2014

Investigating the Biochemical and Catalytic Properties of Nitrile Hydratases

Salette Martinez
Loyola University Chicago, martinez.salette@gmail.com

LOYOLA UNIVERSITY CHICAGO

INVESTIGATING THE BIOCHEMICAL AND CATALYTIC PROPERTIES OF NITRILE HYDRATASES

A DISSERTATION SUBMITTED TO

THE FACULTY OF THE GRADUATE SCHOOL

IN CANDIDACY FOR THE DEGREE OF

DOCTOR OF PHILOSOPHY

PROGRAM IN CHEMISTRY

BY

SALETTE MARTINEZ

CHICAGO, ILLINOIS

AUGUST, 2014

ACKNOWLEDGMENTS

I would like to begin by expressing my sincerest gratitude to Dr. Richard Holz, for introducing me and giving me the opportunity to work in the exciting field of bioinorganic chemistry, for being a great and patient mentor, for his immense support throughout my Ph.D. studies, and for everything that he taught me.

I would also like to thank Dr. Dali Liu for his great support, his advice, mentorship, his collaboration, for being a listener when I had doubts, and for giving me a confidence boost when I seemed to lose it. I would also like to thank Dr. Timothy Elgren from Hamilton College for hosting me at his lab and for his support on one of my projects.

I'm forever grateful to Dr. Misty Kuhn for teaching me valuable skills that have tremendously helped me throughout my research. My fellow graduate students, Natalie Gumataotao and Anna Starus, thanks for being such good friends and labmates. I'm grateful to all the undergraduate students who helped me with my experiments: Karoline Krzywda, Veronika Opalka, and summer intern and High School student, Hei Chan. Also, many thanks, to Rui Wu for her support and her valuable collaboration on many of my projects.

Next, I would like to thank my committee members, Dr. Daniel Becker, Dr. Miguel Ballicora, and Dr. Jacob Ciszek, for their helpful advice; the Chemistry and Biochemistry Department main office staff, Carol Grimm, Stacey Lind, and Denise Hall

for their help with paperwork matters; and Matthew Sara from the Stockroom for his help with laboratory matters. I would also like to thank Mary Dunnwald and Kim Patterson from Marquette University for their help with paperwork matters.

Finally, I would like to thank my parents, Cirilo and Edith, and my siblings for their amazing support and encouragement.

TABLE OF CONTENTS

LIST OF TABLES

LIST OF FIGURES

LIST OF ABBREVIATIONS

NHase	Nitrile Hydratase
Co	Cobalt
Fe	Iron
PtNHase	*Pseudonocardia thermophila* JCM 3095NHase
CtNHase	*Comamonas testosteroni* Ni1 NHase
MbNHase	*Monosiga Brevicollis* NHase
EPR	Electron paramagnetic resonance
DFT	Density functional theory
FT-IR	Fourier transform infrared spectroscopy
ICP-MS	Inductively coupled plasma mass spectrometry
ICP-EAS	Inductively coupled plasma atomic emission spectroscopy
IMAC	Immobilized metal affinity chromatography
BBA	1-Butaneboronic acid
PBA	Phenylboronic acid
WT	Wild-type
HPLC	High performance liquid chromatography
NTCB	2-Nitro-5-thiocyanatobenzoic acid
TMOS	Tetramethyl orhosilicate
Alanine	Ala/A

Arginine	Arg/R
Asparagine	Asn/N
Aspartic Acid	Asp/D
Cysteine	Cys/C
Glutamic Acid	Glu/E
Glutamine	Gln/Q
Glycine	Gly/G
Histidine	His/H
Isoleucine	Ile/I
Leucine	Leu/L
Lysine	Lys/K
Methionine	Met/M
Phenylalanine	Phe/
Proline	Pro/P
Serine	Ser/S
Threonine	Thr/T
Tryptophan	Trp/W
Tyrosine	Tyr/Y
Valine	Val/V
Adenine	A
Cytosine	C
Guanine	G
Thymine	T

ABSTRACT

Chemical and pharmaceutical industries make extensive use of amide compounds for the manufacture of commodity chemicals (e.g., acrylamide) and drug intermediates (e.g., nicotinamide). Production of amide compounds is typically achieved by the hydration of nitrile compounds under acidic or basic conditions, high temperatures, and copper catalysts. However, the use of such chemical methods leads to the generation of unwanted by-products and toxic wastes, in addition to low product yields and high production costs. An alternative route for amide production is the use of a natural catalyst, for example nitrile hydratases (NHase, E.C. 4.2.1.84). NHase is a metalloenzyme that efficiently converts nitriles to amides at neutral pH and ambient temperatures, thus reducing production of unwanted by-products and toxic wastes. NHase contains either a non-heme Fe^{3+} or a non-corrin Co^{3+} metal ion at its active site and consist of two non-homologous subunits, α and β, which form an $(\alpha\beta)_2$ heterotetramer. In order to utilize NHases to their full potential, it is crucial to understand their biochemical and catalytic properties; therefore, the goal of this research project was to gain insight into these fundamental properties. A combination of molecular biology, enzyme kinetics, UV-Visible spectroscopy, X-ray crystallography, and enzyme immobilization were used to accomplish this goal. Three nitrile hydratases were examined; these are the Fe-type NHase from *Comamonas testosteroni* Ni1 and the Co-type NHases from *Pseudonocardia thermophila* JCM 3095 and *Monosiga brevicollis*.

CHAPTER ONE

INTRODUCTION

Nitrile Degrading Pathways

Nitriles are organic compounds that contain an organic moiety and a carbon-nitrogen triple bond (R-C≡N). Nitriles are attractive intermediates for the preparation of amides, carboxylic acids, amines, amidines, esters, aldehydes, ketones, and heterocyclic compounds, etc. (1,2). Besides being utilized as intermediates in organic syntheses, nitriles are also extensively used as feedstocks, solvents, extractants, and pesticides (bromoxynil, dichlorobenil) (2,3). In addition to being synthesized in the laboratory, nitriles are also synthesized by bacteria, plants, and fungi (4,5). In plants, nitrile compounds are produced during the metabolism of cyanogenic glycosides and glucosinolates, which provide a defense mechanism against herbivores and pathogens (4,6). The fungus *Trichoderma harzianum*, for example, synthesizes the nitrile containing antibiotic homothallin II to inhibit competitive organisms such as fungi, Gram-positive, and Gram-negative bacteria (5). Not surprising, due to their extensive use in the chemical, pharmaceutical, and agricultural industries, toxic wastes containing nitriles are often found in industrial discharge and find their way into soils and water streams (1,5).

Bacteria, plants, and fungi are also capable of degrading nitriles to the corresponding carboxylic acid and ammonia. The nitrile degradation pathway begins

after the enzyme aldoxime dehydratase (EC 4.99.1.5) dehydrates an aldoxime to the corresponding nitrile (Figure 1) (7-9). Two biological routes exist for the degradation of the nitrile to carboxylic acid and ammonia: (1) direct hydrolysis by nitrilase (EC 3.5.5.1) or (2) hydration by nitrile hydratase (NHase; 4.2.1.84) to an amide, which is subsequently hydrolyzed to the corresponding acid and ammonia by amidase (EC 3.5.1.4) (Figure 1) (2,10).

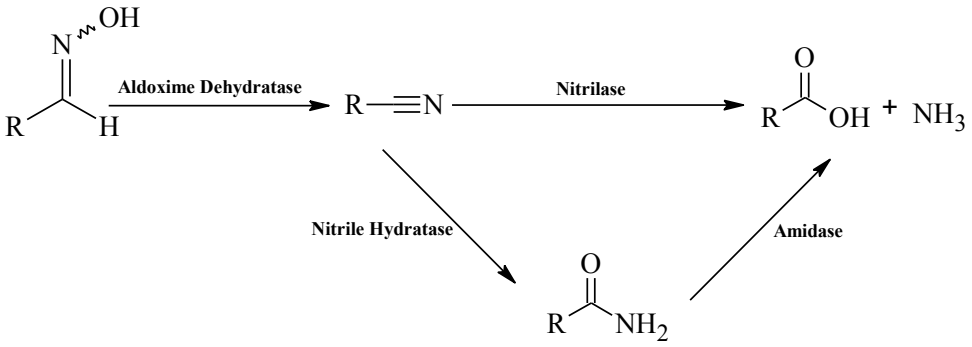

Figure 1. Nitrile degradation pathways.

Bacterial organisms such as *Rhodococcus erythropolis* AJ270 contain gene clusters encoding for aldoxime dehydratase, nitrilase, and nitrile hydratase/amidase systems (11). On the other hand, *Rhodococcus* sp.YH3-3, *Rhodococcus* sp. N-771, *Rhodococcus globerulus* A-4, *Pseudomonas chlororaphis* B23, encode only the genes for aldoxime hydratase and nitrile hydratase/amidase, while *Bacillus* sp. OxB-1encodes the genes for aldoxime dehydratase and nitrilase, respectively (8,12-14). Although the exact biological or physiological function of these nitrile degrading enzymes is unknown, it has been suggested that they are likely involved in nutrient metabolism, providing a carbon and nitrogen source, hormone synthesis (in plants), nitrile detoxification, and nutrient assimilation (4).

In addition to hydrating and/or hydrolyzing their own natural substrates; nitrile degrading enzymes are also able of hydrating and/or hydrolyzing a broad range of synthetic nitrile compounds in a chemo-, regio-, and stereo-selective manner; thus opening an opportunity for their use in organic syntheses, chemical and pharmaceutical industries. In contrast to conventional chemical methods, which require acidic or basic conditions, high temperatures and pressures, and expensive catalysts, reactions utilizing enzymes are done at ambient pressures, temperatures, and physiological pH, thus reducing the generation of unwanted by-products and toxic wastes, normally obtained with conventional chemical methods. Additionally, nitrile degrading enzymes could also be implemented in the bioremediation (biological treatment) of nitrile contaminated soils and water systems.

Biochemical Characteristics and Properties of Nitrile Hydratases

The focus of this introduction will be on the nitrile hydratase enzyme (NHase), which is one of the two enzymes in the pathway (Figure 1) that degrades nitriles to the corresponding amide, which is subsequently converted to carboxylic acid and ammonia. NHases have primarily being isolated from microorganisms such as Proteobacteria, Actinobacteria, Cyanobacteria, and Firmicutes, although, NHase activity has also been reported in some fungi and yeasts (10). Organisms containing NHase have been isolated from different geographical locations including industrial and nitrile contaminated soils, soda lake sediments and soda soils, marine sediments, and deep sea sediments (15-18). Recently, a NHase from the marine sponge *Aplysina cavernicola* was isolated and the presence of putative NHase genes in unicellular eukaryotic organisms has also been reported (19-21). While most isolated NHases are typically mesophilic (stable in

temperatures up to 40º C), there have also been some thermophilic (stable in temperatures from 45-65 ºC) NHases isolated (22).

NHases are metalloenzymes that generally contain cobalt or iron, although the NHase from *Rhodococcus* sp. RHA1 also contains copper, and zinc, respectively (10,23). Based on the metal ion that NHases incorporate into their active site, they are classified as either cobalt-type (Co-NHase) or iron-type (Fe-NHase). Both types of NHases consist of two non-homologous subunits, α and β, which range in size from 20 to 35 kDa (10). Typically, Co-NHases exhibit a higher affinity for aromatic nitrile substrates while Fe-NHase have a higher affinity towards aliphatic nitrile substrates (10).

Several studies have showed that successful expression of soluble and active NHase in *Escherichia Coli* requires the co-expression of open reading frames (ORFs) found downstream of the NHase α and β genes. The products of these ORF's have been termed NHase activators (24-28). In addition, the cobalt containing thiocyanate hydrolase, a homologous enzyme to NHase, which catalyzes the hydration of thiocyanate to carbonyl sulfide and ammonia, also requires an activator protein for functional expression in *E. coli* (29,30). Although, both the Co- and Fe-NHases share high sequence identity, their respective activators or accessory proteins share no homology (31,32). For example, Co-type activators are small proteins (<17 kDa) sharing homology with the β-subunits, while the Fe-activators are larger proteins (> 40kDa) sharing no homology with the α- or β-subunits. Furthermore, a highly conserved cysteine-rich metal binding motif has been identified in the Fe-type activators, while no-metal binding motif has been identified in the Co-activators (33). Based on studies done on the Fe-activator from the *Rhodococcus sp.* N771 NHase and gene products expressed of the ORFs, nhle

and nhhg, located downstream of the β-subunit of the L-NHase and H-NHase from the Co-type *Rhodococcus rhodochrous* J1, it has been proposed that the role of these activator and accessory proteins is to assist with metal insertion and the oxidation of the two equatorial active site Cys residues (32-35).

Characterization by X-ray absorbance spectroscopy, Electron Paramagnetic Resonance (EPR), UV-Visible absorption, Fourier Transform Infrared Spectroscopy (FT-IR), and circular dichroism spectroscopy revealed that the metal ions in NHase exist as low-spin non-corrin Co^{3+} or a low-spin non-heme Fe^{3+} (36-41). Structural analyses by X-ray crystallography showed that the two subunits formed a tight αβ heterodimer and bind one metal atom, the αβ heterodimer loosely interacts with another αβ heterodimer to form an $(\alpha\beta)_2$ heterotetramer (Figure 2) (42-45). Gel-filtration chromatography also supports that the quaternary structure of NHase is a heterotetramer (44).

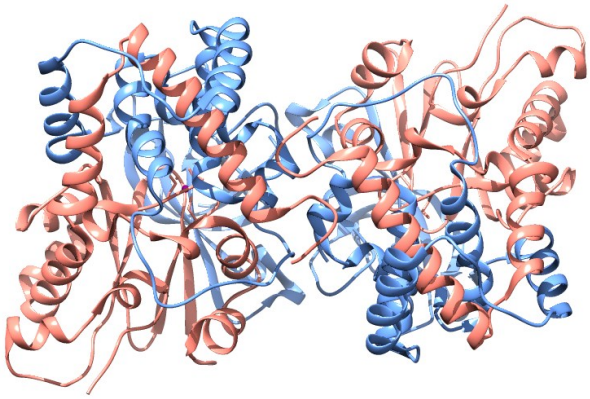

Figure 2. X-ray crystal structure of the Co-NHase $(\alpha\beta)_2$ heterotetramer from *Pseudonocardia thermophila* JCM 3095 (PDB ID: 1IRE). The α subunit is in pink and the β subunit is in blue.

The active site is located at the interface of the α and β subunits, with the highly conserved metal-binding motif (C-T/S-LCSC-Y/T) located in the α subunit, where the

Co-NHase contains Thr and Tyr and the Fe-type contains Ser and Thr (42-45). The active site is composed of four amino acids from the α subunit, three αCys residues, one αSer residue, and two arginine residues from the β subunit (42-45) (Figure 3). The metal ion is bound in an octahedral confirmation and ligated by three cysteine sulfur atoms and two backbone amide nitrogens. The six ligand to the metal ion has been found to be a a water molecule in the Co-NHase from *P. thermophila* JCM 3095and nitric oxide molecule in the Fe-NHase from the *Rhodococcus* sp. N771 while the sixth ligand site is unoccupied in the structures of the Co-NHase from *Bacillus smithii* and the Fe-NHase from *Rhodococcus* sp. R312 (42-45). The two equatorial cysteine ligands are post-translationally modified through oxidation to Cys-sulfenic acid (Cys-SOH) and Cys-sulfinic acid (Cys-SO_2H), respectively (44,46). The backbone amides and the oxidized Cys residues make up a "claw" setting configuration (43). The two conserved Arg residues from the β subunit form hydrogen bonds with the oxygen atoms of the Cys-SOH and Cys-SO_2H and have been proposed to stabilize the claw setting; mutation of βArg56 in the Fe-NHase from the *Rhodococcus* sp. N771 resulted in the complete loss of enzymatic activity (43,44,47).

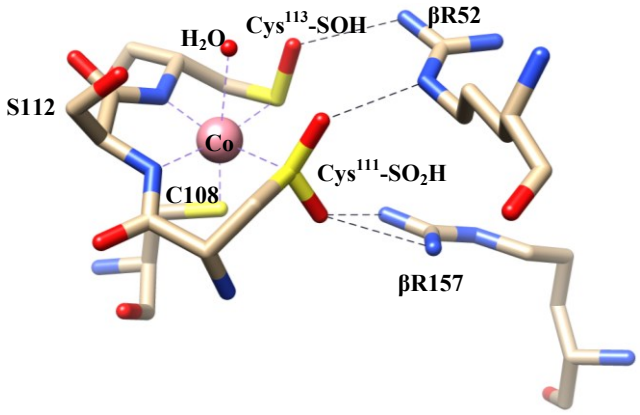

Figure 3. The active site of the Co-NHase from *Pseudonocardia thermophila* JCM 3095 (PDB ID: 1IRE). The metal ion is six-coordinate with one Cys sulfur, one Cys-SOH sulfur, one Cys-SO_2H sulfur, two amide nitrogens, and a water molecule. The oxygens from Cys-SOH and Cys-SO_2H form hydrogen bonds with βArg56 and βArg157

The active site of NHase is unusual among metalloenzymes because of the nature of the ligands and the oxidation state of the metal ion (Figure 3). Usually mononuclear non-heme enzymes exist in the +2 oxidation state and participate in redox reactions; however, in NHases the Fe atom is redox inactive (48,49). On the other hand, NHase is one of the few enzymes that contain cobalt in its active site; the occurrence of cobalt in nature is rare compared to other metals e.g., iron and zinc (50,51). Similar to the Fe-NHase, Co-NHases are also redox inactive. A second unusual feature of NHases is the ligation by the two deprotonated amide nitrogen ligands from the αSer and αCys-SOH peptide backbone (49). This type of ligation has only been observed in the P-cluster of nitrogenase and A cluster of acetyl CoA synthase (48,49). DFT studies have suggested that C-N bonds of the deprotonated amide ligands have significant double bond character; therefore, they are best described as imidates when ligated to the metal ion (52). These imidate ligands can act as strong σ-donors to the metal, thus stabilizing the low-spin state of the metal ion (52). A third unusual characteristic of the NHase active site is the

oxidation of the two equatorial cysteine ligands to Cys-SOH and Cys-SO_2H. Generally, only one type of cysteine oxidation is observed in proteins but not two in the same protein active site as in NHases (49). Usually, ligation of a metal ion by the sulfur atom of Cys residues occurs through π-donation to the metal from the S-atom; however, upon oxygenation of the S-atom, this π- donation is lost and the S-atom becomes a poor π-donor (53,54). To compensate for the loss of π-donation from the Cys-SOH and Cys-SO_2H acid ligands, the non-modified axial Cys residue, which is trans to the water/NO/substrate binding site increases its π-back donation to the metal ion, resulting in a stronger covalent bond between the sulfur and the metal (53). In summary, the properties of the ligands provide a stable environment where the low-spin trivalent metal can exist and participate in catalysis.

Because the iron ion in Fe-NHase is low-spin (d^5, $S = ½$), these NHases can be characterized by various spectroscopic methods including, UV-visible absorption and EPR (49,55). In contrast, the Co-NHases (d^6, $S = 0$) are EPR silent and exhibit a weak absorption band in the visible region between 300 and 400 nm (55). Even though Co-NHases are not useful for spectroscopic studies, these NHases tend to be more stable than the Fe-type. Typically, Fe-NHases tend to quickly lose catalytic activity if isolated and stored in the absence of the weak competitive inhibitor, butyric acid (K_i = 1.3-1.6 mM) which, has been proposed to prevent the oxidation of the active site Cys-SOH to Cys-sSO_2H (56,57). The oxidation of the Cys-SOH to Cys-SO_2H results in inactive NHase (46). Co- NHases are highly stable in the absence of butyric acid, retaining catalytic activity even after 1 year when stored at 4 °C (57). It is this stability that makes Co-NHases attractive as biocatalysts in commercial applications.

Proposed Reaction Mechanisms

In general, the hydration of nitriles is not trivial given that the nitrile carbon is only slightly electrophilic making it relatively unsusceptible to nucleophilic attack by a water/hydroxide molecule (49,58). Therefore, conventional chemistry for the hydration of nitriles requires harsh conditions (e.g., high temperature and copper catalysts) to achieve the hydration reaction, yet NHase is able to easily catalyze the reaction under relatively mild conditions. However, it is not completely understood how NHase is able to achieve the hydration reaction given its unusual electron rich active site. One of the earliest proposed reaction mechanisms (Figure 4) were based on the X-ray crystal structure of an Fe-NHase from *Rhodococcus sp*. R312 complexed with the substrate analogue iodoacetonitrile and previous UV-Visible, EPR and resonance Raman spectroscopy studies done on Fe-NHases (37,42,56,59,60). EPR studies suggested that the substrates propionitrile and isobutyronitrile (37) bound directly to the metal ion, while the competitive inhibitor butyric acid was proposed to hydrogen bond to the metal-bound hydroxide (56). EPR studies also suggested that a water molecule or hydroxide ion is directly coordinated to the active site metal ion occupying the axial site trans to the unmodified Cys ligand (37,59,60). In the NHase X-ray structure complexed with iodoacetonitrile, the nitrile atom from the iodoacetonitrile is coordinated to the iron center (42). Based on these studies, three reaction mechanisms (Figure 4) were proposed with the metal ion acting as a Lewis acid: in mechanism (4A) the substrate binds directly to the metal ion while in mechanisms (4B) and (4C) the metal ion activates a water molecule for nucleophilic attack to the nitrile carbon (42). Further studies are still needed

to differentiate between the three proposed mechanisms and to determine the base and role of the metal ion.

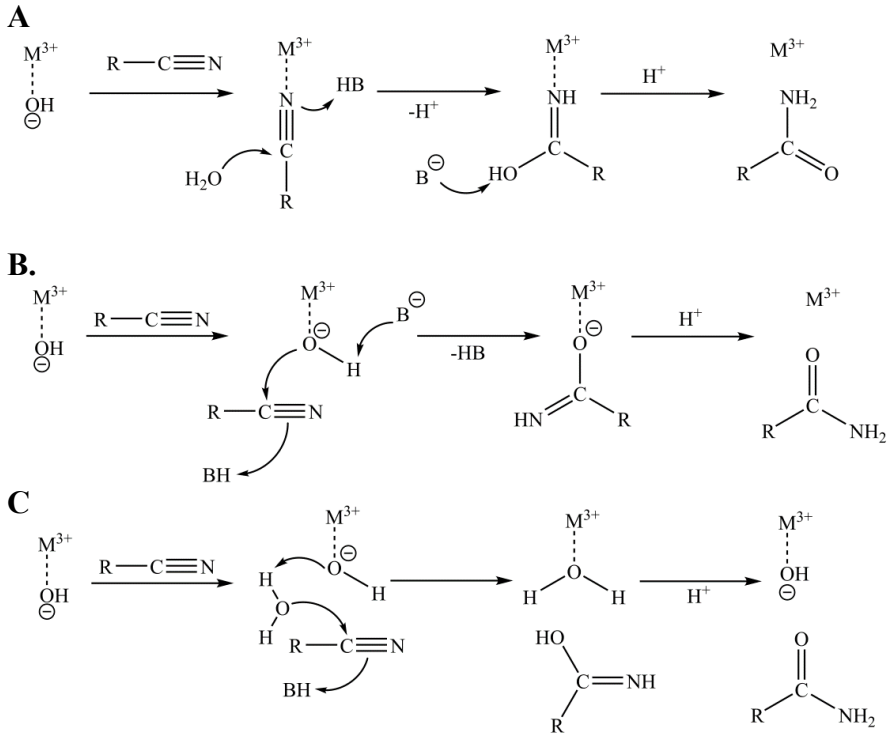

Figure 4. Proposed catalytic mechanisms of NHase based on the X-ray crystal structure of the Fe-NHase from *Rhodococcus* sp. R312. **A)** Direct binding of the nitrile substrate to the metal center and nucleophilic attack by a water molecule, **B)** nucleophilic attack by a metal-bound hydroxide to the nitrile substrate, and **C)** activation of water molecule by a metal-bound hydroxide for nucleophilic attack on the nitrile substrate (42).

Using pH, solvent isotope effects, and temperature dependent kinetic studies on the Co-NHase from *P. thermophila* JCM 3095, Mitra and Holz proposed an alternative reaction mechanism (Figure 5) for NHase. These studies showed, first, that two protons are transferred in the rate-limiting step of the reaction; second, the ionization constants suggest βTyr^{68} and αSer^{112} as potential ionizable groups but that the oxidized Cys ligands αCys^{113} and αCys^{111} were also candidates. Together, these results, along with previous

spectroscopic studies on NHases, and mutation of βTyr^{68} to a phenylalanine on the Co-NHase from *P. thermophila* JCM 3095, allowed a mechanism to be proposed in which (*i*) the substrate binds directly to the metal ion activating it for nucleophilic attack, (*ii*) the nearby deprotonated βTrp^{72} and αSer^{112} act as general bases to activate a water molecule for nucleophilic attack to the nitrile-carbon atom, (*iii*) two protons are then transferred to the nitrile-nitrogen atom, one from the water molecule and the second from the αSer^{112} ligand, and (*iv*) after proton transfer occurs, the resulting imidate tautomerizes to form the amide which is displaced by a water molecule (61). Rao and Holz also proposed a similar mechanism for the Fe-NHase from *Comamonas testosteroni Ni*1, supported by similar solvent pH, temperature dependence, and kinetic isotope effects (62). Together, these studies suggested that nitrile hydration by NHase occurs in a similar fashion in both Fe- and Co-type of NHases. However, this proposed mechanism has come under question from two separate studies. First, optimized density functional theory (DFT) calculations suggested other potential roles for the βTyr^{68} residue; one role is that of a stabilizer by hydrogen bonding to the substrate or another catalytic residue, and the second role is that of a general acid by protonating the metal-bound imidate intermediate (63). The second study focused on the mutation of the βTyr^{72} and αSer^{113} (corresponding to βTyr^{68} and αSer^{112} in the *P. thermophila* JCM 3095 NHase) residues on the Fe-NHase from *Rhodococcus erythropolis* N771 (64). Mutation of αSer^{113} to αAla^{113}, revealed that αSer^{113} is not essential for the catalytic activity of NHase but important for maintaining the electronic state and structure around the active site (64). In contrast, mutation of βTyr^{72} to βPhe^{72}, results in an inactive enzyme and the oxidation of the Cys-SOH ligand to Cys-SO_2H, suggesting that this residue affects the electronic state of the active site

(64). Thus, further clarification is still needed to understand the role of the βTyr in the catalytic mechanism of NHase.

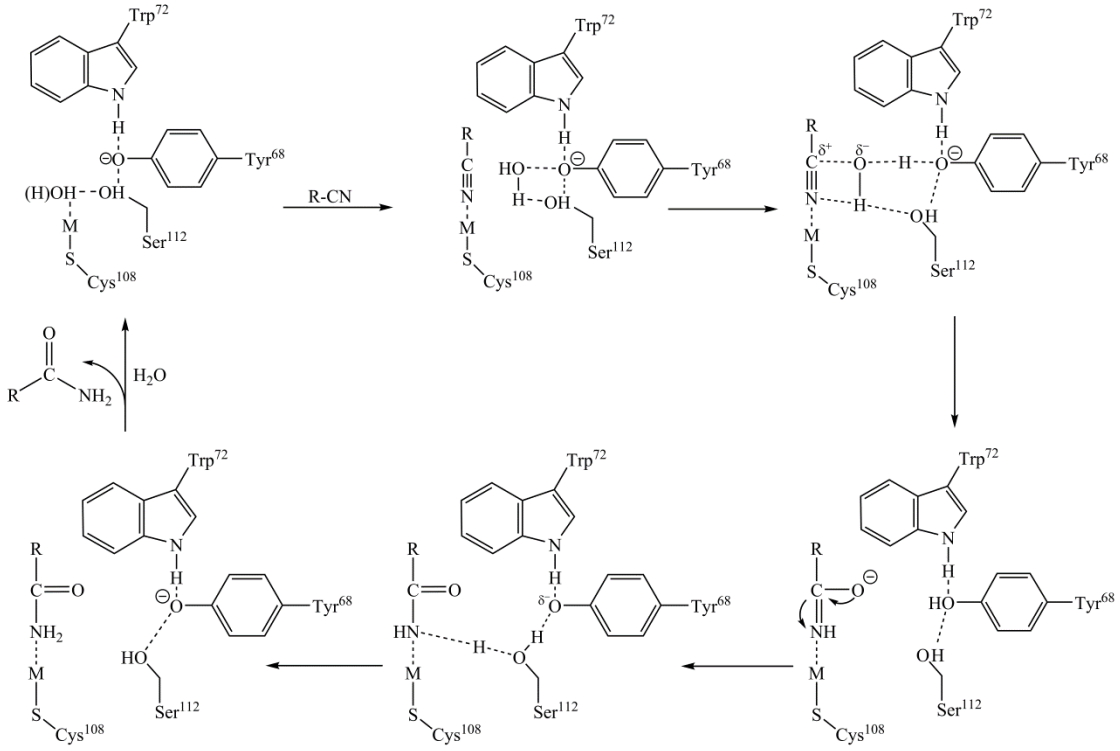

Figure 5. Proposed catalytic mechanism for the Co-NHase from *Pseudonocardia thermophila* JCM 3095 (61).

The reaction mechanism of NHase has also being investigated by DFT using models of the Fe-NHase from *Rhodococcus erythropolis* N-771 (65,66). From these DFT studies, first- and second-shell mechanisms for NHase were proposed (Figure 6 and 7). Calculations for the first-shell model showed that the metal ion is a poor Lewis acid and fails to activate the nitrile substrate for nucleophilic attack by the water molecule (65). Instead, it was proposed that an active-site base could abstract a proton from the water molecule, thus activating it for nucleophilic attack on the nitrile-carbon and lowering the

barrier for nitrile hydration (65). The active-site base in this case was suggested to be the active site Cys-SOH ligand (Figure 6). In the first-shell mechanism (Figure 6), (*i*) the nitrile substrate binds to the metal center, (*ii*), the Cys-SOH ligand deprotonates the water molecule and activates it for nucleophilic attack, (*iii*) the metal-bound imidate abstracts a proton from the Cys-SOH ligand, and (*iv*) tautomerization of the imidate occurs to give the final amide product (65).

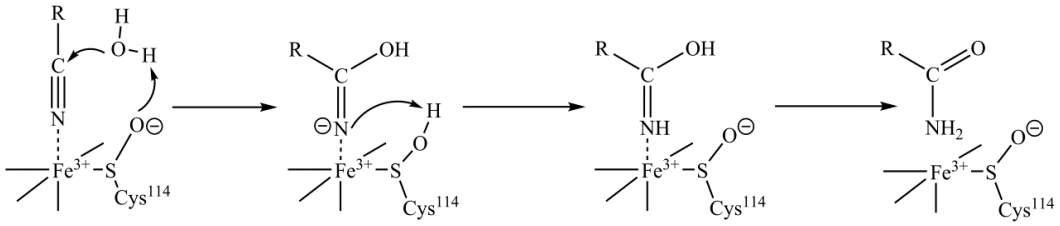

Figure 6. First-shell catalytic mechanism of NHase based on DFT calculations on the *Rhodococcus erythropolis* N-771 NHase (65).

Similar to the first-shell mechanism, the Cys-SOH was proposed to function as a base and an acid, but the nitrile is not directly bound to the metal center. In the first of the two proposed second-shell mechanisms (Figure 7A), (*i*) the Cys-SOH functions as a base, deprotonating the metal-bound water molecule, (*ii*) the resulting metal-bound hydroxide attacks the carbon atom of the nitrile substrate with a concomitant proton transfer from the Cys-SOH to the nitrogen nitrile, and finally (*iii*) the metal-bound imidate tautomerizes and the amide product is released (66). In the other second-shell mechanism (Figure 7B), (*i*) the Cys-SOH functions as the nucleophile and attacks the nitrile carbon with simultaneous proton transfer from the metal-bound water to the nitrile nitrogen, and (*ii*) tautomerization of the metal bound imidate results in the formation of

the amide product (66). While DFT calculations provide possible NHase mechanisms, experimental data with the NHase is still needed to confirm either of the proposed mechanisms. Interestingly, in both first- and second-shell mechanisms, the Cys-SOH is assumed to be in its deprotonated form, in contrast to DFT and XAS studies that have showed that the Cys-SOH in likely found in the protonated form in the resting state at pH 7.5.

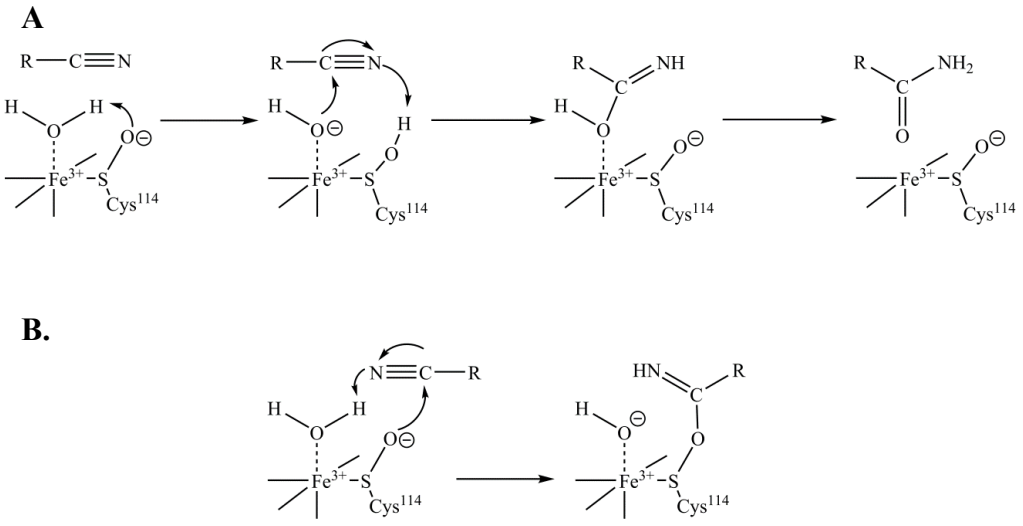

Figure 7. Second-shell catalytic mechanisms of NHase based on DFT calculations on the *Rhodococcus erythropolis* N-771 NHase. **A)** The Cys^{114}-SOH activates a metal-bound water molecule for nucleophilic attack to the substrate and **B)** Cys^{114}-SOH directly attacks the substrate (66).

A similar nucleophilic role for the Cys-SOH was also proposed using an active site cobalt NHase mimetic model, Co^{III}(L-N_2SOSO)(*t*BuNC)$_2$ (Figure 8). In this case, the bis(sulfenato-S)Co^{3+} complex, shows reactivity (40 turnovers) towards acetonitrile under mild acidic conditions, pH 4.8, and 4 °C (67). When the hydration was done in 30% $H_2{}^{18}O$/ $H_2{}^{16}O$ in 1 M HOAc/NaOAc buffer at 4 ºC for 17 h, the complex gave a mixture

of $Co^{III}(LN_2S^{18}OS^{16}O)(t\text{BuNC})_2$ and $Co^{III}(LN_2S^{18}OS^{18}O)(t\text{BuNC})_2$, indicating that an exchange of the oxygen atom occurred at the coordinated sulfenate during the hydration of acetonitrile. On the other hand, when the reaction was done under the same conditions but in the absence of the substrate, acetonitrile, no incorporation of ^{18}O was observed. These results led the authors to proposed a mechanism (Figure 8) in which (*i*) the sulfenic acid acts as the nucleophile attacking the nitrile carbon with a proton transfer from the general acid (HOAc/NaOAc buffer) to the nitrile nitrogen, (*ii*) a water molecule subsequently attacks the sulfenic sulfur, (*iii*) a proton transfer to the imidate intermediate results in tautomerization of the imidate and product release, allowing (*iv*) the sulfenic acid to be regenerated to complete the catalytic cycle (67). Although, a possible mechanism for NHase, this mimetic model has no open coordination site like in NHase and again the sulfenic acid is assumed to be in the deprotonated form.

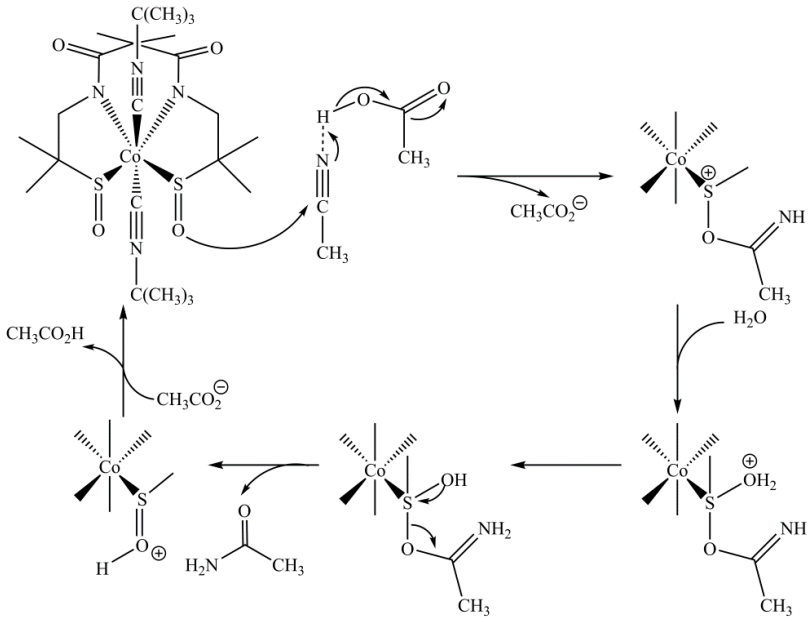

Figure 8. Proposed catalytic mechanism of NHase based on the Co-NHase bis(sulfenato-S)Co^{3+} mimetic complex (67).

The most recently proposed reaction mechanism (Figure 9) is supported by time-resolved X-ray crystallography using the slow substrate *tert*-butylisonitrile. The Fe-NHase from *Rhodococcus erythropolis* N771 catalyzes the hydration of *tert*-butylisonitrile to *tert*-butylamine and carbon monoxide very slowly (k_{cat} = 0.018 s^{-1}) (68,69). This X-ray structural study revealed several potential reaction intermediates including: (*i*) substrate binding to the metal center, (*ii*) a water molecule residing near the isonitrile carbon and the Cys-SOH ligand, and (*iii*) the *tert*-butylamine product above the active site and a water molecule near the Cys-SOH ligand (69). Based on these characterized potential reaction intermediates a mechanism (Figure 9) was proposed where (*i*) the nitrile substrate displaces the metal-bound water molecule binding directly to the metal ion activating the nitrile carbon for nucleophilic attack, (*ii*) subsequently, the Cys-SOH acts as a catalytic base and deprotonates a nearby water molecule, (*iii*) proton transfer to the metal-bound imidate occurs, and (*iv*) the metal-bound imidate tautomerizes and the amide product is liberated (69). This mechanism is similar to the first-shell mechanism (Figure 6) proposed by DFT calculations except for the change in oxidation state of the iron from 3+ to 2+.

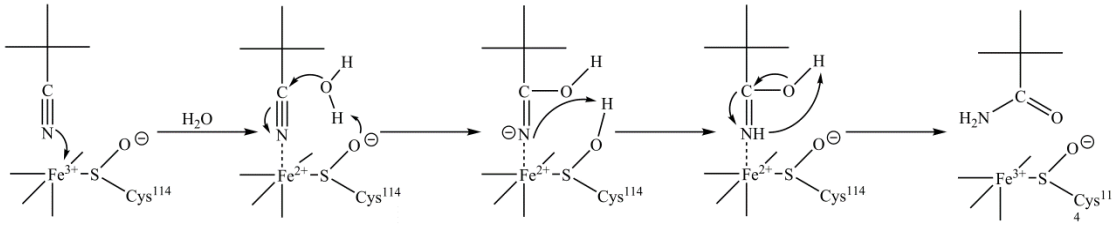

Figure 9. Proposed catalytic mechanism of NHase based on time-resolved X-ray crystallographic studies on the *Rhodococcus erythropolis* N771 using *tert*-butylisonitrile (69).

In summary, aspects of the proposed mechanisms mentioned above could potentially be correct, but there are still several details about the mechanism that need to be clarified. These include: (*i*) the role of the metal, does it bind the substrate or a water/hydroxide molecule?; (*ii*) identities of the catalytic base, nucleophile, general acid or base; (*iii*) protonation states of the post-translationally oxidized equatorial cysteine ligands. In addition, besides the described potential NHase reaction intermediates characterized by time-resolved X-ray crystallography, there are no other reported NHase reaction intermediates. Such data could be extremely useful in determining the correct mechanism by which NHase hydrates the nitrile to the amide.

Application and Immobilization of Nitrile Hydratases

NHases are attractive catalysts because they are able to hydrate a wide array of nitrile compounds (e.g., acrylonitrile, benzonitrile, isobutyronitrile, methacrylonitrile, valeronitrile, adiponitrile, propionitrile, 3-oxonitriles, 3- and 4-hydroxy-2-methylenenitriles, 3-hydroxynitriles, ibuprofen nitrile, 2,6-difluorobenzonitrile, 2-(4-chlorophenyl)-3-methylbutyronitrile, 2-thiophenacetonitrile, thiacloprid, aeroplysinin-1, etc.) to their corresponding amides in a chemo-, regio-, and stereo-selective manner at ambient pressures, temperatures, and physiological pH (70-72). Currently NHase is used for the commercial production of acrylamide from acrylonitrile (>30,000 tons/year, Mitsubishi-Rayon) and nicotinamide from 3-cyanopyridine (>3,500 tons/y, Lonza) (73,74). These transformations are examples of "green chemistry" because by using NHase as the catalyst the conversion of the nitrile proceeds to ~100% of the amide product, thus eliminating generation of unwanted side reactions, toxic wastes, and the use of expensive and toxic catalysts. However, there are several hurdles that must be

overcome for successful implementation, namely, the instability of the enzyme under the operational conditions (e.g., industrial reactors, high concentrations of substrate and product, organic solvents, and high temperatures), separation from the reaction mixture, and reusability (75-77). Such limitations are often overcome by immobilizing the enzyme (75-78).

Enzyme immobilization is typically achieved by one or more traditional methods; attachment to a carrier, cross-linking, and encapsulation (78-80). Attachment to a carrier or support binding is achieved through covalent, ionic, adsorption, metal, or bio-affinity binding. Examples of carriers for attachment include synthetic organic polymers, biopolymers, hydrogels, inorganic polymers, and smart polymers (78). Entrapment of an enzyme in an organic polymer (e.g., alginates and polysaccharides), or a silica sol-gel, occurs when the synthesis of a polymeric network is performed in the presence of the enzyme, in other words, a cage is built around the enzyme (78,80,81). Immobilization by cross-linked of enzyme aggregates (CLEAs) and cross-linked of enzyme crystals (CLECs) is accomplished by using a chemical cross-linker such as the bifunctional glutaraldehyde, which reacts with the protein amine groups (78,81). All the described immobilization methods have advantages and disadvantages, but depending on the intended application one or a combination of any of the methods can be used to create a suitable immobilized NHase.

For acrylamide production Mitsubishi-Rayon uses *Rhodococcus rhodochrous* J1 whole cells containing Co-NHase. The *R. rhodochrous* J1 whole cells are immobilized by encapsulation in a polyacrylamide matrix (82,83). The acrylamide is produced by continuously passing acrylonitrile through a series of fixed-bed reactors containing the

polyacrylamide-immobilized NHase in aqueous conditions of pH 7.5-8.5 at a temperature of 0-5 ° C, affording ~99.9% conversion and selectivity (82,84). Similarly, Lonza uses the same polyacrylamide-immobilized *R. rhodochrous* J1 whole cells containing the Co-NHase for the conversion of 3-cyanopyridine to nicotinamide (>99% selectivity and conversion) under mild aqueous conditions (74). The immobilization of the whole-cells enables an easy separation of the catalyst from the reaction mixture and subsequent reusability.

To generate the starting reagent 5-cyanovaleramide used in the synthesis of the herbicide azafenidin (Milestone), DuPont immobilized *Pseudomonas chlororaphis* B23 whole cells containing an Fe-NHase by encapsulation in calcium-alginate beads (85). Using the calcium-alginate immobilized cells containing NHase, adiponitrile is hydrated to 5-cyanovaleramide in 23 mM sodium butyrate and 5 mM calcium chloride buffer, pH 7, at 5 ° C with high regioselectivity and a 97% overall conversion (85). Additionally, up to 58 consecutive batch reactions were run with the recycled immobilized cells (85). DuPont also immobilized *E. coli* SW132 cells containing the Co-NHase from *Comamonas testosteroni* 5-MGAM-4D by encapsulation in alginate beads to hydrate acrylonitrile to acrylamide (86). A total of 206 consecutive batch reactions using recycled catalyst were run at 5 °C in aqueous conditions, pH 7.0, to produce 1035 g of acrylamide/g dry cell weight and 95 g/ acrylamide/L (86).

The cell-free NHase from haloalkaliphilic actinobacterium strain ANL-iso2 was immobilized by cross-liked enzyme aggregates (CLEAS). The cell-free extract was immobilized using ammonium sulfate as the aggregation agent and cross-linking with glutaraldehyde (87). Although the relative activity of the immobilized NHase was low,

21%, the immobilized NHase had longer storage stability (the activity remained unchanged after 4 months), greater tolerance for high concentrations of the substrate, acrylonitrile, and the product, acrylamide, compared to the soluble NHase (87). Moreover, the CLEA immobilized NHase was successfully recycled and reused for a total of 35 consecutive acrylonitrile hydration reactions in 10 mM Tris-HCl buffer, pH 8.0, at 21 °C (87). Table 1 presents examples of successful immobilization of NHase published in the last four years by one or a combination of the traditional immobilization methods.

In summary, NHase has been immobilized by various methods but there are still some limitations to overcome. For example, some of the conversions had to be done at low temperature to prevent the rapid decrease in activity of the immobilized NHase at higher temperatures; lower reaction temperatures led to a decrease in the reaction rate. In some cases, low concentrations of substrate were used during the conversions because similar to the unimmobilized NHase, the immobilized enzyme could not tolerate high substrate or product concentrations. Because the hydrations were done in aqueous conditions, a two-phase mixture of substrate and product was observed. In this case, it will be advantageous to perform the hydration in organic solvents to overcome solubility issues observed with hydrophobic nitriles. Lastly, leaching of the immobilized NHase from the support or matrix has also been observed leading to a loss in activity.

Table 1. Summary of Immobilized Nitrile Hydratases.

Organism	Immobilization Method/Support	Substrate/Product	Reference
Rhodococcus rhodochrous ATCC BAA-870	Entrapment/ Poly(vinylalcohol)-Chitosan Cross-linking/ Chitosan-glutaraldehyde Cross-linking and entrapment/ Chitosan-glutaraldehyde-Poly(vinylalcohol)	3-Cyanopyridine/ Nicotinamide	(88)
Rhodococcus erythropolis MTCC 1526	Entrapment/Alginate	3-cyanopyridine/nicotinamide, 4-cyanopyridine/ isonicotinamide, benzonitrile/benzamide, pyrazinonitrile/pyrazinecarboxamide, isobutyronitrile/isobutyramide	(89)
Rhodococcus ruber gt1	Absorption/ Raw coal	2-cyanopyridine/Picolinamide, 4-cyanopyridine/Isonicotinamide	(90)
Rhodococcus ruber gt1	Cross-linking/ Activated Chitosan	Acrylonitrile/Acrylamide	(91)
Rhodococcus ruber strain gt1	Absorption/ aluminum oxides Absorption/carbon support	Acrylonitrile/acrylamide	(92)
Geobacillus pallidus RAPc8	Cross-linking/ Eupergit®C-EDAC	3-Cyanopyridine/Nicotinamide	(93)

Proposed Research Aims

NHase is an attractive enzyme for the production of amides; however, much work remains to be done to completely understand the function of this enzyme. Even though NHase has been successfully immobilized in various supports or carriers, there is still room to explore other immobilization supports to improve some of the limits encountered with the current immobilized NHases. In this thesis we present studies that address

unknown aspects of the catalytic mechanism of NHase using kinetic, substrate-analog inhibitors, and structural analyses of the Co-NHase from *Pseudonocardia thermophila* JCM 3095. The functionality of the Fe-NHase from *Comamonas testosteroni Ni*1 was characterized by kinetic and structural analyses. In addition, the role of nearby active site residues in the mechanism of NHase was investigated by site-directed mutagenesis studies, kinetic, UV-Visible spectroscopy, and structural studies on the Fe-NHase *Comamonas testosteroni Ni*1. In regard to NHase functionality, a novel eukaryotic NHase from *Monosiga brevicollis* was discovered and characterized by kinetic analysis, UV-Visible spectroscopy, and inductively coupled plasma mass spectrometry. Lastly, in search of a different support for NHase immobilization, the Co-NHase from *Pseudonocardia thermophila JCM* 3095 was encapsulated in tetramethyl orhosilicate matrices sol-gel matrices and characterize by kinetic analysis.

CHAPTER TWO

THE ACTIVE SITE SULFENIC ACID LIGAND IN NITRILE HYDRATASES CAN FUNCTION AS A NUCLEOPHILE

Research Aim

As described in the introduction section, several reaction mechanisms have been proposed for NHase enzymes; however, questions regarding the role of metal ion, the identities of the general acid/base, and/or nucleophile, remain unclear. Boronic acid compounds have been shown to be potent inhibitors of numerous hydrolytic enzymes including serine, aspartic and cysteine proteases as well as metalloproteases due to the open shell of boron, which allows it to expand from a trigonal planar (sp^2) form to a tetrahedral form (sp^3) (94,95). Such properties make boronic acids useful in mechanistic studies because it allows them to mimic the transition state or reaction intermediates of a hydrolytic enzyme-catalyzed reaction. Therefore, we examined the inhibition of the Co-NHase from *Pseudonocardia thermophila* JCM 3095 (*Pt*NHase) by 1-butaneboronic and phenylboronic acids via kinetics and X-ray crystallography.

Boronic Acids are Potent Inhibitors of Nitrile Hydratase

The ability of both 1-butaneboronic acid (BuBA) and phenylboronic acid (PBA) to inhibit *Pt*NHase was examined by monitoring the hydration of acrylonitrile to acrylamide spectrophotometrically at 225 nm ($\varepsilon = 2.9\ mM^{-1}\ cm^{-1}$). In the absence of

inhibitors, *Pt*NHase catalyzed the hydration of acrylonitrile at pH 7.5 and 25 °C with a k_{cat} value of 1,310 ± 110 s^{-1} and a K_m value of 0.8 ± 0.1 mM. Inspection of the reaction time course for the hydration of acrylonitrile at pH 7.5 and 25 °C by *Pt*NHase in the presence of BuBA or PBA, indicate that both boronic acids function as potent competitive inhibitors of *Pt*NHase. For BuBA, linear reaction progress curves were observed providing an inhibition constant (K_i) of 0.5 ± 0.1 μM. On the other hand, PBA displayed biphasic progress curves, which is characteristic of slow-binding inhibition. The slow-binding inhibition properties of PBA were analyzed based on the equilibrium shown in Figure 10, where K_i ($K_i = k_1/k_2$) is the equilibrium inhibition constant for the formation of the initial complex, EI, k_3 and k_4 are the forward and reverse rate constants for the equilibrium between the EI and the EI* complex (96). By measuring the reaction time course at different concentrations of PBA and substrate, the initial K_i was found to be 5.0 ± 0.9 μM. The overall K_i^* of 0.04 ± 0.01 nM, where $K_i^* = K_i k_4/k_3 + k_4$, was determined by preincubating *Pt*NHase with PBA for 1 h at pH 7.5 and 25 °C followed by reaction with various concentrations of acrylonitrile.

$$E + I \underset{k_2}{\overset{k_1}{\rightleftharpoons}} EI \underset{k_4}{\overset{k_3}{\rightleftharpoons}} EI^*$$

Figure 10. Equilibrium scheme for the slow-binding inhibition of enzyme-catalyzed reactions.

Since both BuBA and PBA function as competitive inhibitors of *Pt*NHase, they must bind to the enzyme active site. In solution, BuBA was reported to be >99% in the

boronic acid form (sp^2 hybridized) at pH 8.0, with a reported pK_a of 10.6 (97). Similarly, the pK_a of PBA is 8.9 (98), so it too will be in the boronic acid form at pH 7.5. Therefore, both BuBA and PBA likely bind to *Pt*NHase in their sp^2 hybridized forms resulting in the displacement of the axial water molecule. This initial Co(III) binding-step was hypothesized to be followed by attack of an active site nucleophile, such as the sulfenic acid ligand, on the electron deficient p_z orbital of the boron atom, since it was recently suggested that boronic acids might inhibit NHases by interacting with the sulfenic acid ligand (99). Nucleophilic attack of the electron deficient p_z orbital of the boron atom is also consistent with previous studies of boronic acid inhibitors bound to hydrolytic enzymes, as hydrolytic reactions typically proceed through a transition-state resulting from nucleophilic attack of the substrate (100,101).

Nitrile Hydratase Complexed with 1-Butaneboronic Acid

To confirm that BuBA binds directly to the low-spin Co(III) ion in the active site of *Pt*NHase and to determine if BuBA has undergone nucleophilic attack, X-ray crystal structures of wild-type (WT) *Pt*NHase and two *Pt*NHase-BuBA complexes formed by either soaking or co-crystallization were solved and refined to 1.9, 1.5 and 1.6 Å resolution, respectively. The overall structure of WT *Pt*NHase is identical to the previously reported structure (PDB ID: 1IRE) (44,57). The active site is the typical "claw setting" observed in all nitrile hydratases with an axial water molecule directly coordinated to the Co(III) ion and forming hydrogen bonds with αSer^{112}, the sulfinic acid ligand (αCys^{111}-O_2H) and the sulfenic acid ligand (αCys^{113}-OH). The protonation states of the sulfenic and sulfinic acid ligands have previously been assigned based on sulfur K-edge XAS data, which indicated the presence of three types of Cys ligands in a WT Fe-

NHase *Rhodococcus erythropolis* N771 (54). These XAS data combined with geometry-optimized DFT calculations suggested the presence of $CysS^-$, CysSOH and $CysSO_2^-$ at pH 7.5.

Upon soaking a crystal of WT *Pt*NHase in cryo-protectant containing 10 mM BuBA for 20 s followed by flash freezing in liquid nitrogen, electron density corresponding to the BuBA inhibitor was present at the active site replacing the axial water molecule (Figure 11). This observation is consistent with the fact that BuBA is a competitive inhibitor of *Pt*NHase. In the WT structure (not shown) the Co(III)-O water bond distance is 2.3 Å compared to a Co(III)–O boronic acid oxygen bond distance of 2.2 Å. Interestingly, the oxygen atom of the αCys^{113}-OH is covalently bound to the boron atom of BuBA (1.5 Å) (Figure 11). This covalent bond, which has not been observed previously, is the result of nucleophilic attack of the sulfenic acid oxygen atom on the empty p_z orbital of the boron atom and the subsequent loss of a boronic acid oxygen atom. Even though the oxygen atom of αCys^{113}-OH is covalently bound to boron, αCys^{113} remains ligated to the low-spin Co(III) ion with a bond distance of 2.2 Å identical to that observed in the WT enzyme. The resulting boron atom is essentially trigonal planar (sp^2) with a dihedral angle of ~170º.

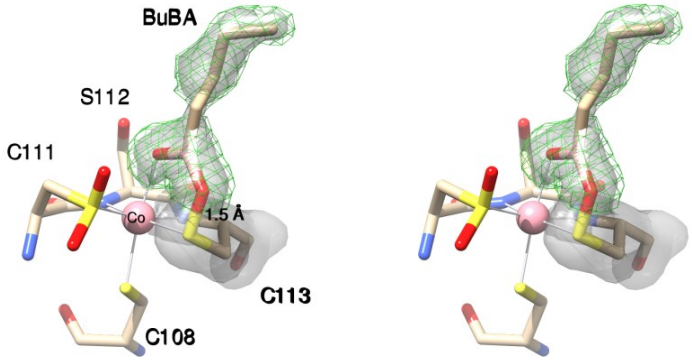

Figure 11. Stereo view of *Pt*NHase bound by BuBA obtained via soaking WT *Pt*NHase in BuBA (PDB ID: 4OB2). A crystal of WT *Pt*NHase was soaked in cryo-protectant containing 10 mM BuBA for 20 s followed by flash freezing in liquid nitrogen. The $2f_o$-f_c map is shown as a transparent grey surface at the 1.1 σ level around BuBA and αCys^{113}. The simulated-annealing omit map (f_o-f_c) is shown around BuBA as a green mesh at 2.7 σ.

On the other hand, the *Pt*NHase-BuBA structure obtained via co-crystallization of WT *Pt*NHase and 10 mM BuBA, reveals that the S-O boronic acid oxygen interaction is significantly diminished (Figure 12). BuBA binding displaces the axial water molecule resulting in a Co(III)-O bond distance of 2.2 Å; however, the second oxygen atom of BuBA is 2.9 Å away from the sulfur atom of Cys^{113}. While this distance is still within the van der Waals radii of sulfur and oxygen, which is ~3.3 Å, it is clear that the αCys^{113}-OH interaction is considerably weakened compared to that observed in the *Pt*NHase-BuBA structure obtained via soaking. This weak S-O interaction is likely due to the initial dissociation of boronic acid from the active site and not the initial binding step. If it were the initial binding step of a boronic acid, αCys^{113} would need to be in its fully reduced form which is not the case as αCys^{113} is clearly oxidized to its sulfenic acid form in the WT *Pt*NHase structure. Therefore, the observed S-O elongation is assigned to boronic acid dissociation. The αCys^{113}-S remains bound to the Co(III) ion with a bond

length of 2.3 Å. The boron atom of BuBA also remains nearly trigonal planner (sp^2) with a dihedral angle of ~160°.

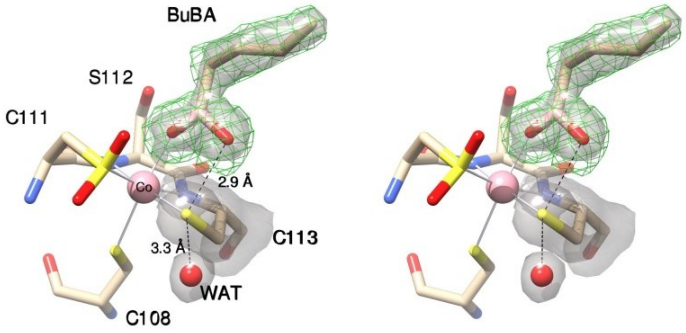

Figure 12. Stereo view of *Pt*NHase bound by BuBA obtained via co-crystallization of WT *Pt*NHase and 10 mM BuBA (PDB ID: 4OB1). The $2f_o$-f_c map is shown as a transparent grey surface at the 1.1 σ level around BuBA and αCys^{113}. The simulated-annealing omit map (f_o-f_c) is shown around BuBA as a green mesh at 2.8 σ.

These two structures represent a "snapshot" of two potential intermediate-states in nitrile hydration by depicting nucleophilic attack by the sulfenic acid ligand and the initial stage of the product-release step. Product loss may occur as the result of a concomitant nucleophilic attack on the αCys^{113} ligand by a water molecule. This is consistent with the observation that a water molecule that is hydrogen bound (2.9 Å) to the NH_2 group of βArg^{157}, is only 3.3 Å from the αCys^{113} ligand. This water molecule may represent the incoming oxygen atom required to reestablish the αCys^{113}-OH ligand. Interestingly, no water molecule is observed within 4 Å of the boron atom in either BuBA structure (Figure 11 and 12), suggesting that a water molecule is not poised for nucleophilic attack on the boron atom facilitating boronic acid formation and product release.

Nitrile Hydratase Complexed with Phenylboronic Acid

Since *Pt*NHase can hydrate both alkyl and aromatic nitriles (57), the X-ray crystal structure of the *Pt*NHase-PBA complex also was obtained via co-crystallization of WT *Pt*NHase and 10 mM PBA and refined to 1.2 Å resolution (Figure 13 and 14). Interestingly, electron density corresponding to the active site cobalt ion and the PBA suggests ~80% occupancy. These data are consistent with inductively coupled atomic emission spectroscopy (ICP-AES), which typically indicates that only 0.8 to 0.9 cobalt ions are present per αβ dimer. Similar to the *Pt*NHase-BuBA structure obtained via soaking, the structural model representing 80% occupancy contains a boronic acid oxygen atom that displaces the axial water molecule and binds directly to the active site Co(III) ion with a bond distance of 2.2 Å (Figure 13 and 14). Similar to the *Pt*NHase-BuBA structure (Figure 13), the boron atom of PBA has undergone nucleophilic attack by the αCys^{113}-OH oxygen atom forming a covalent bond with a B-O distance of 1.5 Å and an S-O bond distance of 1.8 Å. The S-atom of αCys^{113}-OH remains a Co(III) ligand with a bond distance of 2.2 Å. The resulting boron atom is nearly trigonal planar with a dihedral angle of ~160^{o} and the unbound oxygen atom of the original boronic acid moiety is lost. The structural model representing the remaining ~20% of the observed density is similar to the previously reported apo-*Pt*NHase (Figure 14) (57). These data indicate that the *Pt*NHase-PBA complex represents a covalently bound intermediate-state for nitrile hydration, similar to the *Pt*NHase-BuBA complexes, where the αCys^{113}-OH ligand functions as the nucleophile.

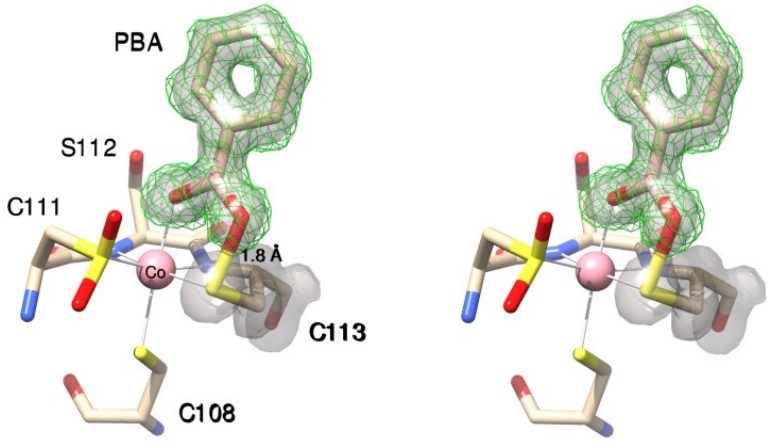

Figure 13. Stereo view of *Pt*NHase bound by PBA at 1.2 Å resolution obtained via co-crystallization of WT *Pt*NHase and 10 mM PBA (PDB ID 4OB0). The $2f_o$-f_c map of the structural model representing 80% occupancy is shown as a transparent grey surface at the 1.4 σ level around PBA and αCys^{113}. The simulated-annealing omit map (f_o-f_c) is shown around PBA as a green mesh at 2.8 σ.

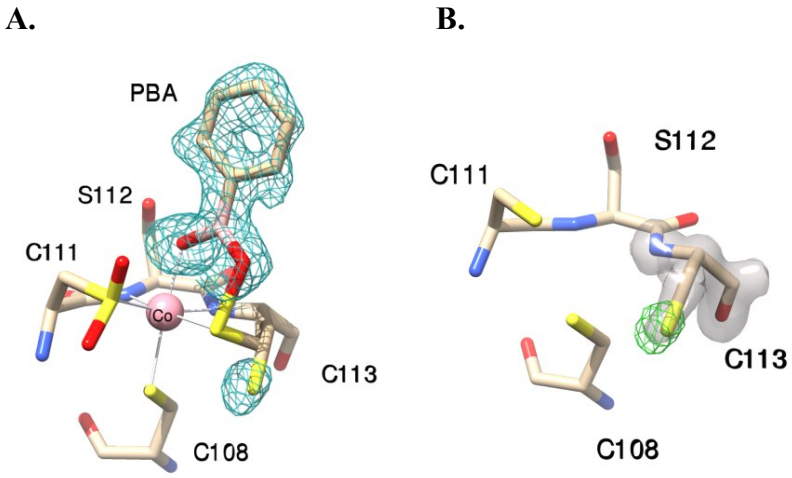

Figure 14. *Pt*NHase complexed with PBA at 1.2 Å resolution obtained via co-crystallization of WT *Pt*NHase and 10 mM PBA (PDB ID: 4OB0). **A)** The experimental difference (f_o-f_c) map is shown around the major alternate conformation (~80%) around later built PBA and the minor apo-structure (~20%) as a cyan mesh at 2.6 σ level. **B)** The $2f_o$-f_c map around the minor alternate conformation of αCys^{113} is shown in transparent grey surface at 1.4 σ level, the simulated-annealing omit (f_o-f_c) map for the minor conformation of αCys^{113} is shown in green mesh at 2.8 σ level.

Proposed Nitrile Hydratase Mechanism

Based on the obtained three structures, parallels can be drawn between boronic acid binding to *Pt*NHase and a nitrile substrate that are consistent with the sulfenic acid ligand functioning as a nucleophile. Kinetic and X-ray crystallographic data indicate that proper oxidation of the αCys^{113} ligand to a cysteine-sulfenic acid is essential for NHase enzymes to be active catalysts suggesting that the S-OH bond is polarized and poised for nucleophilic attack (46,102,103). The catalytic function of the αCys^{113}-OH is also consistent with the rate constants provided by single-turnover stopped-flow studies that indicate a fast pseudo-first order step that involves substrate binding to the trivalent metal ion in the enzyme active site, while product release is the rate-limiting step consistent with a sulfenic acid covalent intermediate complex (104). Additional evidence for metal-ligated sulfenic acids that can function as nucleophiles can be gleaned from NHase model complex studies (67,105). A coordinatively saturated bis(sulfenato-S)Co(III) complex was shown to slowly hydrate acetonitrile to acetamide under acidic conditions while the bis(sulfinato)Co(III) complex was unable to hydrate nitriles (Figure 8) (67). As neither of these compounds have an open coordination site to allow nitrile or water binding, these data implicated the Co(III) sulfenic acid ligand as the nucleophile.

It has long been assumed that a water molecule or a hydroxide ion in the NHase active site functions in the initial nucleophilic attack on an activated nitrile carbon atom. However, our studies provide evidence that the αCys^{113}-OH ligand can function as a nucleophile. The combination of these data with previously reported stopped-flow, kinetic, and X-ray crystallographic data allows a novel catalytic mechanism to be proposed for NHase enzymes with a heretofore unknown role for the αCys^{113}-OH

sulfenic acid ligand (Figure 15). Stopped-flow data indicate that the first step in catalysis involves the direct ligation of the nitrile to the active site low-spin, trivalent metal ion (104). Displacement of the metal-bound water molecule by a nitrile and coordination to the active site metal center activates the CN bond towards nucleophilic attack by the αCys^{113} -OH sulfenic acid ligand. Once nucleophilic attack of the nitrile carbon occurs, two protons are transferred in the rate-limiting step for both Fe- and Co-NHase enzymes (61,62). We propose that one proton transfer occurs between the αCys^{113}-OH ligand and the nitrile N-atom, while the second transfer occurs between the water molecule that reforms αCys^{113}-OH and the newly forming imidate N-atom, consistent with the observed normal isotope effect (61,62). That the αCys-OH ligand is protonated, was suggested by S K-edge XAS and DFT studies (54). Once proton transfer occurs, the resulting covalently bound imidate can tautomerize to form an amide upon nucleophilic attack by a water molecule on αCys^{113} (pathway **A**). Alternatively, nucleophilic attack by water at the C-atom of the imidate intermediate could occur (pathway **B**), such that the oxygen atom of the amide product would be derived from H_2O, not the sulfenic group. In this alternative, the Co(III) ion and sulfenic acid group work together to form and stabilize the imidate intermediate, which can then be hydrated with sulfenic acid functioning as the leaving group. Finally, the amide product can be displaced by a water molecule and thus provide the regenerated catalyst.

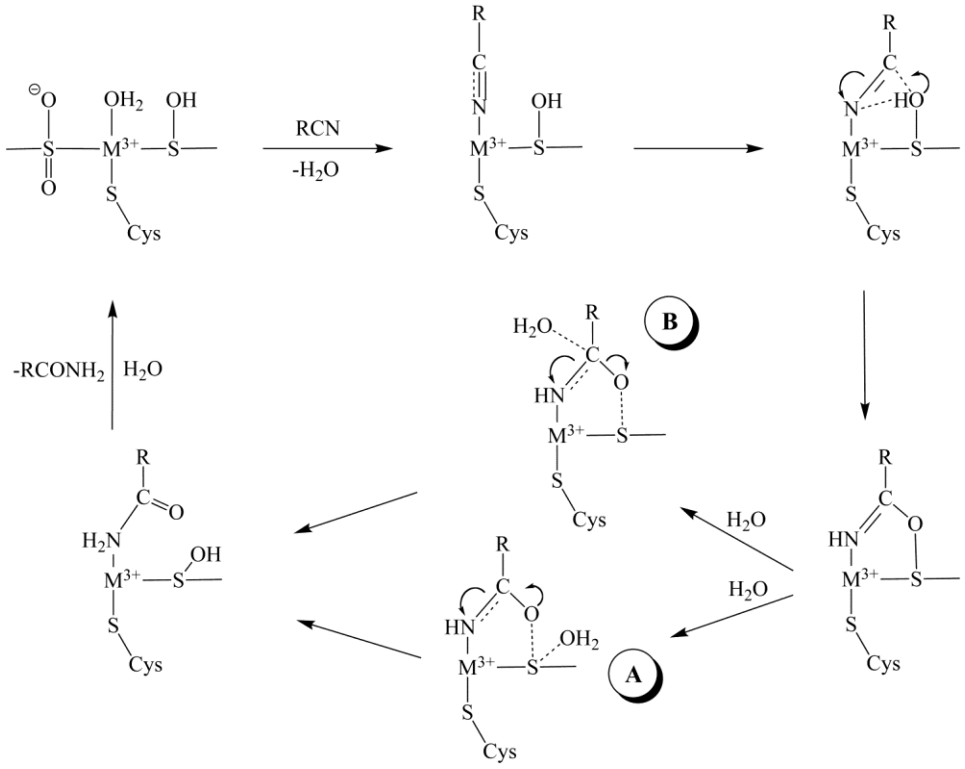

Figure 15. Proposed catalytic mechanism for NHase where the Cys-SOH acid is the nucleophile.

Summary

The work from this study shows that the post-translationally oxidized active site Cys-SOH in nitrile hydratases can function as the nucleophile in the hydration of the nitrile substrate to the corresponding amide. Based on the NHase-boronic acid complexes, which represent potential intermediates in the NHase catalytic cycle, we have proposed a new reaction mechanism for NHase. This work has been published in the Journal of the American Chemical Society: Salette Martinez, Rui Wu, Ruslan Sanishvili, Dali Liu, and Richard Holz, *Journal of the American Chemical Society*, **2014**, *136*, 1186–1189.

Experimental Procedures

Materials. Acrylonitrile, 1-butaneboronic acid, phenylboronic acid, sodium citrate tribasic dehydrate, and 4-(2-hydroxyethyl)piperazine-1-ethanesulfonic acid (HEPES) were purchased from Sigma-Aldrich. All reagents were of the highest purity available and used as received without further purification.

Plasmid construction. A pUC18-NHase plasmid encoding the α-subunit and β-subunit genes of *Pt*NHase (44,61), was used as a template for the polymerase chain reaction (PCR). A polyhistidine (His_6) affinity tag was engineered onto the C-terminus of the α-subunit gene using Phusion DNA polymerase (New England Biolabs). The following primers were used for the PCR: forward 5'-GCC ATG GGA AAC GGC GTG TAC GAC GTC GGC GG-3' and reverse 5'-GGT ACC AAG CTT TCA ATG ATG ATG ATG ATG ATG CGC GAC CGC CTT-3'. The PCR product (βα-His_6 genes) was subcloned into the pSC-B-amp/kan vector using the Strataclone Blunt PCR cloning kit (Agilent). The βα-His_6 genes were subsequently subcloned between the *Nco*I and *Hind*III restriction sites of the kanamycin resistant pET28a$^+$ (Novagen) to create the *Pt*-His_6/pET28a$^+$ plasmid. The nucleotide sequence for the *Pt*NHase activator gene was obtained from the GeneBank, ID HV233497.1, and used to synthesize the gene with *E. coli* codon usage and cloned into a pIDT-SMART (Integrated DNA Technologies, Inc.) ampicillin resistant vector with *Nde*I and *Hind*III restriction sites. Subsequently, the *Pt*NHase activator gene was inserted between the *Nde*I and *Hind*III restriction sites of the ampicillin resistant pET21a$^+$ (Novagen) vector to create the *Pt*-activator/pET21a$^+$ plasmid. All plasmid sequences were confirmed using the automated DNA sequencing at the University of Chicago Cancer Research Center DNA sequencing facility.

Expression and purification of recombinant PtNHase. The *Pt*-His_6/pET28a$^+$ and *Pt*-activator/pET21a$^+$plasmids were co-transformed into *E. coli* BL21(DE3) competent cells (Agilent) for expression. A 100 mL LB-Miller starter culture was inoculated from a single colony with 50 μg/mL and 100 μg/mL of kanamycin and ampicillin, respectively. A 6 L culture was inoculated from this starter culture using 7 mL per liter and grown at 37 °C until an $O.D._{600nm}$ of 0.6-0.8 was reached. The culture was cooled to 20 °C, induced with 0.1 mM isopropyl β-D-1-thiogalactopyranoside (IPTG), supplemented with 0.25 mM $CoCl_2$ (57,106), and expressed at the same temperature for 16-18 h. Cells were harvested by centrifugation at 6,370 *g* 4 °C, for 5 min. The cells were resuspended at 3 mL per gram of buffer A (50 mM NaH_2PO_4, pH 7.5, 500 mM NaCl, 10 mM imidazole) then lysed by sonication on ice for 8 min (30 s on, 45 s off) using a 21W Misonex sonicator 3000. Cell debris was removed by two rounds of centrifugation at 31,000 *g*, 4 °C, for 20 min. The protein was purified by immobilized metal affinity chromatography (IMAC) using a 5 mL Ni-NTA (nickel-nitrilotriacetic acid) Superflow Cartridges (Qiagen). The column was equilibrated with buffer A and the crude extract was loaded onto the column. Unbound protein was washed with 15 column volumes (CV) of buffer A with 25 mM imidazole. The protein was eluted with a linear gradient (0-100%) of buffer B (buffer A with 500 mM imidazole) over 20 CVs at a flow rate of 2 mL/min. Peak fractions were pooled and concentrated with an Amicon Ultra-15 centrifugal filter device with a molecular weight cutoff (MWCO) of 30,000 (Millipore). The concentrated sample (2 mL) was applied to a 16/60 Superdex 200 prep grade (GE Healthcare) column equilibrated with buffer C (50 mM HEPES pH 7.5, 300 mM NaCl) for gel filtration chromatography and the protein was eluted from the column over 1.5 CVs of buffer C.

The peak fractions were pooled and buffer exchanged into 50 mM HEPES pH 7.0 using an Amicon Ultra-15 centrifugal filter device. The purity of *Pt*NHase was analyzed by using 12.5% SDS-PAGE (Figure 16). The protein concentration was determined by UV absorbance at 280 nm using a calculated molar extinction coefficient of 174, 640 M^{-1} cm^{-1} and the Coomassie (Bradford) Protein Assay Kit (Thermo Scientific). The calculated molecular mass of the heterotetramer was 101 kDa. Theoretical molecular mass and protein extinction coefficients were calculated with the ExPASy ProtParam tool (107).

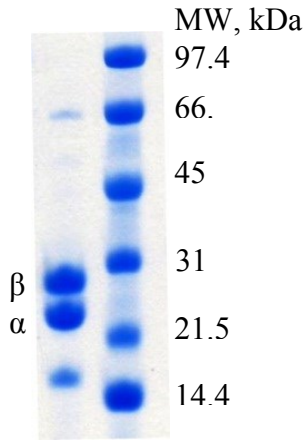

Figure 16. SDS-PAGE of purified *Pt*NHase. *Lane 1* purified *Pt*NHase and *lane 2* molecular weight standards.

Kinetic assay. The kinetic constants were determined by measuring the hydration of acrylonitrile to acrylamide in 50 mM Tris-HCl, pH 7.5 at 25 °C. The rate of the acrylonitrile hydration was followed continuously by monitoring the increase in absorbance at 225 nm using an absorption coefficient of $\Delta\varepsilon_{225} = 2.9$ mM^{-1} cm^{-1}. Assays were performed in a 1 mL quartz cuvette on a Shimadzu UV-2450 PC spectrophotometer equipped with a TCC temperature controller, in triplicate from three independent enzyme samples. The reaction was initiated by adding the enzyme to the reaction mixture (1 mL)

containing various final concentrations of the substrate (0-60 mM). One unit of enzyme activity was defined as the amount of enzyme that catalyzed the production of 1 μmol of acrylamide per minute at 25 °C.

PtNHase inhibition with 1-butaneboronic acid. For determination of the inhibition constant, the kinetic assay was performed as describe above with the addition of various final concentrations of BuBA to the assay mixture and fixed concentrations of acrylonitrile. The reactions were initiated by the addition of *Pt*NHase (final concentration of 3-4 nM). The initial velocity data were analyzed by nonlinear regression with the Enzyme Kinetics Module in SigmaPlot 12.3 (Systat Software, San Jose, CA) using the *Single Substrate-Single Inhibitor* function to determine the inhibition mechanism and the K_i constant.

Slow-binding inhibition by phenylboronic acid: assay started with enzyme. For determination of the kinetic inhibition constants, the kinetic assay was performed as describe above with the addition of various final concentrations of PBA to the assay mixture. The reactions were initiated by the addition of *Pt*NHase (final concentration of 0.56-0.7 nM) and monitored continuously for 10 min (Figure 17A).

Slow-binding inhibition by phenylboronic acid: assay started with enzyme-inhibitor complex. *Pt*NHase (188-237 nM) was preincubated for 60 min at room temperature with PBA (0-2.4 μM) to form the enzyme-inhibitor complex. Reactions were initiated by the addition of 3 μL of the preincubation mixture to a 1 mL reaction mixture containing the substrate (Figure 17B); this resulted in a 333-fold dilution of the enzyme and inhibitor (0.56-0.7 nM *Pt*NHase and 0-7.2 nM PBA, final concentrations).

Dialysis of the enzyme-inhibitor complex. The reversibility of the *Pt*NHase-PBA was examined. *Pt*NHase (0.2 μM) was preincubated with 20 μM of PBA for 1 h at room temperature. A control sample that contained no inhibitor was also prepared. After the 1 h preincubation, 3 μL of each sample was taken and used to initiate a 1 mL reaction containing 8 mM acrylonitrile. The remaining of the samples were subjected to overnight dialysis at 4 °C in 50 mM HEPES pH 7.5 and 300 mM NaCl. Dialysis was performed in a 0.5 mL Slide-A-Lyzer® G2 Dialysis Cassette (Thermo Scientific) with molecular-weight cutoff of 10 K. After overnight dialysis, 3 μL of each sample was taken and used to initiate a 1 mL reaction containing 8 mM acrylonitrile. The final concentration of enzyme and inhibitor in the reaction was 0.6 nM and 60 nM, respectively. The dialyzed sampled regained ~100% of its activity showing that PBA is a slow-binding reversible inhibitor of *Pt*NHase.

Data analysis: slow-binding inhibition by phenylboronic acid. The slow-binding inhibition properties of PBA were analyzed assuming the mechanism in Figure 10, where K_i ($K_i = k_1/k_2$) is the equilibrium inhibition constant for the formation of the initial complex, EI, k_1 and k_2 are the forward and reverse rate constants for the equilibrium between the EI and the EI* complex (96). The overall inhibition constant (K_i^*) is described by $K_i^* = K_i\, k_4/k_3 + k_4$ (Figure 10) (96). The reaction time courses (Figure 17) were fit to Equation 1 using OriginPro 9.0 (OriginLab, Northampton, MA), where A is the change in absorbance at 225 nm at any time t, v_0 is the initial velocity, v_s is the final steady-state velocity, k_{obs} is the apparent first-order rate constant for the interconversion between v_0 and v_s, and A_0 is included to correct any possible deviation from the baseline. The initial and final steady-states velocities were then analyzed

separately by nonlinear regression with the Enzyme Kinetics Module in SigmaPlot 12.3 (Systat Software, San Jose, CA) using the *Single Substrate-Single Inhibitor* function to determine the inhibition mechanism and the K_i and K_i^* constants, respectively.

$$A = v_s\, t + \frac{(v_0 - v_s)(1 - e^{-k_{obs}t})}{k_{obs}} + A_0 \qquad (1)$$

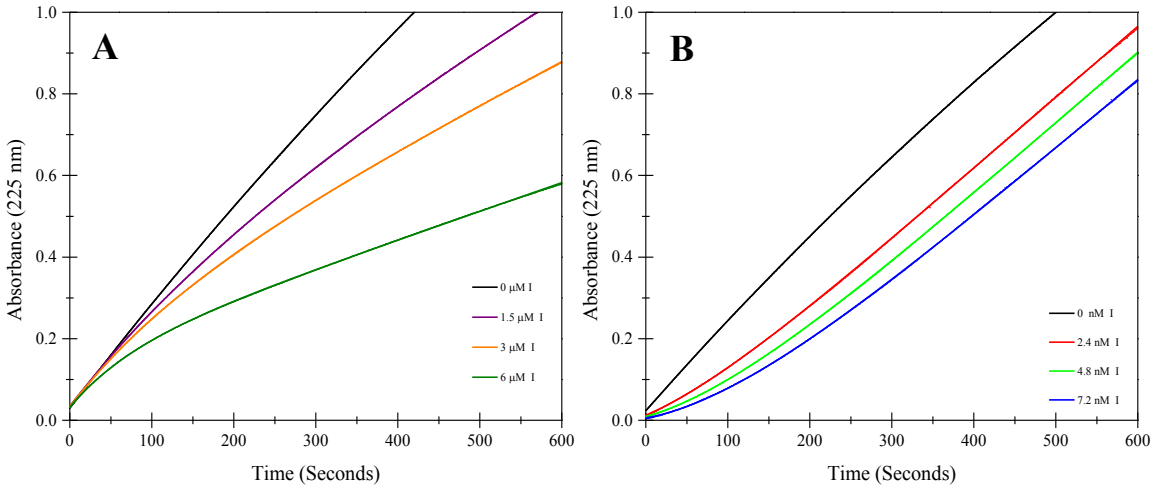

Figure 17. Example of progress curves for the slow-binding inhibition of *Pt*NHase by PBA. **A)** Reaction progress curves (monitored at 225 nm for 10 min) for the hydration of 10 mM acrylonitrile by 0.56 nM *Pt*NHase in the presence of the indicated concentration of PBA in 50 mM Tris-HCl pH 7.5 at 25 °C. The reactions were initiated by the addition of *Pt*NHase. **B)** Reaction progress curves for the hydration of acrylonitrile by reactivated *Pt*NHase. *Pt*NHase (237 nM) was preincubated with various concentrations of PBA (0 – 2.4 µM) for 60 min at room temperature. The preincubated *Pt*NHase/inhibitor complex was diluted 333-fold into reaction buffer containing 10 mM acrylonitrile to initiate the hydration reaction under the same conditions as in panel A. The reaction time courses were fit by nonlinear regression to Equation 1 to obtain the v_0, v_s, and k_{obs} values.

Crystallization and data collection. Crystallization of *Pt*NHase was performed following the previously reported protocol with slight modifications in freezing and soaking conditions; the native crystals grew in the published condition containing 1.4 M sodium citrate tribasic and 0.1 M HEPES (44,57). For co-crystallization with inhibitors,

10 μL of 25 mg/mL *Pt*NHase was mixed with a 10 μL reservoir solution and 2 μL of 100 mM inhibitor, BuBA or PBA. Diffraction quality crystals (Figure 18) grew within two weeks and belonged to the space group $P3_221$ with one copy of heterodimer in the asymmetric unit. For X-ray data collection, these crystals were briefly transferred to the reservoir solution containing 10 mM inhibitor and 20% (v/v) glycerol as cryo-protectant before flash-cooling by plunging in liquid nitrogen. The crystals of NHase with both BuBA and PBA were also obtained by soaking a native crystal for ~20 seconds in reservoir solution containing 10 mM inhibitor and 20% (v/v) glycerol. The crystals were then flash-cooled. Crystallographic data were collected on beamlines 23ID-B or 23ID-D of GM/CA@APS of the Advanced Photon Source (APS) using X-rays of 0.99Å wavelength and Rayonix (formerly MAR-USA) 4×4 tiled CCD detector with a 300 mm^2 sensitive area. All data were indexed, integrated, merged and scaled with HKL2000 (108). Crystal parameters along with data collection and processing statistics are given in Table 2.

Figure 18. Crystals of native *Pt*NHase. Crystallization by the sitting-drop vapor diffusion method in 1.4 M tri-sodium citrate and 0.1 M HEPES at 4 °C.

Phasing, model building, and refinement. Phasing of native NHase crystals was carried out with molecular replacement using the program Phaser from the CCP4 software suite. The structure of *Pt*NHase (PDB ID: 1IRE) (44), without any water molecules and ligands except for the cobalt ion, was used as the starting search model. Initial R_{free} and R factor for the correct solution were 27.0 and 26.9, respectively. Rigid body refinement was followed by restrained refinement with Refmac5(109) and further manual model inspection and adjustments with Coot (110). When refinement converged, solvent molecules were added over several rounds. The R_{free} and the R factor values of the final model of the native structure were 20.2% and 17.5%, respectively (Table 2).

The NHase structures in complex with the BuBA and PBA inhibitors were phased by molecular replacement using the refined coordinates of native NHase as the search model. Refinement of the complex structures was carried out following the same protocol as the native structure. To avoid model bias, no ligand coordinates were included until the later stages of the refinement. The f_o-f_c difference maps (experimental maps), before incorporation of inhibitors in each structure show well-defined electron density for the corresponding inhibitor (Figures 11, 12, 13, and 14).

Inhibitor structures were created in Chemdraw (a "Mol" file); the molecules were regularized and chemical restraints were generated in JLigand. The inhibitors were placed into residual electron density in COOT after the rest of the structure, including most of the solvent molecules, were refined. Final rounds of refinements were conducted in PHENIX (111) to include occupancy and simulated-annealing refinements. The R_{free} and R factor for the NHase structures with soaked BuBA, co-crystallized BuBA, and co-crystallized PBA were 18.3 % and 15.2 %, 16.6 % and 14.2 %, and 18.6 % and 15.2 %,

respectively (Table 2)

Table 2. Data Collection and Refinement Statistics for *Pt*NHase Crystal Structures.

Data set	Native	*Pt*NHase BuBA Soaking	*Pt*NHase BuBA Co-crystal	*Pt*NHase PBA Co-crystal
Space Group	$P3_221$	$P3_221$	$P3_221$	$P3_221$
Cell Dimensions				
a = b (Å)	65.82	65.6	65.9	65.7
c (Å)	185.61	185.7	186.2	185.7
α = β (°)	90	90	90	90
γ (°)	120	120	120	120
Resolution (A)	54.0-1.9	36.0-1.5	36.1-1.6	31.0-1.2
[a]R_{merge} (%)	12.7(40.6)	8.7(82.4)	6.0(20.7)	8.5 (67.9)
I/sigma	8.4(3.8)	16.3(1.5)	18.2(7.6)	9.4 (1.4)
Completeness (%)	99.8(99.8)	99.7(99.2)	100(100)	95.4(71.0)
Multiplicity	5.0(4.4)	4.5 (4.4)	6.6(6.3)	6.2(2.9)
No. Total reflections	176494	323576	390048	859631
No. Unique reflections	35437	72603	59389	139129
[b]R_{work} / [c]R_{free} (%)	17.5/20.2	15.2/18.3	14.2/16.6	14.5/18.5
No. of Atoms	4005	4175	4315	4169
No. of Solvent Atoms	460	543	748	629
B-factors (Å^2)				
Overall	23.3	20.4	15.8	15.7
Protein	22.2	17.9	13.2	13.8
Boronic Acid Ligand	ND	10.4-33.7	22.1-28.7	13.3-17.1
Water	31.8	30.9	27.8	27.8
[d]RMSD Bond Length (A)	0.02	0.02	0.02	0.02
[d]RMSD Bond Angles (°)	1.09	1.14	1.83	1.50
Ramachandran				
Favored (%)	98.0	96.3	96.2	97.7
Allowed (%)	1.5	2.3	2.4	1.8
Outlier (%)	0.5	1.4	1.4	0.5

The values for the highest resolution bin are in parentheses.
[a]Linear $R_{merge} = \Sigma|I_{obs}-I_{avg}|/ \Sigma I_{avg}$. [b]$R_{cryst} = \Sigma|F_{obs}-F_{calc}|/ \Sigma F_{obs}$.
[c]Five percent of the reflection data were selected at random as a test set and only these data were used to calculate R_{free}.
[d]RMSD, root mean square deviation.
ND, Not Determined/Calculated by the program

CHAPTER THREE

THE IRON NITRILE HYDRATASE FROM *COMAMONAS TESTOSTERONI* NI1 DOES NOT REQUIRE AN ACTIVATOR ACCESSORY PROTEIN FOR EXPRESSION IN *ESCHERICHIA COLI*

Research Aim

It is widely accepted that the activators or accessory proteins are necessary for the successful expression of a functional NHase; however, one NHase does not follow this rule. The Fe-NHase from *Comamonas testosteroni* Ni1 (*Ct*NHase), for which an activator protein had not been reported, was expressed in *E. coli* as a soluble enzyme with the co-expression of the molecular chaperones GroES/EL (112). In the absence of the molecular chaperones, the yield and activity *Ct*NHase was significantly lower than that obtained when co-expressed with the molecular chaperones, since most of the enzyme was found as an inclusion body (112). It was proposed that, similar to the NHase activator, the molecular chaperones GroES/EL assisted with enzyme solubility and metal incorporation. However, the proposition that the molecular chaperones were helping with metal incorporation was unexpected because several previous studies established that the GroES/EL chaperones assist in the correct folding of the protein preventing it from going to inclusion bodies (113,114). With the aim of obtaining a functional NHase and understanding the role of the NHase activator or accessory proteins *Ct*NHase was expressed in the absence of an activator protein and the molecular chaperones GroES/EL.

In addition, as a control the Fe-type NHase *Rhodococcus equi* TG328-2 (*Re*NHase) for which an activator protein is known was also investigated.

Expression and Purification of Recombinant *Ct*NHase

*Ct*NHase was expressed in *E. coli* without the co-expression of the *E. coli* molecular chaperones GroES/EL or an activator protein but with *E. coli* codon usage and a hexahistidine tag on the C-terminus of the β-subunit. Expression of *Ct*NHase and purification using IMAC resulted in ~10 mg/L of soluble *Ct*NHase enzyme (Figure 19). Kinetic characterization of *Ct*NHase using acrylonitrile as the substrate provided a k_{cat} of 71 ± 5 s^{-1} and a K_m of 350 ± 50 mM. Since the turnover rate is more than 7-fold higher than any previous report for *Ct*NHase (62,112,115), it was hypothesized that the metal ion was properly inserted and both active site Cys residues were properly oxidized in the absence of an activator protein, which is required for full enzymatic activity (103). For comparison purposes, the Fe-type *Re*NHase was co-expressed with its activator protein (*Re*NHase^{+Act}), purified, and kinetically characterized. Using acrylonitrile as the substrate, the enzyme exhibited a k_{cat} of 2,400 s^{-1} and a K_m of 4.3 ± 1.7 mM, which is in good agreement with previous studies (116). Although expression of *Re*NHase in the absence of its activator protein (*Re*NHase^{-Act}) produced soluble protein, no enzymatic activity was observed, most likely due to its inability to incorporate metal in the absence of an activator protein.

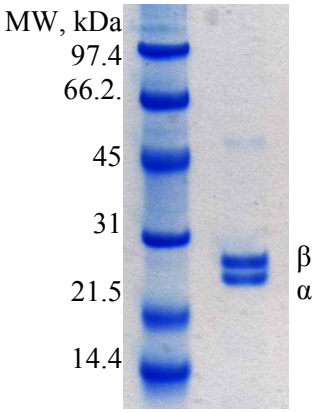

Figure 19. SDS-PAGE of purified *Ct*NHase. *Lane 1* purified *Ct*NHase and *lane 2* molecular weight standards.

Metal Analysis and UV-Visible Spectroscopy

A combination of UV-Visible spectroscopy and metal analysis was used to determine if *Ct*NHase, *Re*NHase^{+Act} and *Re*NHase^{-Act} contained their full complement of Fe(III). After purification, the *Ct*NHase and *Re*NHase^{+Act} enzymes exhibited an emerald green color, whereas the *Re*NHase^{-Act} was colorless. The UV-Vis spectra for *Ct*NHase and *Re*NHase^{+Act} show the characteristic S → Fe(III) ligand-to-metal-charge-transfer (LMCT) band at ~700 nm (ε = ~6,000 $cm^{-1}M^{-1}$and 3,500 $cm^{-1}M^{-1}$, respectively), however no absorbance was detected for *Re*NHase^{-Act} (Figure 20). ICP-AES data indicate that *Ct*NHase contained ~1.6 irons per $\alpha_2\beta_2$ heterotetramer, *Re*NHase^{+Act} had ~1.7 equivalents of iron per $(\alpha\beta)_2$ heterotetramer, while no iron was detected for *Re*NHase^{-Act}. These data clearly indicate that *Re*NHase strictly requires the co-expression of its corresponding Fe-type activator for an active enzyme and the presence of an affinity tag plays no role in metal incorporation. They also confirm that *Ct*NHase contains its full complement of Fe(III) metal and can thus be expressed in *E. coli* in the absence of an Fe-type NHase activator protein or the *E. coli* molecular chaperones GroES/EL.

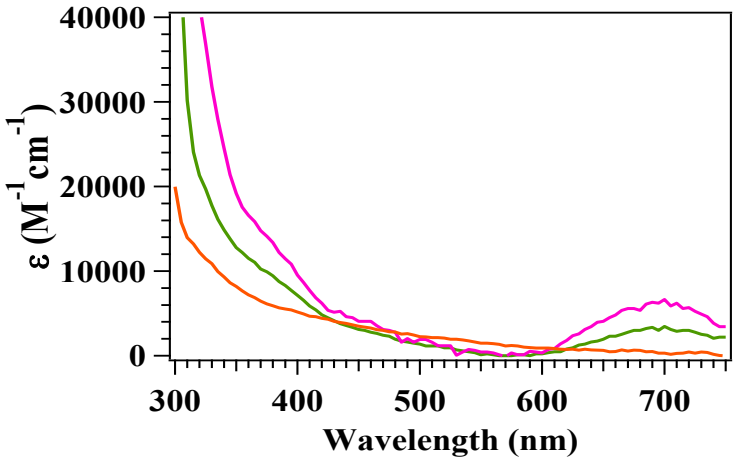

Figure 20. UV-Visible spectra of *Ct*NHase Ni1 (—), *Re*NHase TG328-2 (—) co-expressed with activator, and *Re*NHase TG328-2 co-expressed without activator (—).

Crystal Structure of *Ct*NHase

The three-dimensional X-ray crystal structure of *Ct*NHase was determined to 2.4 Å resolution. The structure verifies that the recombinant *Ct*NHase binds its full complement of iron and, in general, is structurally similar to other Fe-type NHase enzymes (Figure 21). The α-subunit of *Ct*NHase is embedded in the center of the β-subunit, while the N-terminus of the α-subunit forms a helix that is embedded among three helices from the β-subunit (Figure 21A). Supported by ICP-AES data, we set the occupancies of the Fe(III) ion and its coordination residues at 0.8 during structural refinement resulting in satisfactory electron density maps and good R_{free}/R values. The Fe(III) ions in *Ct*NHase are five coordinate and bound by C99, C102, and C104 as well as two backbone amide nitrogens, where C102 and C104 are both oxidized to cysteine-sulfinic acids (CSA) (Figure 21B). The full oxidation of the equatorial Cys residues is expected since crystals of *Ct*NHase were obtained under aerobic conditions over the course of a week. Two amide nitrogen atoms and the oxidized sulfur atoms are roughly

in the same plane as the metal ion. The sulfur atom from C99 forms a coordination bond roughly perpendicular to this plane, which results in a slightly distorted square-based pyramidal geometry. On the opposite side of C99, no sixth ligand such as NO or a water molecule is present as is often observed for Fe-type NHase enzymes (49), which is possibly due to the resolution of the present structure. A phosphate ion is present in the active site, likely due to phosphate (1.57 M) in the crystallization buffer (Figure 21B). This phosphate ion forms hydrogen bonds with α-H80 (2.6 Å) and α-H81 (2.8 Å) along with α-R157 (2.9 Å and 2.8 Å from two nitrogen atoms, respectively) and an oxygen atom of CSA104 (2.6 Å). Interestingly, these histidine residues are not strictly conserved in the α-subunits of Fe-type NHase enzymes.

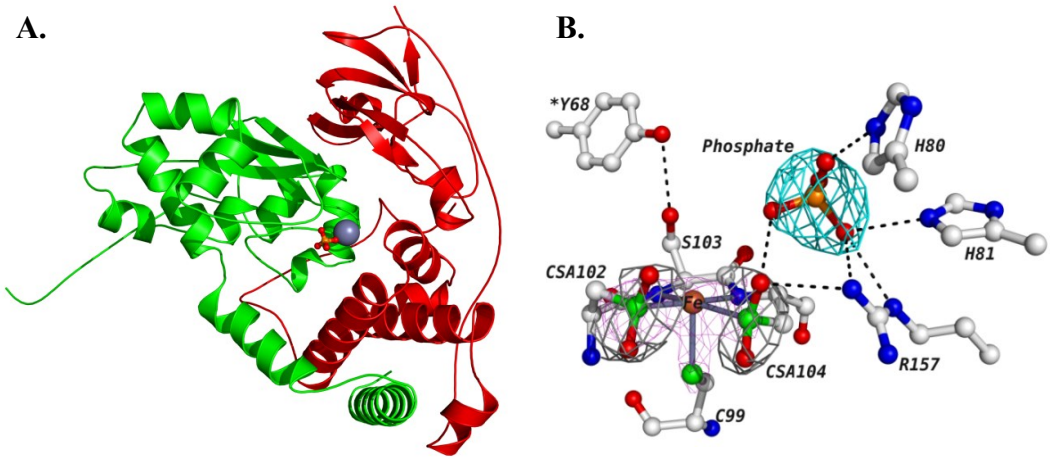

Figure 21. Structure of the *Ct*NHase heterodimer (PDB ID: 4FM4). **A**) The α-subunit is in green and β-subunit is in red. The iron ion is shown as a grey sphere and the phosphate ion bound to the active site is shown in ball-and-stick form. **B**) *Ct*NHase active site containing a phosphate ion in ball-and-stick form, the iron ion is shown as an orange sphere, bonds are shown as silver sticks, and hydrogen bonds are shown as dashed lines. The asterisk indicates that Y68 is from the β-subunit. Electron density maps ($2F_o$-F_c) are shown around key chemical groups: the two sulfinic acid groups are shown in grey at 1.2 σ while the maps around the heavy atom are shown in magenta at 3.4 σ. The ($2F_o$-F_c) maps around the phosphate ion are shown in cyan at 2.2 σ. (Contour levels of the electron density maps are adjusted for both validation and clarity.)

Structural comparison of the *Ct*NHase model and the Fe-NHase from *Rhodococcus sp*. 312 (1AHJ) (42), which exhibits ~50% identity to *Ct*NHase, indicates that the two structures are very similar with a core rmsd (root mean square deviation) of 1.13 Å. Three regions of the *Ct*NHase are different from 1AHJ (Figure 22A). These include the C-terminal region of the α-subunit, the N-terminus of the α-subunit, and a loop region (76-83) of α-subunit just above the Fe(III) active site. Neither this loop region in *Ct*NHase nor the equivalent loop region (88-94) in 1AHJ is involved in any crystallographic contact. It is therefore unlikely that the structural differences are caused by mildly different crystallization conditions (pH 7 vs. pH 8.5). Alteration of this loop region above the active site results in the formation of an unusually wide-open solvent accessible active site (Figure 22B). This accessibility provides a direct approach for the substrate to the active site and coincides directly with the unfilled axial position of the Fe(III) ion (Figure 32B). Typically, the trivalent metal ions of both Co- and Fe-NHase enzymes are buried and accessible only through narrow channels (49). The solvent inaccessibility of the trivalent metal ions in NHases has been implicated in observed substrate specificities, as well as the difficulty in preparing the apo- or metal substituted forms of NHases (49). In the contrast, the narrow substrate channel observed for 1AHJ requires that the substrate approach the metal center at a 60^{o} angle off of the axial position (Figure 22C). In 1AHJ, the side chains of α-Y40, α-W44, α-W118, β-Y37, β-M40 and β-F41 block a direct axial approach to the Fe(III) ion. None of the above residues are conserved and all are significantly bulkier than the spatially related residues in *Ct*NHase.

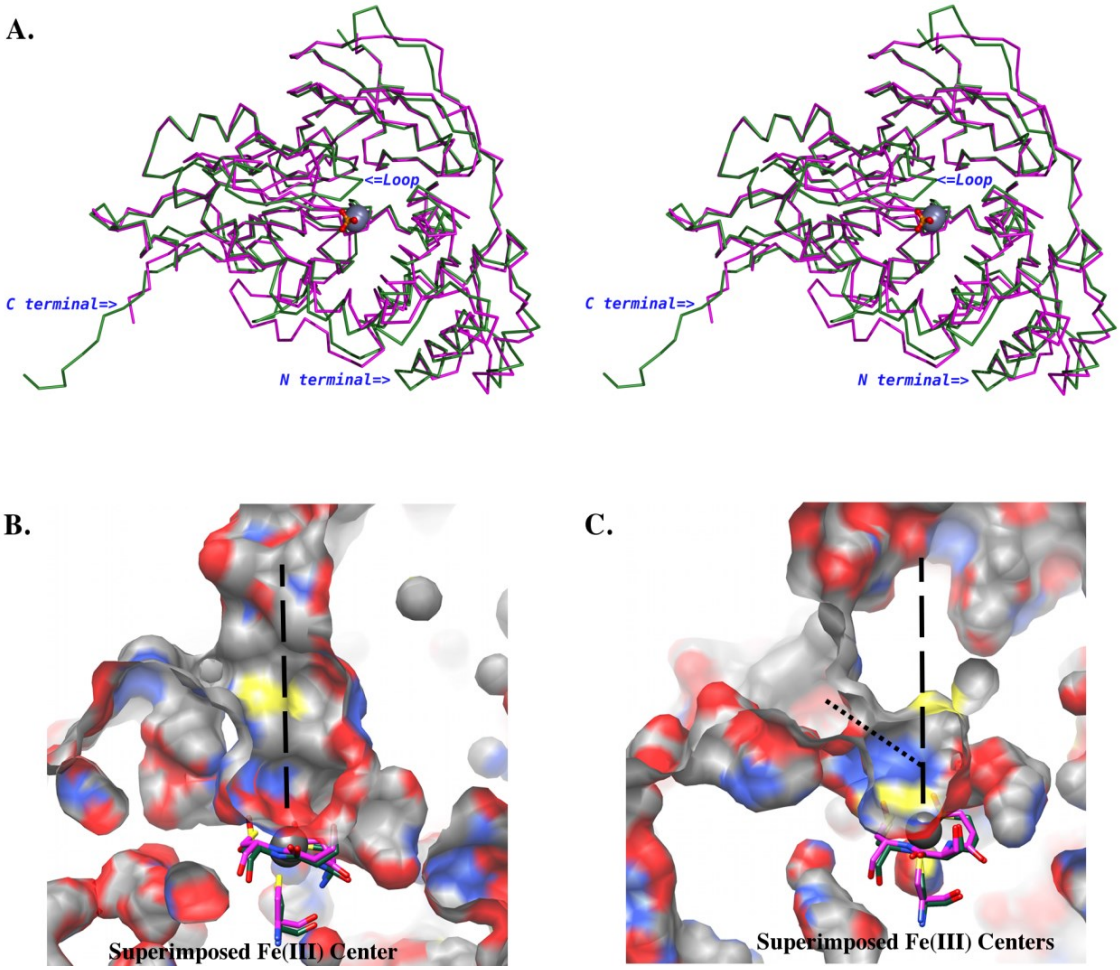

Figure 22. Structural comparison of *Ct*NHase (PDB ID: 4FM4) and the Fe-NHase from *Rhodococcus* sp. R312 (PDB ID: 1AHJ). **A)** A wall-eyed stereo display of the superposition of *Ct*NHase and 1AHJ. The *Ct*NHase structure is in green and the 1AHJ model is in magenta. Three regions with pronounced differences in the protein backbones occur between the two α-subunits and are indicated in the *Ct*NHase structure with labels at the two terminal regions and a loop region (76-83) above the metal center. **B)** Surface representation of the *Ct*NHase heterodimer showing the solvent accessible channel with the active site iron as a grey sphere. The Fe(III) centers of *Ct*NHase and 1AHJ are superimposed. The metal ligands displayed are shown in stick form; the carbon atoms for the residues in *Ct*NHase are green; the carbon atoms of the residues in 1AHJ are blue. The Fe(III) ion in *Ct*NHase is shown as a silver sphere. A dashed line indicates the axial direction of the metal constellation. **C)** Surface representation of 1AHJ showing the solvent accessible channel. The superimposed Fe(III) centers are show as in B.

Summary

In summary, this construct for *Ct*NHase is the first functional expression system for an Fe-NHase that does not require an NHase activator protein or the *E. coli* molecular chaperones GroEL/ES. These data are contrary to the accepted view regarding the strict requirement of co-expressing NHases with activator proteins for fully active enzymes. Based on the X-ray crystallographic data *Ct*NHase binds it full complement of Fe(III) ions in its active site and the equatorial Cys residues are appropriately oxidized, which is a requirement for full enzymatic activity. Both metal ion insertion and Cys oxidation are functions previously ascribed to the NHase activator protein. The structure of *Ct*NHase reveals that the Fe(III) ion in the active site is solvent exposed and resides at the bottom of an open cavity. This exposed active site not only provides a much more direct route for substrates, but also for metal ion incorporation. It is possible that the solvent accessibility of the *Ct*NHase active site, both the large opening and the axial approach direction, provides the necessary access for metal ion incorporation without the use of an activator protein. Moreover, the two non-conserved His residues that reside near the active site Fe(III) ion at the bottom of the solvent exposed channel, may play a role in assisting in the incorporation of iron ions into the active site. In summary, these studies were published in the in the journal of Biochemical and Biophysical Research Communications: Misty L. Kuhn, Salette Martinez, Natalie Gumataotao, Uwe Bornscheuer, Dali Liu, Richard C. Holz, *Biochemical and Biophysical Research Communications*, **2012**, *424*, 365-370.

Experimental Procedures

Materials. Acrylonitrile was purchased from Sigma-Aldrich. Synthesized genes and primers were purchased from Integrated DNA Technologies, Inc., (IDT). All other materials were purchased at the highest quality available.

Plasmid construction. The α- and β-subunit genes of *Ct*NHase were individually synthesized with optimized *E. coli* codon usage and were cloned into the pIDT-SMART kanamycin resistant vector. Protein sequences for the α- and β- subunit genes were obtained from Cerbelaud *et al*. (117). Restriction sites were *NcoI* and *HindIII* for the α-subunit gene and *NdeI* and *KpnI* for the β-subunit. A polyhistidine (His_6) affinity tag was engineered onto the C-terminus of the β subunit using Phusion DNA polymerase (New England Biolabs) and the following primers: forward 5'-GCA CCC ATA TGG ACG GCA TGC-3' and reverse 5'-GGT ACC TTA ATG ATG ATG ATG ATG GTG CAC CTC TGC G-3'. The PCR product was sub-cloned into the pSC-B-amp/kan vector using the Strataclone Blunt PCR cloning kit (Agilent). The α- and β-C-His_6 subunit genes were sub-cloned into MCSI and MCSII of the kanamycin resistant pCOLADuet-1 expression vector (Novagen), respectively, to create the plasmid pSMCtαβHis. The sequence was confirmed using automated DNA sequencing at the University of Chicago Cancer Research Center DNA sequencing facility.

CtNHase expression in the absence of an activator protein. The *Ct*NHase α- and β-subunits (~23 and ~23.5 kDa, respectively) were expressed alone, without co-expressing an Fe-type activator protein or the *E. coli* chaperones GroES/EL, in the following manner. The plasmid pSMCtαβHis was freshly transformed into BL21(DE3) competent cells (Agilent), and a single colony was used to inoculate 50 mL of LB-Miller

culture containing 50 μg/mL kanamycin with shaking overnight at 37 °C . This culture (~7 ml) was used to inoculate a 1 L culture and the cells were grown at 37 °C until the OD_{600nm} reached 0.6-0.8. The culture was cooled on ice, induced with 0.1 mM isopropyl β-D-1-thiogalactopyranoside (IPTG), and expressed at 20 °C for 16 hours. Cells were harvested by centrifugation at 5000 *g* and 4 °C for 5 min in a Beckman Coulter Avanti JA-10 rotor. Cell pellets were resuspended in buffer A (50 mM Na_2HPO_4 pH 7.5, 300 mM NaCl, 10 mM imidazole) at a ratio of 5 mL per gram of cells, then sonicated for 4 min (30 s on 45 s off) at 21W using a Misonix sonicator 3000. The crude extract was obtained after centrifugation in a JA-20 rotor at 15,000 *g* and 4 °C for 20 min. The sample was subjected to another round of centrifugation before purification to remove particulate matter.

Rhodococcus equi TG328-2 nitrile hydratase (ReNHase) expression in the presence and absence of an activator protein. The *Rhodococcus equi TG328-2* nitrile hydratase (*Re*NHase) and activator plasmids were obtained from Bornscheuer *et al*. (116). The *Re*NHase gene was sub-cloned into the ampicillin resistant $pET21a^+$ expression vector and the activator gene into the kanamycin resistant $pET28a^+$ expression vector using *NdeI* and *HindIII* restriction sites. *Re*NHase was expressed in the presence (*Re*$NHase^{+Act}$) or absence (*Re*$NHase^{-Act}$) of its Fe-type activator protein as previously described (116).

Purification of CtNHase and ReNHase co-expressed with ($ReNHase^{+Act}$*) and without activator (*$ReNHase^{-Act}$*).* Crude extracts of *Ct*NHase, *Re*$NHase^{+Act}$, or *Re*$NHase^{-Act}$ were loaded onto a 5 ml Ni-NTA (nitrilotriacetic acid) Superflow Cartridge (Qiagen) for immobilized metal affinity chromatography (IMAC) using an ÄKTA FPLC P-960.

The column was washed with four column volumes (CVs) of buffer A, and the protein was eluted with a linear gradient (0-100%) of buffer B (buffer A with 500 mM imidazole) over 20 CVs at a flow rate of 1 ml/min. Active protein fractions were pooled and concentrated with an Amicon Ultra-15 10,000 MWCO centrifugal filter unit (Millipore) resulting in ~10 mg/L of soluble *Ct*NHase and ~50 mg/L of *Re*NHase^{+Act}. Protease inhibitors or butyric acid was not required during purification of *Ct*NHase, but 40 mM *n*-butyric acid was included in all buffers for *Re*NHase purification. For crystallization trials, *Ct*NHase was further purified using a HiLoad 16/60 Superdex 200 prep grade gel filtration column (GE Healthcare). The protein eluted over one CV of buffer C (50 mM HEPES pH 7.5, 300 mM NaCl) at a flow rate of 0.5 ml/min. The fractions were pooled, concentrated, and buffer was exchanged to 50 mM HEPES pH 7.0 using an Amicon Ultra-15 10,000 MWCO centrifugal filter unit.

Purified protein samples were analyzed by SDS-PAGE with a 12.5% polyacrylamide SPRINT NEXT GEL™ (Amresco). Gels were stained with Gel Code Blue (Thermo-Fisher Scientific). Protein concentration of crude extracts was determined using a Coomassie (Bradford) Protein Assay Kit (Pierce) and pure protein by measuring the absorbance at 280 nm. Theoretical molecular weights and protein extinction coefficients were calculated with the ExPASy compute pI/Mw tool (107). The molecular weight for the *Ct*NHase tetramer was 92,828 g/mol with an extinction coefficient of 118,720 cm^{-1} M^{-1}. For the *Re*NHase tetramer, a molecular weight of 97,888 g/mol was calculated with an extinction coefficient of 149,660 $cm^{-}1$ M^{-1}.

Kinetic analysis of CtNHase, ReNHase^{+Act}, and ReNHase^{-Act}. The enzymatic activity of *Ct*NHase, *Re*NHase^{+Act}, and *Re*NHase^{-Act} towards acrylonitrile (225 nm, ε =

2.9 $mM^{-1}cm^{-1}$) was measured using a Shimadzu UV-2450 spectrophotometer. A 1 ml reaction consisted of 50 mM Tris-HCl buffer pH 7.5 (*Ct*NHase) or 50 mM phosphate buffer pH 7.5 (*Re*NHase^{+Act} and *Re*NHase^{-Act}) and various concentrations of acrylonitrile. All assays were performed at room temperature and data analysis was performed using Origin Lab 7.5. The kinetic constants V_{max} and K_m (k) were calculated using the equation [$y = V_o + (V_{max} - V_o)\ (x^n/(k^n + x^n))$] where n = 1 and V_o is zero to give the equation $y = V_{max}*(x/(k + x))$. One unit (U) of NHase activity is defined as the formation of 1 μmol of acrylamide per minute.

Metal analysis. Protein samples for *Ct*NHase (0.15 mg/ml), *Re*NHase^{+Act} (0.15 mg/ml), and *Re*NHase^{-Act} (0.19 mg/ml) were digested with concentrated nitric acid at 70 °C for 10 minutes and then cooled to room temperature. These samples were diluted to 5 ml total volume with deionized water to give a final nitric acid concentration of 5%, and were filtered using 0.2 μm Supor membrane syringe filters (Pall). A nitric acid blank was also prepared. The samples were analyzed using inductively coupled atomic emission spectroscopy (ICP-AES) at the Integrated Molecular Structure Education and Research Center (IMSERC) at Northwestern University (Evanston, IL, USA).

CtNHase crystallization and data collection. Crystals of *Ct*NHase were obtained by the hanging drop vapor diffusion method. The initial sparse matrix screen was carried out using a Gryphon crystallization robot from Art Robbins Inc. with commercial screen sets including Wizard Screen I-IV from Emerald Biosystems (Bainbridge Island, WA, USA) and Crystal Screen I-II, Peg Ion Screen, Index Screen I-II, and Crystal Screen Cryo from Hampton Research. Once initial crystallization conditions were obtained, they were optimized manually by varying all component concentrations. Optimized conditions

were: 1 µl of purified *Ct*NHase (15, 20, or 30 mg/ml) in 50 mM HEPES pH 7.0 with an equal volume of the crystallization reservoir solution (1.08 M K_2HPO_4, 0.49 M NaH_2PO_4 with 25 or 30% (v/v) glycerol). The best quality *Ct*NHase crystals were obtained at 20 °C after 5 days (Figure 23). For X-ray data collection, the crystals were soaked in the reservoir solution with 30% (v/v) glycerol as a cryo-protectant before flash freezing in liquid nitrogen. Data sets were collected at the SBC 19-ID beamline at the Advanced Photon Source, Argonne National Laboratory (Argonne, IL, USA). Monochromatic data collection was conducted at a wavelength of 0.98 Å using a Quantum 315 CCD detector providing a data set with a resolution to 2.4 Å.

Figure 23. Crystals of *Ct*NHase. Crystallization by the hanging-drop vapor diffusion method in 1.08 M K_2HPO_4, 0.49 M NaH_2PO_4, with 25 or 30% glycerol at 20 °C.

Structure determination and refinement. The X-ray data set for *Ct*NHase was indexed, integrated and scaled using HKL3000 software and the statistics revealed that the data were of good quality (Table 3) (108). The space group was $P3_1$ with eight copies of *Ct*NHase heterodimers in each asymmetric unit giving a solvent content of 71%. Molecular replacement was carried out with a known NHase structural model (PDB ID: 1AHJ) (42) using the program Phaser from the CCP4 software suite. Once a solution was

obtained, model building was conducted in COOT (110); rigid-body refinement and restrained refinement was conducted in refmac5 (109). In order to remove model bias and achieve the best refinement result possible, simulated annealing refinement, TLS refinement, and ordered solvent identification were conducted using PHENIX.refine (111) while model building continued until the lowest R_{free}/R values were achieved. Active site metal ion occupancies were initially set at one resulting in negative difference electron density (F_o-F_c map) around the metal center (not shown). Metal analyses indicated ~0.8 equivalents of iron per heterodimer, therefore, the final structural model was refined with iron ion occupancies and those of the three coordinating residues (CSA102, S103 and CSA104) set at 0.8. Positive difference electron density (F_o-F_c map) around this region was observed (not shown) after refinement, which is likely due to the contribution of residues 102-104 from the 20% apo-enzyme molecules in the crystal. The structure was refined in PHENIX with the completed model possessing R_{free}/R values of 22.7/18.8. Since the $P3_1$ space group can be indicative of twining, the L-test for twining was conducted using the Xtriage program in PHENIX revealing that the intensity statistics behave as expected, indicating no twining.

Table 3. Data Collection and Refinement Statistics for the *Ct*NHase Crystal Structure.

PDB Code	4FM4
Resolution Range, Å	36.2-2.4
Space Group	$P3_1$
Cell Dimensions	
a, b, c, Å	111.4, 111.4, 475.3
α, β, γ, °	90, 90, 120
Total (Unique) Reflections	128,0741 (262,123)
Completeness, %	99.5 (99.2)
Linear R_{merge}[a], %	13.3 (60.2)
I/σ ($I/\sigma_{cut-off}$)	11.0 (1.0)
R_{crys}[b]/R_{free}[c], %	18.8/22.7
Rmsd[d] bond, Å	0.01
Rmsd[d] angle, °	1.4
Average B, $Å^2$	47.8
Estimated Coordinates Error, Å	0.29

[a]Linear $R_{merge} = \Sigma|I_{obs}-I_{avg}|/ \Sigma I_{avg}$

[b]$R_{crys} = \Sigma|F_{obs}-F_{calc}|/ \Sigma F_{obs}$.

[c]Five percent of the reflection data were selected at random as a test set and only these data were used to calculate R_{free}.

[d]rmsd, root mean square deviation.

CHAPTER FOUR

MUTATIONAL, STRUCTURAL, AND KINETIC ANALYSES ON αHIS80, αHIS81, AND αARG157 RESIDUES: INSIGHT INTO THE NITRILE HYDRATASE MECHANISM

Research Aim

The Fe-type NHase from *Comamonas testosteroni* Ni1 (*Ct*NHase) is unusual among NHases in that it is able to incorporate iron into its active site and properly oxidize the equatorial cysteine ligands to Cys^{104}-SOH and Cys^{102}-SO_2H in the absence of an activator protein (118). The X-ray crystal structure of *Ct*NHase is similar to other Fe-type NHases that have been structurally characterized (Figure 21A) (42-44). However, the active site ligand, Cys^{104}-SOH, was found to be fully oxidized to Cys^{104}-SO_2H (Figure 21B) since crystals of *Ct*NHase were obtained under aerobic conditions over the course of a week and in the absence of the weak NHase inhibitor, butyric acid, which slows the oxidation process. Analysis of its X-ray crystal structure revealed that two α-subunit histidine residues, αHis80 and αHis81, and an arginine residue, αArg157, coordinate to a phosphate ion from the crystallization solution (Figure 21B).

Interestingly, these histidine residues are non-conserved among the Fe- and Co-type NHases (Figure 24) while αArg157 is strictly conserved among both types of NHases (Figure 24). Both of these histidine residues are located near the active site and

Figure 24. Alignment of the amino acid sequences of the α-subunits of Fe- and Co-NHases. The conserved metal-binding and the arginine residue which hydrogen bonds to the active site cysteine-sulfenic acid are highlighted in black. The two non-conserved histidine residues (His80 and His 81) found in *Ct*NHase are highlighted in gray. Ct, *Comamonas testosteroni* Ni1; Re-TG3282, *Rhodococcus equi* TG328-2 (Fe-type); Rh-R312, *Rhodococcus* sp. 312 (Fe-type); Rh-N771, *Rhodococcus* sp. N771 (Fe-type); Pt, *Pseudonocardia thermophila* JCM 3095 (Co-type); Rh/HM-J1, *Rhodococcus rhodochrous* J1 high-molecular-mass (Co-type).

contribute to an unusual solvent accessible cavity above the active site, while the conserved arginine residue forms hydrogen bonds to Cys^{104}-SO_2H (Figure 21B). Recently, it was shown that Cys-SOH functions as a nucleophile in the hydration of the nitrile substrate (119). Additionally, mass-spectrometry studies on the oxidation states of the post-translationally modified active site Cys residues reveal the importance of Cys-SOH in the catalytic activity of NHase (46). In an effort to understand the catalytic roles that αHis80, αHis81, and αR157 play, we have mutated these residues to αH80A, αH81A, αH80A /αH81A, αH80W/αH81W, αR157A, and αR157K, and examined the resulting *Ct*NHase enzymes kinetic properties, metal content, UV-Visible spectra, and structural properties *via* X-ray crystallography.

Kinetic Analysis of *Ct*NHase Mutant Enzymes

Kinetic constants of wild-type and mutant *Ct*NHases were obtained by monitoring the hydration of acrylonitrile to acrylamide using a continuous UV-Visible assay at 25 °C in 50 mM Tris-HCl pH 7.5 providing a K_m value of 248 ± 20 mM and a k_{cat} of 1100 ± 30 s^{-1}. Interestingly, the k_{cat} value obtained is ~15-fold higher than the previously reported while the K_m is ~1.4-fold lower (118). In the present study, the assay was performed immediately after the enzyme was purified (both purification and kinetic measurements were performed in a time-window of ~12 h) as *Ct*NHase loses catalytic activity over time. Such a decrease in catalytic activity over time has been reported for both Co- and Fe-type NHases and likely results from the oxidation of the Cys-SOH ligand to Cys-SO_2H when stored under aerobic conditions and in the absence of butyric acid (46,103).

A purification procedure similar to the wild-type enzyme was used for all of the mutants and kinetic analyses were performed immediately after purified enzyme was

obtained, which was within a time-window of ~12 h. Single point-mutations of the histidine residues to alanines (αH80A and αH81A) resulted in an enzyme with an ~25% decrease in K_m and an ~80% (αH80A) and ~93% (αH81A) decrease in k_{cat} (Table 4). The double alanine mutant (αH80A/αH81A) provided an enzyme with an ~15% decrease in K_m and an ~88% decrease in k_{cat} (Table 4), mimicking the kinetic constants observed for the αH81A single mutant. Therefore, both αH80 and αH81 are important for the hydration of nitriles, likely in providing hydrogen bonds that stabilize the transition state; however they are not required for catalysis. In an attempt to block the channel leading to the active site, a double mutant containing tryptophan (αH80W/αH81W) was prepared. This mutant enzyme exhibited an ~93% decrease in k_{cat} but only an ~7% decrease in K_m (Table 4). These data indicate that access to the active site Fe(III) ion is not perturbed but the lack of the histidine residues decreases the enzymes ability to hydrate acrylonitrile.

The strictly conserved arginine residue (αR157), which forms hydrogen bonds with the active site α-Cys^{104}-SOH ligand, was mutated to alanine (αR157A). This mutant enzyme exhibited a similar K_m value to that of the wild-type *Ct*NHase but displayed <1% of the wild-type k_{cat} value (Table 4). Mutation of αR157 to lysine (αR157K) also had a similar K_m value to wild-type *Ct*NHase but exhibited only <3% of the wild-type k_{cat} (Table 4). Based on the crystal structure of wild-type *Ct*NHase, a hydrogen-bond of 2.9 Å is formed between the N2-atom of αR157 and the O1-atom of the αCys^{104}-SOH ligand, which is proposed to be the nucleophile in catalysis, and has been suggested to exist in its protonated form at pH 7.5 (54). It is likely that the pK_a and stability of the αCys^{104}-SOH ligand is maintained through hydrogen-bond formation with αR157. Therefore, disruption of this hydrogen-bond will affect the stability of αCys^{104}-SOH resulting in the

observed decreased in catalytic activity.

Table 4. Kinetic Constants for the Wild-type and Mutant *Ct*NHases[a].

	k_{cat} (s^{-1})	K_m (mM)
Wild-type	1100 ± 30	250 ± 20
αH80A	220 ± 38	187 ± 18
αH81A	77 ± 13	179 ± 11
αH80A/αH81A	132 ± 3	213 ± 61
αH80W/αH81W	79 ± 4	232 ± 7
αR157A	10 ± 2	204 ± 8
αR157K	32 ± 4	239 ± 1

[a]Acrylonitrile was used as the substrate.

Metal Analysis and UV-Visible Absorption Spectra of *Ct*NHase Mutant Enzymes

The metal content of wild-type *Ct*NHase was found to be 1.4 ± 0.2 equivalents of iron per $(\alpha\beta)_2$ heterotetramer by inductively coupled plasma mass spectrometry (ICP-MS). These data are in line with the previously reported value of 1.6 equivalents of iron per $(\alpha\beta)_2$ heterotetramer (118). ICP-MS analysis of the single point mutations αH80A, αH81A, αR157A, and αR157K revealed that 2.5 ± 0.2, 1.6 ± 0.2, 2.1 ± 0.2, and 1.3 ± 0.1 equivalents of iron is present per $(\alpha\beta)_2$ heterotetramer, respectively. The double mutants αH80A/αH81A and αH80W/αH81W contained 1.5 ± 0.2 and 1.2 ± 0.1 equivalents of iron per $(\alpha\beta)_2$, respectively. These data are also consistent with those reported for other Fe-type NHases, which typically contain between 1.6 to 2.0 iron ions per $(\alpha\beta)_2$ heterotetramer (120,121). These data indicate that mutating the active site residues αHis80, αHis81, and αR157 has little to no effect on the incorporation of iron into the active site.

The UV-Visible spectrum of Fe-type NHases, contains a characteristic S → Fe(III) ligand-to-metal-charge-transfer (LMCT) band at ~700 nm. Because of its intensity, this S → Fe(III) LMCT band is a good reporter for electronic perturbations occurring at the metal center that are the result of primary and/or secondary coordination sphere changes (49). To determine the effect that each mutation has on the electronic structure of the Fe(III) ions in *Ct*NHase, the UV-Visible spectrum for each of the mutants was obtained. Figure 25 shows the UV-Visible spectra and Table 5 contains the λ_{max} and molar absorptivities (ε) values for the S → Fe(III) LMCT band for each mutant enzyme and wild-type *Ct*NHase for comparison purposes. All of the *Ct*NHase mutants exhibited an S → Fe(III) LMCT band; however, for αH80A, αH81A, αR157A, and αR157K this absorption band was red shifted with a corresponding increase in molar absorptivity. On the other hand, the αH80A/αH81A and αH80W/αH81W mutant enzymes exhibited a blue shift along with a similar increase in molar absorptivity. These observed shifts in LMCT band energies are indicative of electronic perturbations occurring at the Fe(III) center.

Bathochromic (red) shifts in this LMCT band are typically observed when (*i*) the pH is increased, (*ii*), upon interaction with the inhibitor butyric acid, (*iii*), changes in hydrogen-bonding at or near the active site or (*iv*) oxidation of αCys-SOH to αCys-SO_2H (49,64,102). On the other hand, hypsochromic (blue) shifts have been observed by the addition of substrate and also upon disruption of the hydrogen-bonding network between βArg56 and Cys^{114}-SOH and βArg56 and Cys^{112}-SO_2H in the Fe-type NHase from *Rhodococcus* sp. N-771 (37,57,104). Shifts in the S → Fe(III) LMCT band in NHases has been attributed to either an increase or decrease in π-back-donation from the axial Cys ligand to the metal center, in response to perturbations at the active site (53,122).

Given that all mutant spectra was collected in the absence of an inhibitor or substrate, the observed shifts are likely the result of disruption of hydrogen-bonds, hydrogen-bond networks, or the oxidation of αCys^{104}-SOH to αCys^{104}-SO_2H. Oxidation of the sulfenic acid is unlikely given that these spectra were all recorded right after purification.

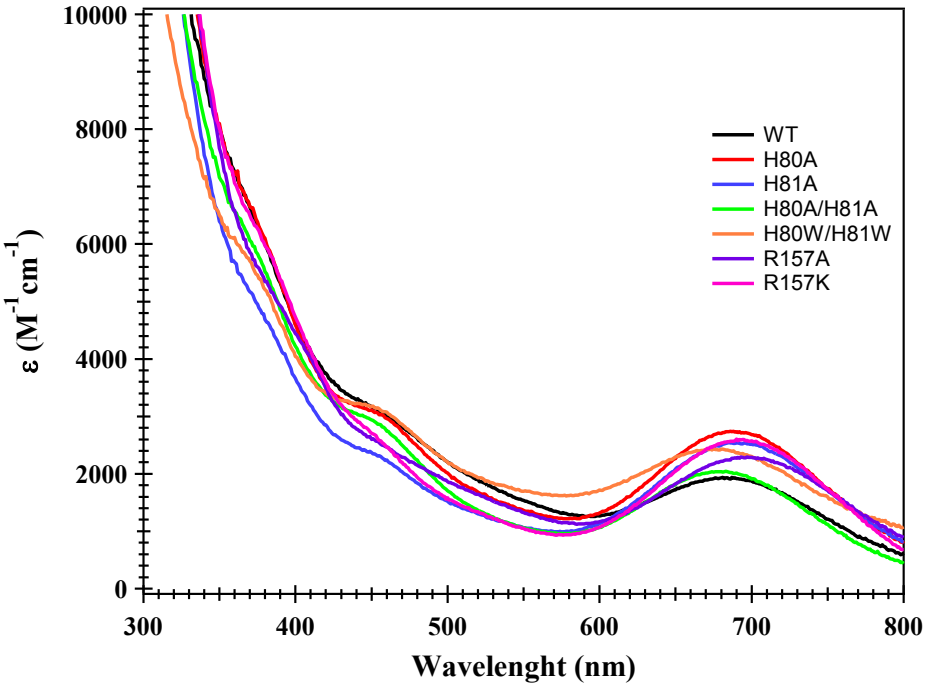

Figure 25. UV-Visible absorption spectra of wild-type and mutant *Ct*NHases. Spectra were recorded in 50 mM Tris-HCl, pH 7.5, and 300 mM NaCl.

Table 5. UV-Visible λ_{max} and Molar Absorptivities (ε) Values for Wild-type and Mutant *Ct*NHases.

	λ_{max} (nm)	ε (M^{-1} cm^{-1})
WT	681	1936
αH80A	686	2743
αH81A	690	2533
αH80A/αH81A	677	2038
αH80W/αH81W	673	2430
αR157A	697	2295
αR157K	691	2576

Analysis of the wild-type active site (Figure 26) shows that a hydrogen-bond exists between the nitrogen atom of the guanidinium moiety of αR157 and the oxygen atom of αCys^{104}-SOH (2.9 Å). This hydrogen-bond is expected to be lost upon mutation of αR157 to an alanine, resulting in a decrease in negative charge on the sulfenic acid oxygen as this oxygen has been shown to protonated at pH 7.5. This would result in an increase in electron donation to the Fe(III) center from the sulfenic acid sulfur ligand. Red shifts of similar magnitude observed in NHase enzymes were attributed to a decrease in π-electron donation from the axial thiolate ligand to the Fe(III) ion to compensate for the π-donating behavior of the sulfenic acid ligand (49,64,102). In contrast, the αR157K enzyme could still participate in hydrogen-bonding with α-Cys^{104}-SOH, albeit less efficiently, thus the observed red shift is smaller in magnitude. While no direct hydrogen-bond is observed between αH80 or αH81 and the active site ligands, they do form hydrogen bonds with solvent molecules that in turn interact with active site ligands. Therefore, the observed red or blue shift for the αHis single and double point mutants is likely due to disruption of this hydrogen-bonding network, which in turn perturbs the electronic state of the Fe(III) center affecting its ability to catalyze the hydration of nitriles.

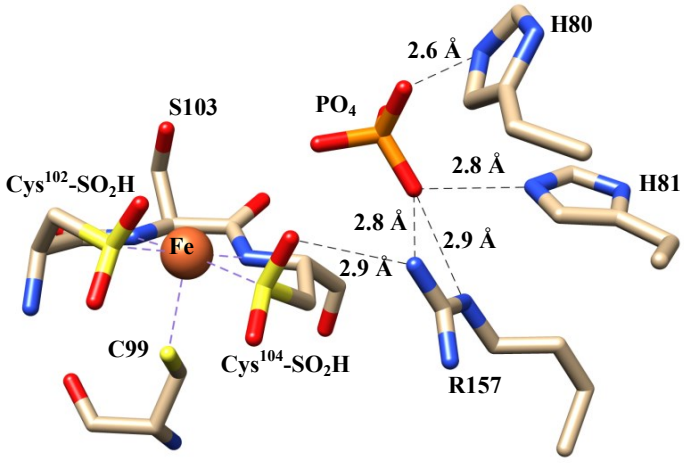

Figure 26. Hydrogen-bonding network near the active site of wild-type *Ct*NHase (PDB ID: 4FM4). The black dashed lines represent the hydrogen bonds.

Crystal Structures of *Ct*NHase Mutants

The X-ray crystal structures of the *Ct*NHase αH80A/αH81A, αH80W/αH81W, and αR157A mutants were solved to 2.0, 2.8, and 2.5 Å resolutions, respectively. Overall, the X-ray crystal structures of all three mutant *Ct*NHase enzymes are similar to the wild-type structure (Figure 27A) with the α-carbon root mean squared deviation (rsmd) for the α-subunit within 0.567 Å (αH80A/αH81A), 0.546 Å (αH80W/αH81W), and 0.225 Å (αR157A) while the rsmd for the β-subunit is within 0.232 Å (αH80A/αH81A), 0.193 Å (αH80W/αH81W), and 0.171 Å (αR157A). Three distinct differences are observed among the α-subunits of all of the mutant enzymes, including the orientation of the C-terminal (Figure 27A) and two loop regions containing α74-82 and α152-155 (Figure 27B, Table 6), which are in the vicinity of the metal center and near the mutation sites. A loop region in the β-subunit containing residues β92-98 is also slightly perturbed (Figure 27A). Shifting the α74-82 loop (Figure 27B, Table 6) in the mutant enzymes contributes to a much wider channel leading to the active site allowing

greater solvent and substrate access while likely decreasing substrate specificity as evidenced from K_m values, which are related to substrate affinity. In addition, a significant change in the orientation of two lysine residues located on this loop, αK79 and αK82, is also observed in the αH80A/αH81A and αH80W/αH81W strucutres. In both structures, the side chains of the two lysine residues change conformation as they flip and point away from the channel compared to the wild-type structure. Such a change in conformation, likely results in the loss in these residues ability to participate in hydrogen-bonding networks with solvent, substrate and/or product. Similar, perturbations in the hydrogen-bonding networks around the active sites of both Fe- and Co-type NHases have been reported when, for example, second- or third-shell residues in either the α- or β-subunit have been mutated, yielding enzymes with low catalytic activities (64,123).

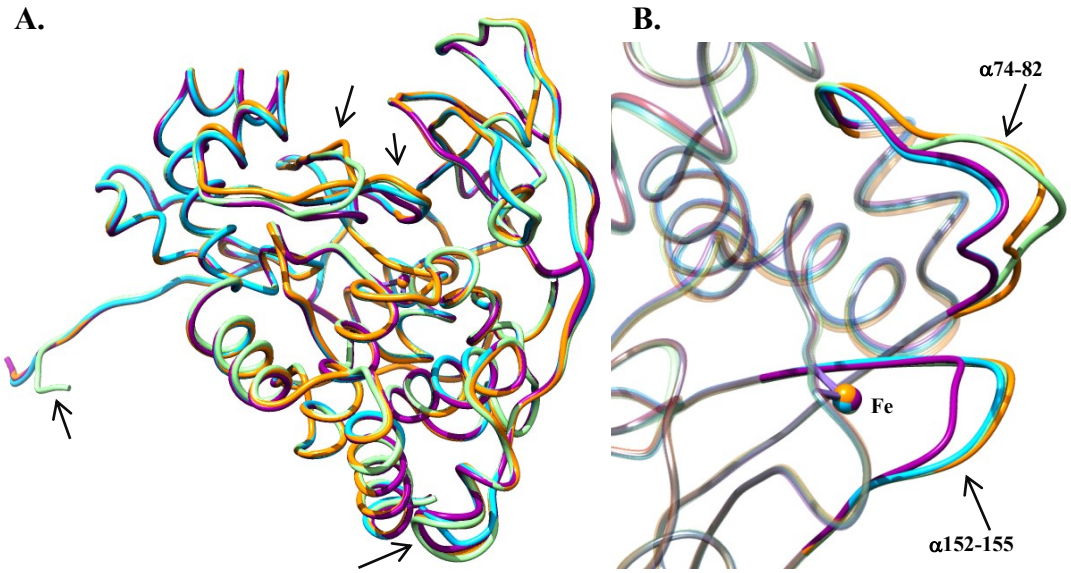

Figure 27. Superposition of wild-type *Ct*NHase (PDB ID: 4FM4) and mutant structures. **A)** Superposition of the αβ heterodimer, the wild-type is in dark magenta, αH80A/αH81A mutant is in light green, αH80W/αH81W is in orange, and the αR157A mutant is in light blue. The regions with pronounced difference between the wild-type and the mutant enzymes are indicated with arrows. **B)** The two loop regions located in the α-subunit exhibiting relatively significant structural differences are indicated by arrows.

Table 6. Summary of the Root Mean Squared Standard Deviation (RMSD) Values for the Mutants vs. Wild-type *Ct*NHase Crystal Structures.[a]

	αSubunit (Å)	**Loop α74-82 (Å)**	**Loop α152-155 (Å)**
αH80A/αH81A	0.567	2.232	0.925
αH80W/αH81W	0.546	2.127	0.909
αR157A	0.225	0.320	0.837

[a]Structural Comparison was done in UCSF Chimera

Structures of αH80A/αH81A and αH80W/αH81W. In contrast to the wild-type *Ct*NHase structure (Figure 26) and αH80W/αH81W (Figure 28) enzyme, the Fe(III) ion in the αH80A/αH81A mutant enzyme (Figure 29) is six coordinate. It is bound by three sulfurs from αC99, αC102, and αC104, two backbone amide nitrogens, and an oxygen atom from a water molecule. Similar to the wild-type enzyme, the equatorial αC102 and αC104 ligands are fully oxidized to αCys-SO_2H for both αH80A/αH81A and

αH80W/αH81W since the crystals were obtained under aerobic conditions over the course of a week. The phosphate ion, originally present in the active site of the wild-type *Ct*NHase enzyme is absent in both structures. In the active site of the wild-type enzyme (Figure 26), an hydrogen-bond is formed between the N2-atom of αR157 and the O1-atom of αCys^{104}-SO_2H (2.9 Å); however, in the αH80/αH81 mutant, this distance increases to 3.7 Å (Figure 29) while in the αH80W/αH81W enzyme it increases to 4.1 Å (Figure 28), both of which are outside a typical hydrogen-bond distance. Although αR157 in both the αH80/αH81 and αH80W/αH81W mutant enzymes is still capable of forming a hydrogen-bond with the O1 oxygen atom of αCys^{104}-SO_2H, substitution of αH80 and αH81 for alanine or tryptophan residues disrupts loops α74-82 (Figure 27B, Table 6) and α152-155 (Figure 27B, Table 6) resulting in αR157 being pulled away from αCys^{104}-SO_2H, preventing hydrogen-bond formation. Based on sulfur K-edge EXAFS and geometry-optimized DFT calculations, the protonation state of the sulfenic acid was suggested to be Cys-SOH (54). Therefore, the loss of this hydrogen-bonding interaction between αR157 and the O1-atom of the sulfenic acid ligand will likely decrease the nucleophilicity of the sulfenic oxygen atom, consistent with the observed blue-shift in the S → Fe(III) LMCT band. Since the sulfenic acid ligand has been shown to function as the nucleophile in the catalytic reaction, the loss of the hydrogen bond between the αR157 and the O1-atom of the sulfenic acid ligand would be expected to significantly decrease the activity. Therefore, the 10-fold decrease in k_{cat} observed for both αH80A/αH81A and αH80W/αH81W mutant enzymes is consitent with these crystallographic data.

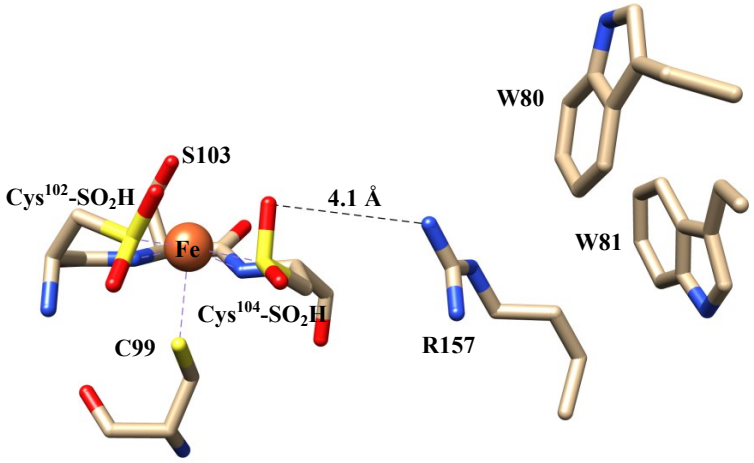

Figure 28. Active site of the αH80W/αH81W mutant *Ct*NHase. The black dashed line represents the hydrogen bond.

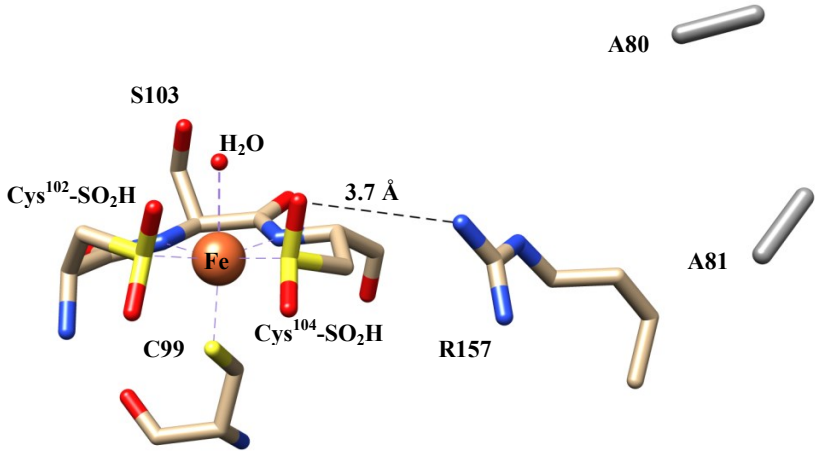

Figure 29. Active site of the αH80A/αH81A mutant *Ct*NHase. The black dashed line represents the hydrogen bond.

Table 7. Distances (Å) between the Iron Center and the Atoms from the Ligands in the Wild-type and Mutant Crystal Structures.

	Fe-S (αCys99)	**Fe-S (αCys^{102}-SO$_2$H)**	**Fe-S (αCys^{104}-SO$_2$H)**	**Fe-N (αSer103)**	**Fe-N (αCys^{104}-SO$_2$H)**
Wild-type	2.5	2.1	2.4	2.2	2.2
αH80A/αH81A	2.2	2.2	2.1	2.2	2.1
αH80W/αH81W	2.5	2.1	2.3	2.2	2.3
αR157A	2.4	2.2	2.2	2.0	2.2

The decrease in nucleophilicity of the sulfenic oxygen atom is also reflected in the decreased distance between the S-atom of αCys^{104}-SO_2H and the Fe(III) ion (2.4 Å in wild-type vs. 2.1 Å for αH80A/αH81A and 2.3 Å for αH80W/αH81W) (Table 7). The decreased bond distance suggests increased electron donation to the metal center resulting in decreased electron density on the oxygen-atom of the sulfenic acid moiety. Decreased Lewis acidity of the Fe(III) ion in the histidine mutated enzymes is also reflected in the shorter S-atom bond distance of the trans αC99 ligand (2.5 Å in wild-type vs. 2.2 Å for αH80A/αH81A). Since the thiol ligands tune the Lewis acidity of the metal center, the correct push or pull of electron density to and from the metal center, especially for αC99 which is trans to the exchangeable sixth coordination site where the water/OH^-/product/substrate bind, is critical for full catalytic activity (49,53,124). These data are also constant with the observed blue shift in the S → Fe(III) LMCT band and indicate that the loss of the hydrogen-bonding interaction between αR157 and the O1-atom of the sulfenic acid ligand alters the catalytic properties of the active site Fe(III) ion.

Structure of αR157A. The Fe(III) active site of the αR157A mutant enzyme is five coordinate, bound by three sulfurs from αC99 and the post-translationally modified αC102 and αC104 residues, as well as two backbone amide nitrogens (Figure 30). Similar to the wild-type and αH80W/αH81W enzymes, the sixth site is unoccupied. Interestingly, besides the loss of the hydrogen-bond between the N2-atom of αR157 and the O1-atom of αCys^{104}-SO_2H (Figure 30), the αR157A enzyme has the least structural change in the overall α-subunit (rmsd of 0.225) and the α74-82 loop region (rmsd of 0.320). Similar to the histidine mutant enzymes, the Fe(III)-ligand bond distances for the αR157A mutant enzyme decrease (Table 7) except for the S-atom of the αCys^{102}-SO_2H

ligand, which increases from 2.1 to 2.2 Å. These data suggest that the >100-fold decrease in the catalytic activity is due to the loss of the hydrogen-bond between αR157 and αCys^{104}-SOH ligand, which has been suggested to function as the nucleophile in the catalytic reaction (119). That hydrogen-bond formation to the actives site Cys ligands is catalytically important is also reflected in recent studies on both Fe- and Co-type NHases. For example, mutation of αR56 in the Fe-type NHase from *Rhodococcus erythropolis* N771, which forms a hydrogen bond to both the sulfenic acid and sulfinic acid residues, resulted in an enzyme that exhibits only 1% of the catalytic activity of the wild-type NHase (47,123). Similarly, mutation of αR170 in the Co-type NHase from *Pseudomonas putida*, which corresponds to the mutated αR157 in *Ct*NHase, to an aspartate resulted in an enzyme with a 1.6-fold decrease in the catalytic efficiency (47,123). These data underscore the importance of hydrogen-bond formation between second sphere residues and the active site sulfinic and sulfenic acid ligands in NHases.

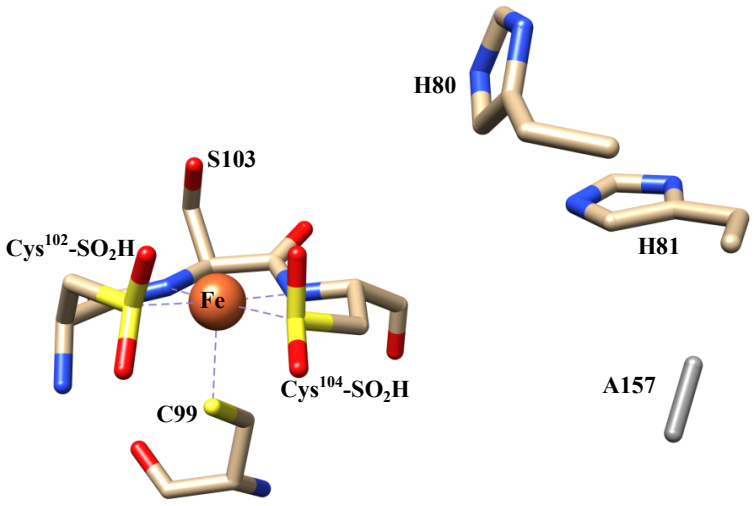

Figure 30. Active site of the αR157A mutant *Ct*NHase.

Summary

Based on these data, mutation of αH80, αH81, and αR157 result in *Ct*NHase enzymes with diminished catalytic activity, indicating that all three residues are catalytically important but not essential. In each mutant enzyme, hydrogen-bonding interactions are crucial for the catalytic function of the αCys^{104}-SOH ligand. Eliminating these hydrogen bonding interactions likely alters the nucleophilicity of the sulfenic acid oxygen and the Lewis acidity of the active site Fe(III) ion. Several studies on both Fe- and Co-type NHases have shown the importance of the stability and integrity of the Cys-SOH ligand for catalytic activity in NHases; for example, further oxidation to Cys-SO_2H leads to inactivation (46,102). Most recently, in our studies with the Co-type NHase from *P. thermophila* JCM 3095, we showed that Cys-SOH can function as a nucleophile in the hydration of nitrile to amides by NHase (119). Therefore stabilization of αCys^{104}-SOH in *Ct*NHase through hydrogen-bond formation with αR157 is important for a fully functional NHase enzyme. Second, although not directly involved in catalysis, the two non-conserved αH80 and αH81 residues appear to play an important role in maintaining the proper structure of the α-subunit in and around the active site. For example, the αH80A/αH81A and αH80W/αH81W mutant enzymes exhibited two significant structural changes in two loop regions of the α-subunit (α74-82 and α152-155) that affected the metal-ligand bond distances and the hydrogen-bonding interaction between αR157 and αCys^{104}-SOH. Therefore, these studies indicate that a combination of elements that include the proper structure of the active site (*i.e.* stabilization of active site nucleophile through hydrogen-bonding and proper distance of the ligands to metal center), proper architecture of the α-subunit, and outer-sphere residues (e.g. αHis80 and αHis81), are

necessary for NHase to efficiently catalyze nitrile to amides.

Experimental Procedures

Materials. Acrylonitrile was obtained from Sigma-Aldrich. All other materials were purchased at the highest quality available.

Mutagenesis of CtNHase. Site-directed mutagenesis was performed using the QuickChange Lightning Multi Site-Directed Mutagenesis Kit from Agilent following the manufacturer's instructions. The expression plasmid pSMCtαβHis containing the α and β-His_6 genes of *Ct*NHase was used as the template for mutagenesis and the primes used for the mutagenesis are listed on Table 7. The mutations were confirmed by DNA sequencing at the University of Chicago Cancer Research Center DNA sequencing facility. Mutant plasmids were transformed into *Escherichia coli* BL21(DE3) competent cells (Agilent) for expression.

Table 8. Primers for *Ct*NHase Site-Directed Mutagenesis.[a]

Mutation	Primers
αH80A	F: CTGGGGTTCAGTTTCCCAAAG**GCC**CATAAACACTTTGTTG R: CAACAAAGTGTTTATG**GGC**CTTTGGGAAACTGAACCCCAG
αH81A	F: GGTTCAGTTTCCCAAAGCAC**GCT**AAACACTTTGTTGTACTCG R: CGAGTACAACAAAGTGTTT**AGC**GTGCTTTGGGAAACTGAACC
αH80A/ αH81A	F: GTTCAGTTT CCCAAAG**GCCGCT**AAACACTTTGTTGTAC R: GTACAACAAAGTGTTT**AGCGGC**CTTTGGGAAACTGAAC
αH80W/ αH81W	F: GGGTTCAGTTTCCCAAAG**TGGTGG**AAACACTTTGTTGTACTCG R: CGAGTACAAAGTGTTT**CCACCA**CTTTGGGAAACTGAACCCC
αR157A	F: GGATACGACTGCCGATACT**GCA**TATATGGTCTTGCCGCTT R: AAGCGGCAAGACCATATA**TGC**AGTATCGGCAGTCGTATCC
αR157K	F: TACGACTGCCGATACT**AAA**TATATGGTCTTGCCGC R: GCGGCAAGACCATATA**TTT**AGTATCGGCAGTCGTA

[a]Mutated codons are in bold. Primers are written from 5' to 3'. F, forward primer; R, reverse primer.

Expression and purification of CtNHase mutants. The mutant proteins were expressed and purified and characterized as described on Chapter 3 *Experimental Procedures* section for the wild-type *Ct*NHase. Purified protein samples were analyzed by 12.5 % SDS-PAGE. Protein concentration was determined using a Coomassie (Bradford) Protein Assay Kit (Thermo Scientific). Theoretical molecular weights and protein extinction coefficients were calculated with the ExPASy compute pI/Mw tool (107). The molecular weight for the *Ct*NHase heterotetramer was 92,828 g/mol with an extinction coefficient of 118,720 cm^{-1} M^{-1}.

Kinetic Assay of CtNHase mutants. The activity of wild-type and mutant proteins were determined by following the hydration of acrylonitrile in 50 mM Tris-HCl pH 7.5 spectrophotometrically at 225 nm ($\Delta\varepsilon_{225}$ = 2.9 mM^{-1} cm^{-1}). All assays were performed at 25 °C in a Shimadzu UV-2450 PC spectrophotometer in 1 mL quartz cuvette with different concentrations of substrate as soon as the protein was purified. The reaction was started with enzyme. One unit (U) of NHase activity is defined as the formation of 1 μmol of acrylamide per minute. To obtain the kinetic parameters, V_{max} and K_m, the initial velocities from at least two independent measurements were fitted to the Hill equation by non-linear regression using OriginPro 9.0 (OriginLab, Northampton, MA).

UV-Visible spectroscopy of CtNHase wild-type and mutants. UV-Vis absorption spectra were recorded on Shimadzu UV-2450 PC spectrophotometer in 1 mL quartz cuvette in 50 mM Tris-HCl, pH 7.5, and 300 mM NaCl at 10 °C.

Metal Analysis of CtNHase mutants. The metal content of mutant protein was determined by inductively-coupled plasma mass spectrometry (ICP-MS). Purified wild-type and mutant proteins along with a control of buffer containing no protein were

digested with concentrated nitric acid (0.863 mL) and heated at 70 °C for 1 h. The samples were allowed to cool to room temperature then diluted to final concentration of 5% nitric acid. The metal content was analyzed at the Water Quality Center in the College of Engineering at Marquette University.

Crystallization of Mutant Proteins. Crystals of *Ct*NHase were obtained by the hanging drop vapor diffusion method using the same conditions as those described in Chapter 3 *Experimental Procedur*es section for the wild-type *Ct*NHase. For X-ray data collection, the crystals were soaked in the reservoir solution with 30% (v/v) glycerol as a cryo-protectant before flash freezing in liquid nitrogen. The X-ray data set (Table 9) for *Ct*NHase mutants was indexed, integrated and as described in Chapter 3 *Experimental Procedur*es section for the wild-type *Ct*NHase. Molecular replacement was carried out with the wild-type *Ct*NHase structural model.

Table 9. Data Collection and Refinement Statistics for the *Ct*NHase Mutant Crystal Structures

Data set	***Ct*NHase αH80A/αH81A**	***Ct*NHase αH80W/αH81W**	***Ct*NHase αR157A**
Space Group	P31	P31	P31
Cell Dimensions			
a=b (Å)	112.0	111.7	111.6
c (Å)	476.0	475.9	474.6
α=β (°)	90	90	90
γ (°)	120	120	120
Resolution (A)	36.57-2.00	67.84-2.80	50.60-2.25
[a]R_{merge} (%)	14.8(69.9)	14.5(72.4)	15.6(72.4)
I/sigma	3.2(2.2)	7.3(1.9)	6.9(2.1)
Completeness (%)	99.7(99.2)	99.9(100)	100(100)
Redundancy	5.6(5.5)	3.6(3.7)	3.8(3.7)
No. Total reflections	2508285	585059	1185275
No. Unique reflections	450084	163400	313740
[b]R_{work} / [c]R_{free} (%)	25.0/21.1	22.9/18.1	20.3/17.3
No. of Atoms	30101	26101	28551
No. of Solvent Atoms	4561	445	2995
B-factors (Å^2)	30.3	48.4	31.8
[d]RMSD Bond Length (A)	0.08	0.08	0.07
[d]RMSD Bond Angles (°)	1.06	1.16	1.07
Ramachandran			
Favored (%)	96.4	94.9	96.7
Allowed (%)	2.6	3.8	2.5
Outlier (%)	1.0	1.3	0.8

The values for the highest resolution bin are in parentheses.
[a]Linear $R_{merge} = \Sigma|I_{obs}-I_{avg}|/ \Sigma I_{avg}$
[b]Rcryst = $\Sigma|F_{obs}-F_{calc}|/ \Sigma F_{obs}$
[c]Five percent of the reflection data were selected at random as a test set and only these data were used to calculate R_{free}.
[d]RMSD, root mean square deviation.
ND, Not Determined/Calculated by the program

CHAPTER FIVE

BIOCHEMICAL CHARACTERIZATION OF A EUKARYOTIC NITRILE HYDRATASE

Research Aim

Nitrile hydratases have been primarily isolated from bacterial (prokaryotic) organisms but recently, bioinformatics investigations have provided evidence for the potential emergence of a novel class of nitrile hydratase in unicellular eukaryotic organisms such as *Monosiga brevicollis, Thecamonas trahens, Sphaeroforma arctica, Stephanoeca diplocostata*, *Salpingoeca rosetta, Emiliania huxleyi* and *Aureococcus anophagefferens* (20,21). Unlike prokaryotic NHases, the purported eukaryotic NHase open reading frame (ORF) contains fused α and β subunits bridged by an insert made up of several histidines residues (Figure 31). The C-terminus of the eukaryotic protein contains the strictly conserved metal-binding motif (CTLCSCY) found in the α subunit of Co-type NHases and the homologous cobalt thiocyanate hydrolase (10). Interestingly, the number of histidine residues linking the two subunits varies by organism, for example the *Monosiga brevicollis* gene encodes for seventeen histidines, while the gene from *Salpingoeca rosetta* encodes for only two histidines. In addition, the size of this insert also varies by eukaryotic organism.

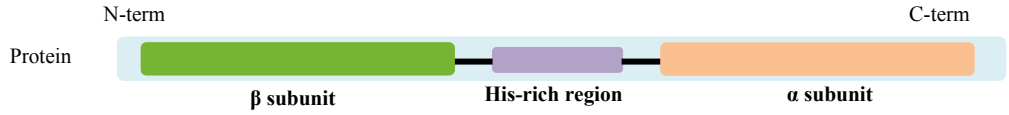

Figure 31. Scheme showing the arrangement of the fused NHase β and α subunits in eukaryotes (figure adapted from reference 21).

The aim of this research is to clone and purify a purported eukaryotic NHase and determine if this enzyme possesses NHase activity. To accomplish this aim, the gene encoding the choanoflagellate *Monosiga brevicollis* NHase (*Mb*NHase) was cloned and expressed in *Escherichia coli*. This gene product was then characterized by biochemical and kinetic analyses.

Cloning, Expression, and Purification of *Mb*NHase

The existence of a eukaryotic NHase in the choanoflagellate *M. brevicollis* and other eukaryotic organism was reported (20,21); however, until now no biochemical characterization of this novel NHase has been described. The gene encoded by *M. brevicollis* contains 495 amino acids and alignment of this gene with the amino acids of the α and β subunits from various prokaryotic NHases revealed that the N-terminus of *Mb*NHase aligns with the β subunit of the NHases (Figure 32), while the C-terminus aligns with and has high similarity (35-45%) to the α subunits (Figure 33). Both α and β subunits in *Mb*NHase are connected by a histidine rich region containing seventeen histidines, and the C-terminus contains the signature Co-type NHase metal-binding domain (Figure 33). The gene was commercially synthesized using *E. coli* codon usage and cloned into the pET21a^{+} vector, subsequently, the plasmid was transformed into *E. coli* BL21(DE3) cells for protein expression. Similar, to the growth and expression

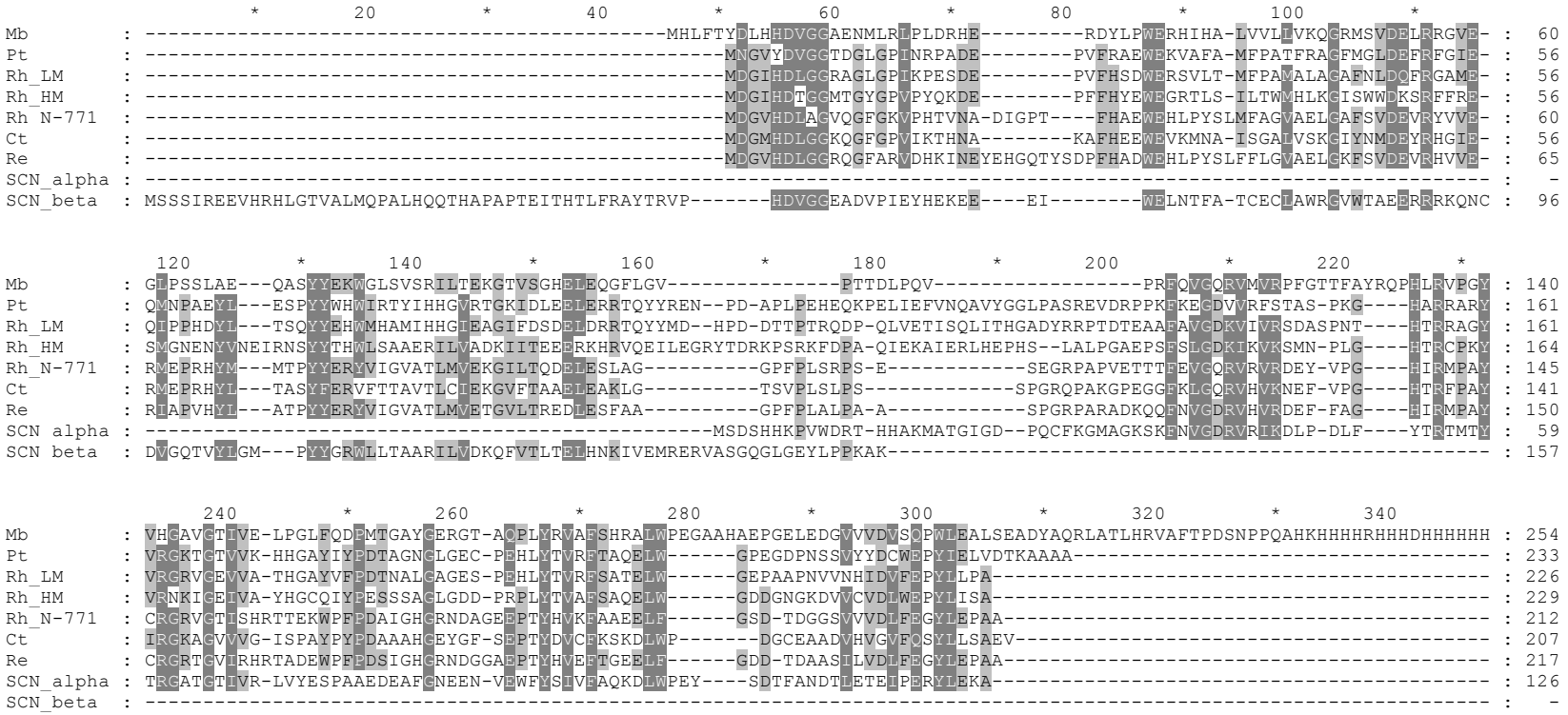

Figure 32. Amino acid alignment of the N-terminus residues of the eukaryotic NHase from *M. brevicollis* and prokaryotic NHase β subunits. Conserved residues among *Mb*NHase and prokaryotic NHases are highlighted in gray. Mb, NHase from *M. brevicollis*; Co-NHases: Pt (*Pseudonocardia thermophila* JCM 3095), Rh_LM, (low-molecular weight, *Rhodococcus rhodochrous* J1), Rh_HM (high-molecular weight, *Rhodococcus rhodochrous* J1); Iron-NHases: Rh_N-771 (*Rhodococcus* sp. N-771), Ct (*Comamonas testosteroni* Ni1), Re (*Rhodococcus equi* TG328-2); SCN_alpha, SCN_beta, and SCN_gamma, cobat thiocyanate hydrolase (SCNase) from *Thiobacillus thioparus* THI115.

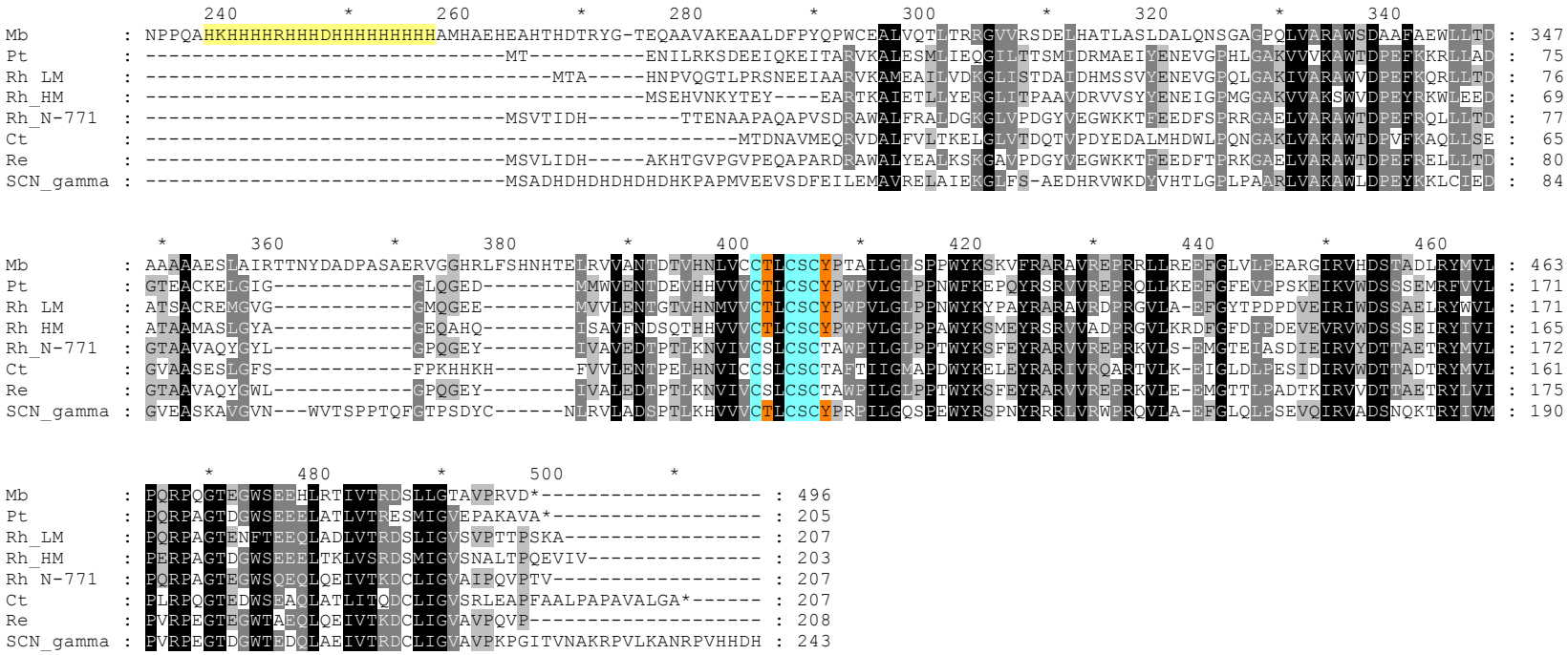

Figure 33. Amino acid alignment of the C-terminus residues of the eukaryotic NHase from *M. brevicollis* and prokaryotic NHase α subunits. Conserved residues among *Mb*NHase and prokaryotic NHases are highlighted in black and gray. The metal-binding motif is highlighted in cyan and active site Co-type NHase residues are in orange. The histidine-rich region is highlighted in light yellow. Mb, NHase from *M. brevicollis*; Co-NHases: Pt (*Pseudonocardia thermophila* JCM 3095), Rh_LM, (low-molecular weight, *Rhodococcus rhodochrous* J1), Rh_HM (high-molecular weight, *Rhodococcus rhodochrous* J1); Iron-NHases: Rh_N-771 (*Rhodococcus* sp. N-771), Ct (*Comamonas testosteroni* Ni1), Re (*Rhodococcus equi* TG328-2); SCN_alpha, SCN_beta, and SCN_gamma, cobat thiocyanate hydrolase (SCNase) from *Thiobacillus thioparus* THI115.

conditions of other Co-type NHases (27,28,57), the growth media was supplemented with $CoCl_2$ (0.25 mM).

Taking advantage of the seventeen histidine residues naturally encoded by the gene, the protein was purified by IMAC. The purified protein exhibits an amber color (Figure 34A) and SDS-PAGE (Figure 34B) showed a single band, with molecular weight of ~50 kDa, which is in good agreement with the theoretical molecular weight of 55.6 kDa. In contrast, to prokaryotic NHases, this eukaryotic NHase was expressed as a fused protein where both the α and β subunits reside in a single polypeptide (Figure 34B), as predicted by Foerstner and colleagues (21). The quaternary structure of the purified protein was analyzed by gel filtration chromatography. Comparison of the elution profile to those of protein standards used to calibrate the column along with the cobalt NHase from *Pseudonocardia thermophila* JCM 3095 (*Pt*NHase), revealed that *Mb*NHase exists primarily as a homodimer in solution with a small fraction (<10%) existing as a monomer. These data indicate that in solution, *Mb*NHase resembles the general quaternary structure, $\alpha_2\beta_2$ heterotetramer, found in both Co- and Fe-type NHases (44,125).

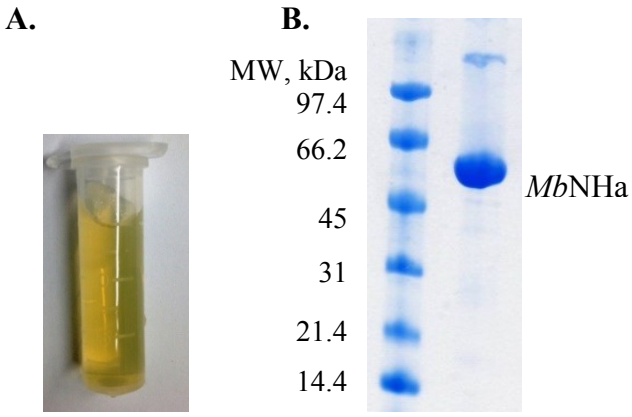

Figure 34. Analysis of purified *Mb*NHase. **A)** Purified *Mb*NHase and **B)** SDS-PAGE analysis: *lane 1* molecular weight standards, *lane 2* purified *Mb*NHase.

*Mb*NHase Is Catalytically Active towards Nitrile Substrates

The ability of the purported recombinant eukaryotic NHase to hydrate nitrile compounds to the corresponding amide was investigated using a continuous UV-Visible spectrophotometric assay (57,118,119). Because the natural substrate of this purported NHase enzyme is unknown, substrates typically used for analyzing the activity of well characterized NHases were chosen as potential substrates to determine the catalytic activity; these included, one aliphatic nitrile substrate (acrylonitrile), one aromatic nitrile (benzonitrile), and a thiocyanate (2-nitro-5-thiocyanatobenzoic acid (NTCB)). Table 10 summarizes the kinetic constants for each of these nitrile and thiocyanate substrates for *Mb*NHase. The purported *Mb*NHase is, in fact, capable of hydrating both acrylonitrile (k_{cat} = 99 ± 8 s^{-1}) and benzonitrile (k_{cat} = 18.3 ± 0.5 s^{-1}) as well as the thiocyanate substrate NTCB (k_{cat} = 0.017 ± 0.003 s^{-1}) following Michaelis-Menten kinetics. Interestingly, the enzyme had a higher affinity for the aromatic nitrile substrate compared to the aliphatic substrate (Table 10), following the trend observed for most Co-type NHases, which tend to have a preference for aromatic nitriles (2,10). These data

establish that the purported recombinant *Mb*NHase possesses NHase activity. These data also suggests that the two active site cysteine residues, Cys^{403} and Cys^{405}, are properly oxidized to cysteine sulfinic acid (Cys^{403}-SO_2H) and cysteine sulfenic acid (Cys^{405}-SOH) because proper oxidation of these two active site residues is necessary for NHase enzymes to be catalytically activity (46).

Table 10. Kinetic Parameters of the Eukaryotic *Mb*NHase.

Substrate	K_m **(mM)**	k_{cat} **(s^{-1})**	k_{cat}/K_m **(s^{-1} mM^{-1})**
Acrylonitrile	78 ± 3	99 ± 8	1.26 ± 0.07
Benzonitrile	18.3 ± 0.5	33 ± 1	1.80 ± 0.02
NTCB	0.0017 ± 0.0003	0.017 ± 0.003	111 ± 14

*Mb*NHase Incorporates Cobalt into Its Active Site

The protein obtained after purification exhibited an amber color (Figure 34A) similar to other Co-type NHases (126). To confirm that the purified *Mb*NHase enzyme contains cobalt, the enzyme was analyzed by inductively-coupled plasma mass spectrometry (ICP-MS) along with a sample of the purified Co-type NHase from *Pseudonocardia thermophila* JCM 3095 (*Pt*NHase). ICP-MS confirmed the presence of cobalt in *Mb*NHase, which exhibited a cobalt content of 0.9 equivalences per αβ monomer similar to *Pt*NHase, which contained 0.8 equivalents of cobalt per αβ heterodimer. Interestingly, this novel NHase is able to incorporate the metal ion into the active site in the absence of a NHase activator protein or any accessory protein during protein expression. It has been found that the co-expression of NHase genes with an activator gene is necessary for metal insertion and the post-translational oxidation of the two equatorial active site cysteine residues (32-35). The exception to this requirement is

the Fe-type NHase from *Comamonas testosteroni* Ni1, which we showed does not require an activator or accessory protein for metal insertion and the oxidation of the two active site equatorial ligands (118). In the investigations by Marron *et al*. (20) and Foerstner *et al*. (21) no open reading frames encoding for an NHase activator or accessory protein, which are usually found downstream of the prokaryotic NHase genes, were reported (20,21). However, it is interesting to speculate on whether the histidine rich insert of *Mb*NHase plays a similar role to that of the activator protein in metal acquisition and/or insertion. Based on IMAC purification it is clear that this histidine rich region is capable of binding metal ions as the protein bound tightly to the Ni-NTA column, eluting from the column when the concentration of imidazole was ~50% (250 mM imidazole).

Co-type NHases exhibit a characteristic absorption shoulder in the 300-350 nm region due to a weak S $\rightarrow$ Co(III) ligand-to-metal charge transfer band (LMCT) (36,39,127). The UV-Visible spectrum (Figure 35) of *Mb*NHase exhibited an intense peak at 280 nm with a shoulder at ~320 nm (ε = 19,392 M^{-1} cm^{-1}). No other absorption bands are observed in the visible region, consistent with Co-type NHases (49). Comparison of the observed UV-Visible spectrum of *Mb*NHase to *Pt*NHase (ε = 18, 062M^{-1} cm^{-1}) (Figure 35) indicated that they are nearly identical. These data are consistent with the presence of cobalt in *Mb*NHase and suggest that the cobalt ion resides in a typical NHase "claw setting" active site. Furthermore, these data also suggest that the cobalt ion in *Mb*NHase is likely found as a non-corrin low-spin Co(III).

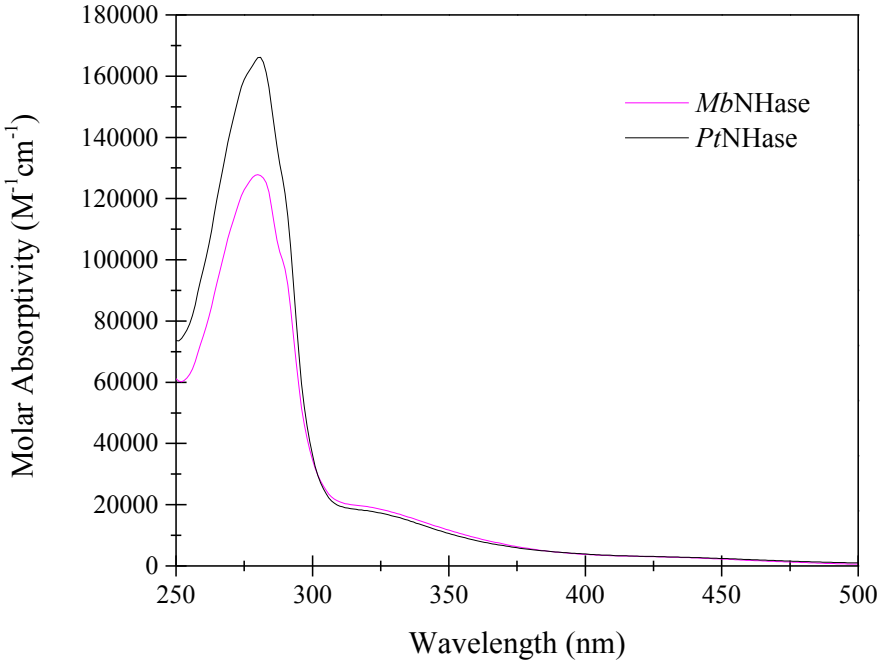

Figure 35. UV-Visible absorption spectrum of the purified *Mb*NHase and cobalt *Pt*NHase. Pink spectrum corresponds to *Mb*NHase (1.5 mg/mL) expressed in the presence of cobalt and black spectrum corresponds to cobalt *Pt*NHase (1.7 mg/mL).

Summary

Herein we report the successful expression of a recombinant NHase from the eukaryotic organism *M. brevicollis* providing the first evidence for a functional eukaryotic NHase. *Mb*NHase is capable of hydrating alkyl and aromatic nitrile substrates to their corresponding amides as well as thiocyanate substrates. Based on ICP-MS and UV-Visible spectroscopy, the *Mb*NHase is a Co-type NHase that incorporates cobalt into its active site without the assistance of an additional activator protein. Further studies are required to determine the role that the histidine rich insert plays in metal acquisition and/or insertion into eukaryotic NHases. Interestingly, similar histidine rich regions are present in some proteins of the cobalamin (vitamin B12) biosynthetic pathway, e.g., the chelatase CbiX enzyme from *Bacillus megaterium* and CobW from *Pseudomonas*

denitrificans (128). Histidine rich regions are also found in the metallochaperone and accessory proteins involved in metallocenter assembly of the nickel hydrogenases and ureases, such as HypB from *Bradyrhizobium japonicum* and *Rhizobium leguminosarum*, SlyD from *Escherichia coli* and *Helicobacter pylori*, UreE from *Klebsiella aerogenes*, Hpn and Hpn-like proteins from *Helicobacter pylori* (129). Based on the similarity of the histidine rich region with accessory proteins involved in the metallocenter assembly of cobalamin, hydrogenases, and ureases, it is possible that the histidine rich insert that links the α and β subunits of *Mb*NHase, and those found in other eukaryotic NHases, play a role in cobalt binding and possible insertion of the cobalt ion into the active site.

Experimental Procedures

Reagents. All reagents of the highest grade were obtained from commercial suppliers. The *Mb*NHase gene and oligonucleotides were obtained from Integrated DNA Technologies, Inc.

Plasmid construction. The protein sequence for the *Mb*NHase gene was obtained from UniProt ID A9V2C1.1 and used to commercially synthesize the gene with *E. coli* codon usage and cloned into the pUCIDT kanamycin resistant vector with *NdeI* and *HindIII* restriction sites. The gene was subsequently digested and ligated into the ampicillin resistant pET21a$^+$ (Novagen) expression vector to create the plasmid *Mb*NHase/pET21a$^+$. All plasmid sequences were confirmed using the automated DNA sequencing at the University of Chicago Cancer Research Center DNA sequencing facility.

Expression and purification of recombinant MbNHase. The *Mb*NHase/pET21a$^+$ plasmid was transformed into *E. coli* BL21(DE3) cells (Agilent). A single colony from

the transformation was used to inoculate a 50 mL LB Miller culture containing 50 μg/mL of carbenicillin and allowed to grow at 37 °C and constant shaking overnight. This overnight culture was used to inoculate a 3 L of LB Miller culture containing 100 μg/mL of ampicillin and grown at 37 °C with constant shaking until an optical density of ~0.8-1.0 at 600 nm was reached. The culture was cool down to 20 °C then subsequently induced with 0.1 mM IPTG, supplemented with 0.25 mM $CoCl_2$, and then expressed at 20 °C for 16 h. Cells were harvested by centrifugation at 6,370 *g* for 10 min at 4 °C, resuspended in buffer A (50 mM NaH_2PO_4 pH 8.0, 500 mM NaCl, and 10 mM imidazole) with 5% glycerol and store at -80 °C.

The frozen cell suspension was thawed and lysed by sonication. Cell debris was removed by two rounds of centrifugation at 31,000 *g* for 20 min at 4 °C. The clarified lysate was loaded onto a 5 mL Ni-NTA Superflow column (Qiagen). The column was washed extensively with buffer A containing 35 mM imidazole, followed by washes with buffer A containing 60 mM and 110 mM imidazole, respectively. The bound protein was eluted with a linear gradient of imidazole (110-500 mM). Peak fractions were pooled and concentrated using an Amicon Ultra-15 centrifugal filter device with a molecular-weight-cutoff (MWCO) of 50 K.

Gel filtration chromatography was used to polish and assessed the quaternary structure of *Mb*NHase. A 16/60 Superdex 200 prep grade (GE Healthcare) column was equilibrated with 50 mM HEPES pH 8.0 and 300 mM NaCl (buffer B). The column was calibrated using the MWGF200 gel filtration calibration kit (β-Amylase, 200 kDa; Alcohol Dehydrogenase, 150 kDa; Albumin, 66 kDa; Carbonic Anhydrase, 29 kDa; Cytochrome c, 12.4 kDa) from Sigma. The concentrated sample (2 mL) from the IMAC

purification was applied to the column and the protein was eluted in buffer B. The molecular mass of *Mb*NHase was calculated from a standard curve derived from the molecular mass standards used to calibrate the column. The purity of *Mb*NHase was analyzed by using 12.5% SDS-PAGE. The protein concentration was determined by UV absorbance at 280 nm using a calculated molar extinction coefficient of 143,700 M^{-1} cm^{-1}. The calculated molecular mass of the homodimer was 111,207 Da. Theoretical molecular mass and protein extinction coefficients were calculated with the ExPASy ProtParam tool (107).

Kinetic Assay. NHase activity was determined by measuring the hydration of acrylonitrile, benzonitrile, and 2-nitro-5-thiocyanatobenzoic acid (NTCB) in 50 mM Tris-HCl, pH 7.0 at 25 °C. The rate of the nitrile hydration was followed by continuously monitoring the increase in absorbance using the absorption coefficients of the corresponding amide product. Acrylamide ($\Delta\varepsilon_{225}$ = 2.9 mM^{-1} cm^{-1}) was measured at 225 nm (57). Benzamide ($\Delta\varepsilon_{242}$ = 5.5 mM^{-1} cm^{-1}) was measured at 242 nm(57). Formation of the thiolate product from NTCB was measured at 412 nm ($\Delta\varepsilon_{412}$ = 13,600 M^{-1} cm^{-1}) (112). All assays were performed in a 1 mL quartz cuvette on a Shimadzu UV-2600 spectrophotometer equipped with a TCC-240A temperature controlled cell holder. The reaction was initiated by adding the enzyme to the reaction mixture (1 mL) containing various final concentrations of the substrate. One unit of enzyme activity was defined as the amount of enzyme that catalyzed the production of 1 μmol of the amide per minute at 25 °C. To obtain the kinetic parameters, V_{max} and K_m, the initial velocities from at least two independent measurements were fitted to the Michaelis-Menten Equation by non-linear regression using OriginPro 9.0 (OriginLab, Northampton, MA).

UV-Visible Spectra. Absorption spectra were recorded on Shimadzu UV-2600 spectrophotometer equipped with a TCC-240A temperature controlled cell holder in 1 mL quartz cuvette in 50 mM HEPES, pH 8.0, and 300 mM NaCl at 25 °C for *Mb*NHase and 50 mM HEPES, pH 7.5, and 300 mM NaCl for *Pt*NHase.

Metal Analysis. The metal content of purified proteins was determined by inductively-coupled plasma mass spectrometry (ICP-MS). Purified *Mb*NHase (1 mg) expressed in the presence of cobalt and *Pt*NHase (1 mg) along with a control of buffer containing no protein were digested with concentrated nitric acid (0.863 mL) and heated at 70 °C for 1 h. The samples were allowed to cool to room temperature then diluted to final concentration of 5% nitric acid. The metal content was analyzed using an ICP-MS at the Water Quality Center in the College of Engineering at Marquette University.

CHAPTER SIX

ACRYLAMIDE PRODUCTION USING ENCAPSULATED NITRILE HYDRATASE FROM *PSEUDONOCARDIA THERMOPHILA* JCM 3095 IN A SOL-GEL MATRIX

Research Aim

Nitrile hydratase has great potential as a biocatalyst for organic chemical processing because of its ability to convert nitriles to amides under physiological conditions. As described in the introduction chapter, for industrial applications whole cells containing NHase and some isolated, purified, NHases have been immobilized on various supports by means of adsorption, entrapment, cross-linking, and membrane immobilization (22). While the immobilization of whole cells containing NHase have been successful for the production of various commodity chemicals, purified NHases are necessary for the specific hydration of nitriles with other hydrolysable groups that will be susceptible to side-reactions within a bacterial cell. In addition, reaction systems that cannot tolerate carboxylate side products also require purified NHase since other enzymes in the bacterial nitrile degradation pathway, such as nitrilases and amidases can convert nitriles to carboxylates (130). Purified enzymes also eliminate the need to have nitrile substrates pass across cell membranes; this would otherwise decrease the yields of recoverable products (22,131). However a major issue in the use of enzymes (whole cells or purified), in general, and NHases specifically in organic synthetic processes is the difficulty in separating the enzyme from the synthetic reaction mixture (78). A related

issue involves the use of aprotic solvents in organic synthetic reaction mixtures, which renders most enzymes including NHase inactive (78,132,133). One way to overcome some of these hurdles is through the encapsulation of enzymes within silica glasses derived through sol-gel processing (134-137). Encapsulated enzymes have resulted in the generation of novel functional materials that are optically transparent and sufficiently porous to permit small substrates access to the entrapped enzyme (135,138-143). Recent studies have demonstrated that encapsulated proteins retain their solution structure and native function while residing in the hydrated pore of the sol-gel (135,144-146). Moreover, nanoscopic confinement within sol-gels stabilizes proteins against thermal and proteolytic degradation (135,141). These physical properties permit the broad application of sol-gel:protein materials as chemical sensors, separation media, and heterogeneous catalysts (147).

With the aim of creating a robust and recyclable NHase biomaterial for the conversion of acrylonitrile to acrylamide in aqueous and organic co-solvents conditions, purified Co-NHase from *Pseudonocardia thermophila* JCM 3095 (*Pt*NHase) was immobilized by encapsulation using the sol-gel process in tetramethyl orhosilicate (TMOS) gels.

Encapsulation of *Pt*NHase

*Pt*NHase containing a hexa-histidine tag on the C-terminus was purified by IMAC and used for encapsulation in TMOS gels using the sol-gel method to create a monolith at the bottom of a glass vial. After solidification, the monolith was washed with buffer and stored in buffer at 4° C overnight. Analysis of both the buffer in which the monoliths were stored and the buffer from all the washing steps using the Bradford assay indicated

that on average <0.5% of the *Pt*NHase protein was present in both the wash buffer and the storage buffer. These data indicate that ~99.5% of the protein is encapsulated within the sol-gel matrix.

Under solution conditions, *Pt*NHase catalyzes the hydration of acrylonitrile at pH 7.5 and 25 ^{o}C with a k_{cat} value of 1,460 ± 90 s^{-1} and a K_m value of 1.3 ± 0.3 mM. Non-proteolytically digested *Pt*NHase:sol-gel biomaterial reacts readily with acrylonitrile (Figure 36) at 35 °C in 50 mM Tris-HCl pH 7.5 with >90% conversion of 600 mM acrylonitrile to acrylamide in 60 min. These data indicate that the kinetics of substrate turnover for sol-gel encapsulated NHases appear to be governed by mass transport of the substrate through the porous gel to the enzyme active site and product release. The reaction mixture was analyzed by high-performance-liquid chromatography (HPLC) and no acrylic acid was detected indicating that only the desired product, acrylamide, was produced. Quantitating the reaction of acrylonitrile with *Pt*NHase:sol-gel biomaterials is difficult as the exact quantity of encapsulated enzyme is not known, however, assuming that ~99.5% of the enzyme used was encapsulated at least 12% of the solution state activity is retained at 35 °C. Protein denaturation or inaccessibility to enzyme buried within the sol-gel material likely results in reduced activity upon encapsulation of the enzyme. Even so, these biomolecular nanocomposites display the expected enzymatic properties including substrate recognition as NHases in solution.

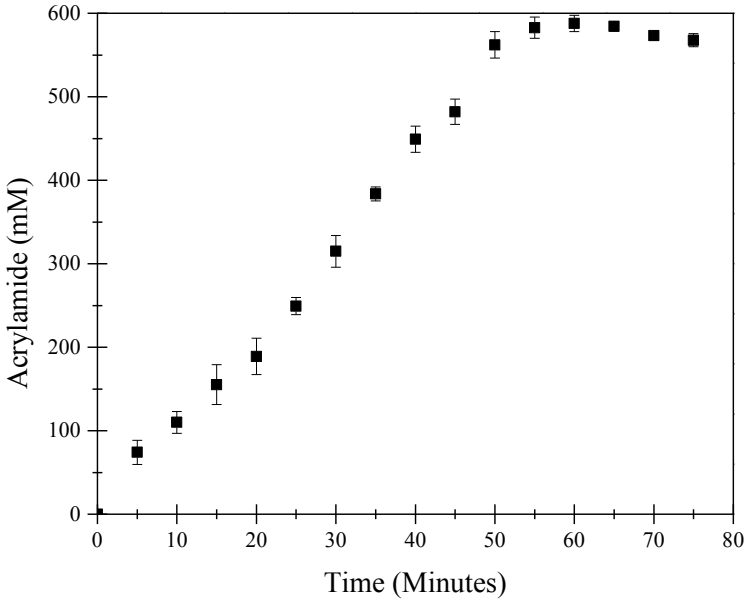

Figure 36. Time course for the hydration of 600 mM acrylonitrile to acrylamide. The reaction was carried out in 50 mM Tris-HCl pH 7.5 at 35 °C using *Pt*NHase:sol-gels containing 1.8 mg of *Pt*NHase.

Proteolytic Digestion of Soluble *Pt*NHase and *Pt*NHase:sol-gel Biomaterial

To ensure that substrate has access to fully encapsulated enzyme and not simply protein adhered to the surface, the *Pt*NHase:sol-gel biomaterial was treated with trypsin or α-chymotrypsin to proteolytically digest all surface accessible protein. The *Pt*NHase:sol-gel biomaterial retained >90% of its residual activity after digestion with either trypsin or α-chymotrypsin (Figure 37) while soluble *Pt*NHase retained <15% of its residual activity after digestion, indicating that surface bound enzyme is hydrolyzed, but interior *Pt*NHase is not. These data also indicate that substrate has access to the *Pt*NHase enzyme trapped in the interior of the sol-gel biomaterial, which is an active catalyst but protected from proteolytic digestion.

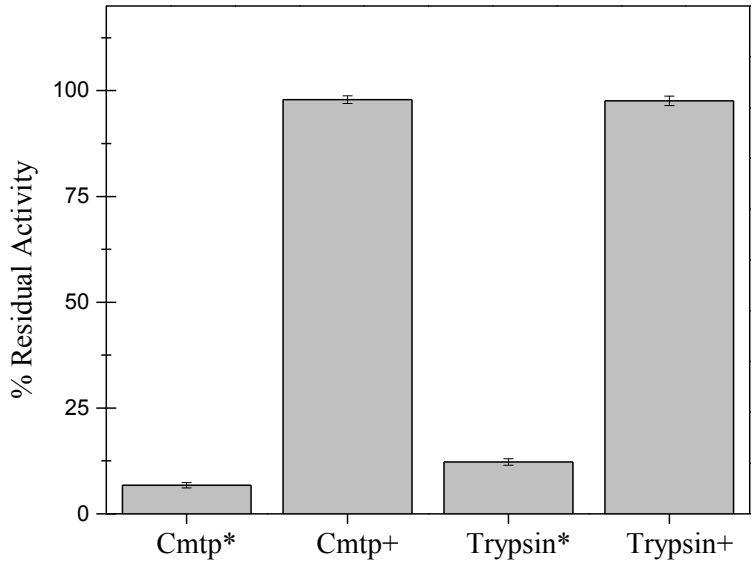

Figure 37. Residual activity of soluble *Pt*NHase (*) and *Pt*NHase:sol-gels (+) proteolytically digested with α-chymotrypsin (Cmtp) and trypsin. The soluble *Pt*NHase (*) and *Pt*NHase:sol-gels (+) were incubated at a 1:1 ratio of enzyme:protease for 18 h at 35 C. Residual activity was measured with 100 mM (soluble *Pt*NHase) and 600 mM (*Pt*NHase:sol-gels) acrylonitrile in 50 mM Tris-HCl pH 7.5 at 35 °C.

Thermostability of Soluble *Pt*NHase and *Pt*NHase:sol-gel Biomaterial

The thermostability of soluble *Pt*HNase enzyme and the *Pt*NHase:sol-gel biomaterial was evaluated over a temperature range of 50 to 80 °C. Both soluble *Pt*NHase enzyme and *Pt*NHase:sol-gel biomaterial were highly stable at 50 °C over 600 min incubation (Figure 38). At 60 °C, the stability of the soluble *Pt*NHase enzyme decreases significantly after 30 min of incubation (Figure 38A); however, the *Pt*NHase:sol-gel biomaterial showed greater stability at this temperature (Figure 38B). The *Pt*NHase:sol-gel biomaterial also showed improved stability after incubation at 70 °C compared to the soluble enzyme (Figure 38B). Neither the soluble enzyme nor the biomaterials were stable when incubated at 80 °C. Based on published studies that have looked at the thermostability of soluble vs. encapsulated enzymes (141,148,149), we

hypothesized that the observed improvement in thermostability of the enzyme upon the encapsulation in the sol-gel matrix is due to the enzyme being in a conformation that prevents unfolding and thus its denaturation at high temperatures.

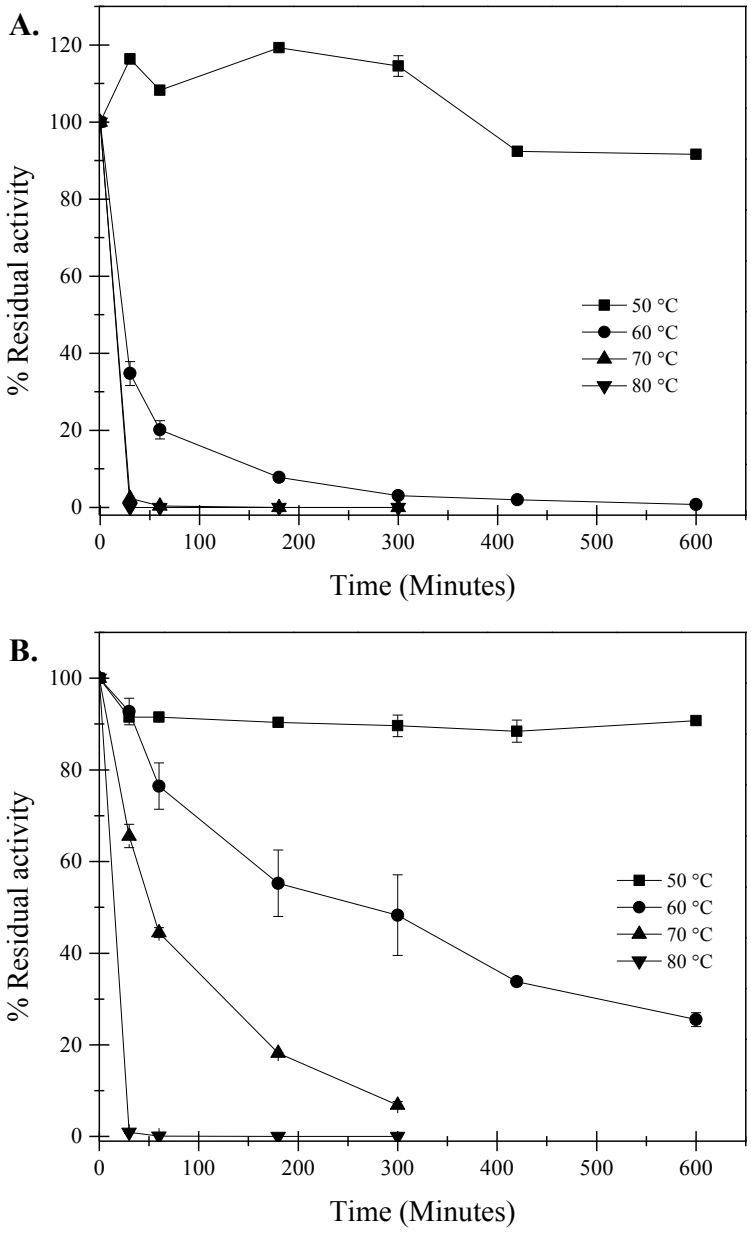

Figure 38. Thermostability of soluble *Pt*NHase (**A**) and *Pt*NHase:sol-gels (**B**). The residual activity of the soluble and encapsulated after the high temperature incubation was determined by measuring the hydration of acrylonitrile to acrylamide at 35 °C.

Reusability and Long-Term Stability of the *Pt*NHase:sol-gel Biomaterial

For commercial applications, a biocatalyst must be reusable and have long term stability (76). With this in mind we sought to investigate whether the *Pt*NHase:sol-gel biomaterial could be recycled in subsequent reactions with acrylonitrile. After every use, the *Pt*NHase:sol-gel biomaterial was thoroughly washed with buffer to remove residual acrylonitrile and acrylamide then submitted to the same reaction conditions (Figure 39). The conversion of acrylonitrile to acrylamide decreases linearly with ~50% of the initial activity remaining after thirteen cycles. The *Pt*NHase:sol-gel biomaterial can also be stored at 4 °C in buffer and used weeks later without significant loss of activity (Figure 40). Thus, encapsulation enhances the stability of *Pt*NHase and provides a biomaterial that can be recycled multiple times, stored for long periods of time, and reused.

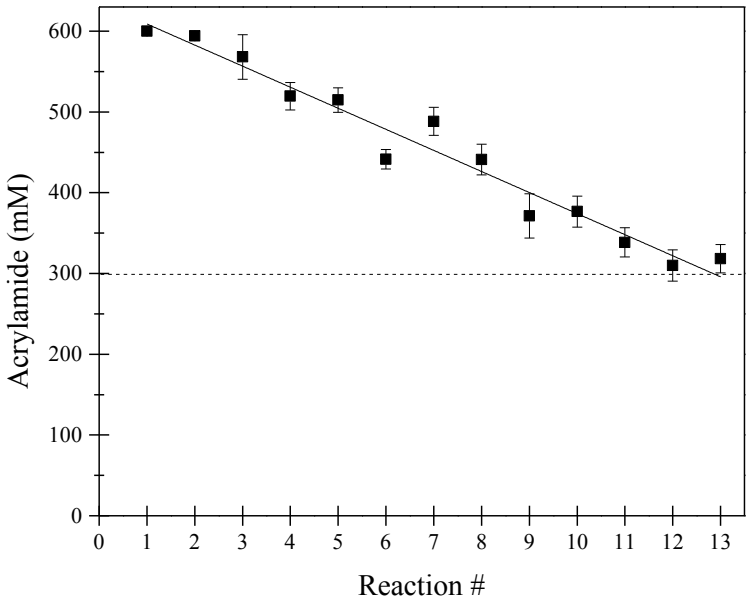

Figure 39. Production of acrylamide using recycled *Pt*NHase:sol-gels. Each reaction consisted of 600 mM acrylonitrile in 50 mM Tris-HCl pH 7.5 at 35 °C, 1 h.

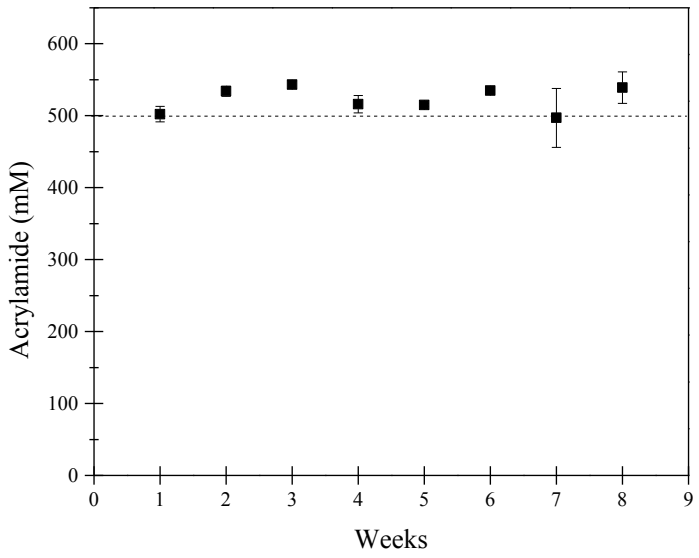

Figure 40. Long-term stability of the *Pt*NHase:sol-gels. The *Pt*NHase:sol-gel hydrogels were used for the hydration of 600 mM acrylonitrile in 50 mM Tris-HCl pH 7.5 at 35 °C, 1 h.

Stability of the Soluble *Pt*NHase and *Pt*NHase:sol-gel Biomaterial in Organic Co-solvent

Typically, the solubility of nitriles at high concentrations becomes problematic requiring organic solvents; however, enzymes often denature in organic solvents. The *Pt*NHase:sol-gel biomaterial placed in methanol is able to hydrolyze acrylonitrile to acrylamide. Since only one mole of water is consumed in each catalytic cycle, enough water may exist in the sol-gel or in the methanol to allow the encapsulated enzyme to remain catalytic. Therefore, we examined the hydration of acrylonitrile in 90:10 (data not shown), 70:30 and 50:50 MeOH:water solvent mixtures (Figure 41A). Greater than 90% conversion of acrylonitrile to acrylamide was achieved in 50:50 MeOH:water solvent mixtures while ~75 % conversion was achieved in 70:30 MeOH:water solvent mixtures (41B). For comparison purposes, soluble *Pt*NHase exhibits only 65% of its native activity in 50:50 MeOH:water solvent mixtures which decreases to 15% in 70:30

MeOH:water solvent mixtures (Figure 41B). Thus, sol-gel encapsulation affords a significant stabilization against increasing protic solvent concentrations, compared to the non-encapsulated enzyme.

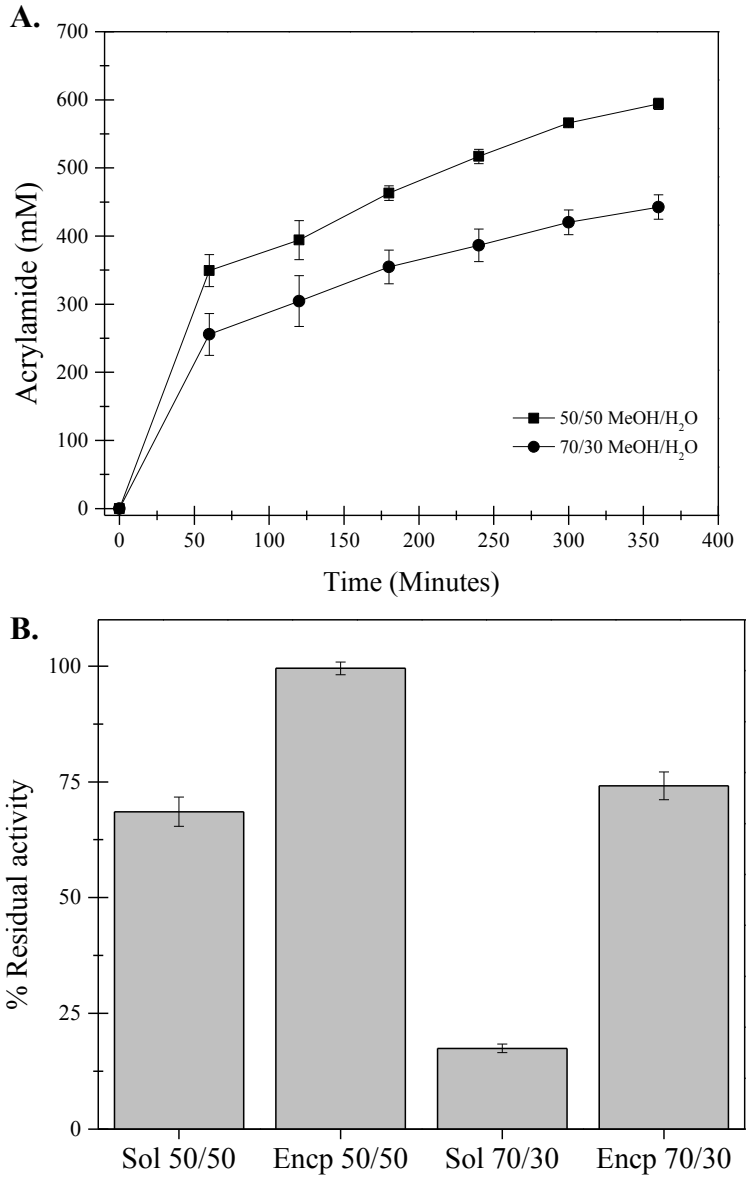

Figure 41. Hydration of acrylonitrile in MeOH:water mixtures. **A)** Time course for the hydration of 600 mM acrylonitrile to acrylamide at 25 °C, **B)** Residual activity of the soluble (Sol) and encapsulated (Encp) *Pt*NHase for the conversion of 600 mM acrylonitrile to acrylamide in a solution of 50/50 and 70/30 MeOH/water at 25 °C.

Summary

In summary, in this work we present the first encapsulation of a nitrile hydratase in a sol-gel matrix. The resulting biomaterial (*Pt*NHase:sol-gel) exhibits catalytic activity towards acrylonitrile providing only the acrylamide as the product. Although the activity of the encapsulated *Pt*NHase is diminished compared to the soluble *Pt*NHase, its thermal stability is markedly improved. The hydrogels were active and stable when exposed to proteases and the enzyme could withstand protic solvent mixtures. Additionally, *Pt*NHase:sol-gel biomaterials were successfully used and recycled for the hydration of 600 mM acrylonitrile to acrylamide and remained active for more than 8 weeks at 4 °C . The beauty of NHase biocatalytic materials as organic synthetic tools resides in the fact that the NHase:sol-gel materials can be cast into any shape desired and if cast as pellets, can be added in a catalytic amount to a reaction mixture and simply filtered or decanted off after a prescribed reaction time. Moreover, these materials will potentially provide functional biomaterials capable of hydrolyzing nitriles in a chemo-, regio-, and stereo-selective manner from a wide variety of nitrile substrates thus, providing synthetic chemists new avenues to design synthetic methodologies using nitriles as starting materials. This work has been published in the Journal of Molecular Catalysis B: Enzymatic: Salette Martinez, Misty L. Kuhn, James T. Russell, Richard C. Holz, and Timothy E. Elgren, *Journal of Molecular Catalysis B: Enzymatic*, **2014**, *100*, 19-24.

Experimental Procedures

Materials. Tetramethyl orthosilicate (TMOS, ≥99%), acrylonitrile, acrylamide, Type I Trypsin from bovine pancreas, and Type II α-chymotrypsin from bovine pancreas,

were purchased from Sigma-Aldrich. All reagents were of the highest purity available and used as received without further purification.

Kinetic characterization of PtNHase. The activity of purified *Pt*NHase was determined by measuring the hydration of 100 mM acrylonitrile to acrylamide (225 nm, $\varepsilon = 2.9\ mM^{-1}\ cm^{-1}$) in 50 mM Tris-HCl, pH 7.5 at 35 °C. Assays were performed in a 1 mL quartz cuvette in triplicate on a Shimadzu UV-2450 PC spectrophotometer equipped with a TCC temperature controller. One unit of enzyme activity was defined as the amount of enzyme that catalyzed the production of 1 μmol of acrylamide per minute at 35 °C.

Encapsulation of PtNHase in tetramethyl orthosilicate. The sol consisted of 1.57 mL of TMOS, 0.350 mL Nanopure (18 Ω) H_2O, and 0.011 mL of 0.040 M HCl. The mixture was sonicated on ice for 30 min, and then left on ice for ~1 h prior to protein incorporation. Hydrolyzed TMOS sol (0.100 mL) was mixed with an equal volume of pure *Pt*NHase (1.8 mg) in 50 mM Tris-HCl, pH 7.5, 300 mM NaCl. The mixture was placed on ice until solidification occurred to create *Pt*NHase:sol-gel monoliths at the bottom of a glass vial. Following solidification, the monoliths were washed three times with 0.400 mL of 50 mM Tris-HCl, pH 7.5 (sol-gel buffer) and stored at 4 °C overnight in 0.400 mL of the same buffer. The following day, the aged monoliths were crushed to produce a heterogeneous material and then washed three times with 0.400 mL of the sol-gel buffer. The buffer used to age the *Pt*NHase:sol-gels and buffer from the wash were tested for protein leaching by the Coomassie (Bradford) Protein Assay Kit (Pierce).

Kinetic characterization of the PtNHase:sol-gel. The activity of the *Pt*NHase:sol-gel biomaterial was determined by measuring the conversion of acrylonitrile to acrylamide using high performance liquid chromatography (HPLC). A 5 mL solution of

600 mM acrylonitrile in 50 mM Tris-HCl pH 7.5 at 35°C was reacted with *Pt*NHase:sol-gel biomaterial with constant shaking at 250 rpm. Aliquots of the reaction mixture (0.300 mL) were taken at fixed-time intervals and analyzed by HPLC using a Shimadzu Shim-Pack XR-ODS C18 reverse-phase column (3.0 mm i.d. × 75 mm) with a mixture of 97% water: 3% methanol as the mobile phase at 220 nm. The specific activity (U/mg) of the *Pt*NHase:sol-gel biomaterial was calculated from the reaction rate (mmol/L/min), the amount of the *Pt*NHase encapsulated, and the volume of the reaction. The concentration of acrylamide produced was determined using standard curves of peak area versus known acrylamide concentrations.

Recycling experiments. A 5 mL solution of 600 mM acrylonitrile in 50 mM Tris-HCl pH 7.5 at 35 °C was reacted with *Pt*NHase:sol-gel biomaterial for 1 h after which an aliquot (0.300 mL) was taken for HPLC analysis. The product mixture was then decanted and the hydrogel washed with 1.2 mL of sol-gel buffer. The *Pt*NHase:sol-gel hydrogel was re-suspended in 5 mL of 600 mM acrylonitrile in 50 mM Tris-HCl pH 7.5 at 35 °C and the reaction repeated as described above. This process of reacting, recovering, washing, and re-suspending the *Pt*NHase:sol-gel hydrogel was repeated 12 additional times resulting in 12 separate cycles with the same sample of the *Pt*NHase:sol-gel biomaterial.

Proteolytic digestion of soluble and PtNHase:sol-gels. Trypsin digestion of soluble (0.5 mg) *Pt*NHase and *Pt*NHase:sol-gel material (1.8 mg of *Pt*NHase) was performed at a ratio of 1:1 (Trypsin:*Pt*NHase) in 50 mM Tris-HCl and 1 mM $CaCl_2$, pH 7.6 (trypsin reaction buffer) at 35 °C for 18 h with constant agitation. The α-chymotrypsin digestion of soluble *Pt*NHase (0.5 mg) and *Pt*NHase:sol-gel material (1.8

mg of *Pt*NHase) was performed in 100 mM Tris-HCl and 10 mM $CaCl_2$, pH 8.0 (α-chymotrypsin buffer), also at a 1:1 ratio (α-Chymotrypsin:*Pt*NHase) at 35 °C for 18 h with constant agitation. Along with the digestion samples, controls that consisted of *Pt*NHase in trypsin and α-chymotrypsin reaction buffers were also incubated at 35 °C for 18 h with constant agitation. Following digestion, the degraded samples of soluble *Pt*NHase and controls were centrifuged, cooled on ice, and assayed for *Pt*NHase activity using the assay conditions described above. The activity of the control samples was taken as 100%. The *Pt*NHase:sol-gels were thoroughly washed three times with 0.400 mL of sol-gel buffer to remove trypsin or α-chymotrypsin and digestion products. Then the *Pt*NHase:sol-gel hydrogels were assayed for catalytic using the standard assay conditions.

Activity of soluble and encapsulated PtNHase in organic co-solvents. The activity of the soluble *Pt*NHase with 50, 70, and 100% (v/v) methanol as the organic co-solvent towards acrylonitrile was measured spectrophotometrically at 25 °C as described above. Each measurement was repeated at least three times. The hydration of acrylonitrile using the *Pt*NHase:sol-gel hydrogels with organic co-solvents at 50, 70 and 100% (v/v) was carried out in 5 mL reactions of 600 mM acrylonitrile at 25 °C with constant shaking (250 rpm). Aliquots, 0.300 mL, of the reaction mixture were taken at fixed-time intervals and analyzed by HPLC as described above.

Thermostability of the soluble and immobilized PtNHase. The thermostability of soluble *Pt*NHase and *Pt*NHase:sol-gel biomaterial was determined by incubation at 50, 60, 70, and 80 °C for 0, 30, 60, 180, 300, 420, and 600 min. After the incubation period

was completed, the residual enzyme activity of the samples was determined using the assay conditions described above.

CHAPTER SEVEN

CONCLUSIONS

In conclusion, the studies presented herein have as provided useful information to elucidate the catalytic mechanism of NHase, gain insight into the biosynthesis of an unusual Fe-NHase, gain insight into the functionality of a novel eukaryotic cobalt NHase, and provided an alternative process for the immobilization of NHase. Kinetic analyses in the presence of two potential substrate-analog boronic acid inhibitors, 1-butaneboronic acid and phenylboronic acid, and the solved X-ray crystal structures with bound boronic acids using *Pt*NHase, provided information on several previously unresolved mysteries of the NHase catalytic mechanism. First, the study showed that boronic acids are good competitive inhibitors for NHase, therefore, useful for mechanistic studies. The X-ray crystal structures of *Pt*NHase in complex with the boronic acids offered the characterization of potential catalytic intermediates along the NHase catalytic reaction pathway, which until now have not been observed. Furthermore, the results point to the active site Cys-SOH ligand as the possible nucleophile in the NHase mechanism, which directly attacks the carbon atom of the nitrile substrate, a previously unknown role for the Cys-SOH ligand. Lastly, the results also provided evidence for the direct coordination of the substrate to the metal ion.

Although these results have provided much needed answers in the reaction mechanism of NHase, there are still catalytic details that need to be addressed.

Missing or unclear details regarding the NHase reaction mechanism include: (*i*) distinction between the two proposed reaction mechanism pathways (Figure 15); (*ii*) evidence to determine the protonation state of the Cys-SO_2H and Cys-SOH ligands; (*iii*) identity of the catalytic base. Studies, targeting these questions will certainly help in further understanding the NHase catalytic mechanism.

The studies done on the Fe-NHase from *C. testosteroni* Ni1, have showed that this enzyme is unusual among other NHases because it fails to follow the strict requirement of the co-expression of the activator protein for the assembly of a functional active site. The combination of enzyme kinetics, metal analysis, UV-Visible spectroscopy, and X-ray crystallography provided strong evidence for the correct assembly of this Fe-NHase active site in the absence of the activator protein. The X-ray crystal structure showed two potential explanations for the incorporation of the metal ion into the active site, which include: (*i*) a loop located above the active site that contributes to a wide-open and solvent accessible active site; (*ii*) the solvent accessible active site provides a direct approach for the substrate and the metal ion. Further studies on this NHase, for example site-directed mutagenesis of residues along the solvent accessible channel could provide additional information about amino acid residues potentially involve in the assembly of the active site.

Additional insights into the catalytic properties of NHase were obtained by the site-directed mutagenesis studies done on the Fe-NHase from *C. testosteroni* Ni1. These studies showed the importance of a hydrogen-bond provided by an arginine residue to the Cys-SOH ligand. Hydrogen bonding to the active site Cys-SOH ligand, which has been shown to be the nucleophile, is important for its stabilization during the hydration of the

nitrile substrate. In addition, the mutagenesis studies also showed that the two non-conserved histidine residues near the active site are important in maintaining the structure of the α-subunit and hydrogen-bonding networks near the active site. Future studies that include the mutation of other arginine residues that hydrogen-bond to the Cys-SOH could provide additional evidence that support the importance of hydrogen bonding in the stabilization of the nucleophile during the catalysis. Because mutation of an arginine residue that hydrogen bonds to the Cys-SOH to an alanine or lysine residue decreases the catalytic rate, it could be possible to use this type of mutant to trap an NHase-substrate intermediate and characterize it by X-ray crystallography.

The investigations presented in this thesis have also provided experimental evidence that support the existence of a new member of the nitrile hydratase family, a NHase from a eukaryotic organism. The data showed that this NHase is able to incorporate cobalt and can hydrate several nitrile substrates. In contrast to the NHase from bacterial organisms, this NHase contains both subunits connected by a histidine rich insert. Since, no activator protein has been reported for this NHase but was able to incorporate the metal ion on its own, we proposed that this histidine rich insert could be involve in the metal acquisition or incorporation, in other words, this insert maybe acting as the activator protein during the expression of the NHase. Future studies that focus on the histidine rich insert would provide details on the role of this insert in the biosynthesis of this new NHase.

The sol-gel process was used to immobilize an NHase by encapsulation and create a biomaterial for the hydration of acrylonitrile to acrylamide. The encapsulated activity retained a detectable activity after the encapsulation and the method developed for

encapsulation incorporated ~ 99.5% of the protein within the sol-gel matrix and no protein leaching from the material was observed. One of the interesting properties obtained with this *Pt*NHase:sol-gel biomaterial was the observed activity in high concentrations of organic co-solvent. Such a property could allow for the hydration of hydrophobic nitriles, which are difficult to perform in aqueous media. With improvement, this biomaterial could find potential usage for the hydration of other nitrile substrates besides acrylonitrile.

REFERENCE LIST

1. Martínková, L., Uhnáková, B., Pátek, M., Nešvera, J., and Křen, V. (2009) *Environment International* **35**, 162-177

2. Banerjee, A., Sharma, R., and Banerjee, U. (2002) *Applied Microbiology and Biotechnology* **60**, 33-44

3. Ramteke, P. W., Maurice, N. G., Joseph, B., and Wadher, B. J. (2013) *Biotechnology and Applied Biochemistry* **60**, 459-481

4. Howden, A. J. M., and Preston, G. M. (2009) *Microbial Biotechnology* **2**, 441-451

5. Baxter, J., and Cummings, S. P. (2006) *Antonie van Leeuwenhoek* **90**, 1-17

6. Gupta, N., Balomajumder, C., and Agarwal, V. K. (2010) *Journal of Hazardous materials* **176**, 1-13

7. Kato, Y., Ooi, R., and Asano, Y. (1998) *Archives of Microbiology* **170**, 85-90

8. Kato, Y., Ooi, R., and Asano, Y. (2000) *Applied and Environmental Microbiology* **66**, 2290-2296

9. Sawai, H., Sugimoto, H., Kato, Y., Asano, Y., Shiro, Y., and Aono, S. (2009) *Journal of Biological Chemistry* **284**, 32089-32096

10. Prasad, S., and Bhalla, T. C. (2010) *Biotechnology Advances* **28**, 725-741

11. Coffey, L., Clarke, A., Duggan, P., Tambling, K., Horgan, S., Dowling, D., and O'Reilly, C. (2009) *Archives of Microbiology* **191**, 761-771

12. Kato, Y., Yoshida, S., Xie, S.-X., and Asano, Y. (2004) *Journal of Bioscience and Bioengineering* **97**, 250-259

13. Xie, S.-X., Kato, Y., Komeda, H., Yoshida, S., and Asano, Y. (2003) *Biochemistry* **42**, 12056-12066

14. Oinuma, K.-I., Hashimoto, Y., Konishi, K., Goda, M., Noguchi, T., Higashibata, H., and Kobayashi, M. (2003) *Journal of Biological Chemistry* **278**, 29600-29608

15. Langdahl, B. R., Bisp, P., and Ingvorsen, K. (1996) *Microbiology* **142**, 145-154

16. Sorokin, D. Y., van Pelt, S., Tourova, T. P., and Muyzer, G. (2007) *Applied and Environmental Microbiology* **73**, 5574-5579

17. Colquhoun, J. A., Heald, S. C., Li, L., Tamaoka, J., Kato, C., Horikoshi, K., and Bull, A. T. (1998) *Extremophiles* **2**, 269-277

18. Brandão, P. F. B., Clapp, J. P., and Bull, A. T. (2003) *Applied and Environmental Microbiology* **69**, 5754-5766

19. Lipowicz, B., Hanekop, N., Schmitt, L., and Proksch, P. (2013) *Marine Drugs* **11**, 3046-3067

20. Marron, A. O., Akam, M., and Walker, G. (2012) *PLoS ONE* **7**, e32867

21. Foerstner, K. U., Doerks, T., Muller, J., Raes, J., and Bork, P. (2008) *PLoS ONE* **3**, e3976

22. Velankar, H., Clarke, K. G., Preez, R. d., Cowan, D. A., and Burton, S. G. (2010) *Trends in Biotechnology* **28**, 561-569

23. Okamoto, S., and Eltis, L. D. (2007) *Molecular Microbiology* **65**, 828-838

24. Nishiyama, M., Horinouchi, S., Kobayashi, M., Nagasawa, T., Yamada, H., and Beppu, T. (1991) *Journal of Bacteriology* **173**, 2465-2472

25. Hashimoto Y., N., M., Horinouchi S., Beppu T. (1994) *Bioscience, Biotechnology, and Biochemistry* **58**, 1859-1869

26. Nojiri, M., Yohda, M., Odaka, M., Matsushita, Y., Tsujimura, M., Yoshida, T., Dohmae, N., Takio, K., and Endo, I. (1999) *Journal of Biochemistry* **125**, 696-704

27. Petrillo, K. L., Wu, S., Hann, E. C., Cooling, F. B., Ben-Bassat, A., Gavagan, J. E., DiCosimo, R., and Payne, M. S. (2005) *Applied Microbiology and Biotechnology* **67**, 664-670

28. Wu, S., Fallon, R. D., and Payne, M. S. (1997) *Applied Microbiology and Biotechnology* **48**, 704-708

29. Kataoka, S., Arakawa, T., Hori, S., Katayama, Y., Hara, Y., Matsushita, Y., Nakayama, H., Yohda, M., Nyunoya, H., Dohmae, N., Maeda, M., and Odaka, M. (2006) *FEBS Letters* **580**, 4667-4672

30. Arakawa, T., Kawano, Y., Kataoka, S., Katayama, Y., Kamiya, N., Yohda, M., and Odaka, M. (2007) *Journal of Molecular Biology* **366**, 1497-1509

31. Cameron, R. A., Sayed, M., and Cowan, D. A. (2005) *Biochimica et Biophysica Acta (BBA) - General Subjects* **1725**, 35-46

32. Zhou, Z., Hashimoto, Y., Cui, T., Washizawa, Y., Mino, H., and Kobayashi, M. (2010) *Biochemistry* **49**, 9638-9648

33. Lu, J., Zheng, Y., Yamagishi, H., Odaka, M., Tsujimura, M., Maeda, M., and Endo, I. (2003) *FEBS Letters* **553**, 391-396

34. Zhou, Z., Hashimoto, Y., Shiraki, K., and Kobayashi, M. (2008) *Proceedings of the National Academy of Sciences* **105**, 14849-14854

35. Zhou, Z., Hashimoto, Y., and Kobayashi, M. (2009) *Journal of Biological Chemistry* **284**, 14930-14938

36. Brennan, B. A., Alms, G., Nelson, M. J., Durney, L. T., and Scarrow, R. C. (1996) *Journal of the American Chemical Society* **118**, 9194-9195

37. Sugiura, Y., Kuwahara, J., Nagasawa, T., and Yamada, H. (1987) *Journal of the American Chemical Society* **109**, 5848-5850

38. Nelson, M. J., Jin, H., Turner, I. M., Grove, G., Scarrow, R. C., Brennan, B. A., and Que, L. (1991) *Journal of the American Chemical Society* **113**, 7072-7073

39. Payne, M. S., Wu, S., Fallon, R. D., Tudor, G., Stieglitz, B., Turner, I. M., and Nelson, M. J. (1997) *Biochemistry* **36**, 5447-5454

40. Scarrow, R. C., Brennan, B. A., Cummings, J. G., Jin, H., Duong, D. J., Kindt, J. T., and Nelson, M. J. (1996) *Biochemistry* **35**, 10078-10088

41. Brennan, B. A., Cummings, J. G., Chase, D. B., Turner, I. M., and Nelson, M. J. (1996) *Biochemistry* **35**, 10068-10077

42. Huang, W., Jia, J., Cummings, J., Nelson, M., Schneider, G., and Lindqvist, Y. (1997) *Structure* **5**, 691-699

43. Nagashima, S., Nakasako, M., Dohmae, N., Tsujimura, M., Takio, K., Odaka, M., Yohda, M., Kamiya, N., and Endo, I. (1998) *Nature Structural & Molecular Biology* **5**, 347-351

44. Miyanaga, A., Fushinobu, S., Ito, K., and Wakagi, T. (2001) *Biochemical and Biophysical Research Communications* **288**, 1169-1174

45. Hourai, S., Miki, M., Takashima, Y., Mitsuda, S., and Yanagi, K. (2003) *Biochemical and Biophysical Research Communications* **312**, 340-345

46. Murakami, T., Nojiri, M., Nakayama, H., Dohmae, N., Takio, K., Odaka, M., Endo, I., Nagamune, T., and Yohda, M. (2000) *Protein Science* **9**, 1024-1030

47. Piersma, S. R., Nojiri, M., Tsujimura, M., Noguchi, T., Odaka, M., Yohda, M., Inoue, Y., and Endo, I. (2000) *Journal of Inorganic Biochemistry* **80**, 283-288

48. Mascharak, P. (2013) The Active Site of Nitrile Hydratase: An Assembly of Unusual Coordination Features by Nature. Springer Berlin Heidelberg. pp 1-25

49. Kovacs, J. A. (2004) *Chemical Reviews* **104**, 825-848

50. Kobayashi, M., and Shimizu, S. (1999) *European Journal of Biochemistry* **261**, 1-9

51. Okamoto, S., and Eltis, L. D. (2011) *Metallomics* **3**, 963-970

52. Boone, A. J., Cory, M. G., Scott, M. J., Zerner, M. C., and Richards, N. G. J. (2001) *Inorganic Chemistry* **40**, 1837-1845

53. Lugo-Mas, P., Dey, A., Xu, L., Davin, S. D., Benedict, J., Kaminsky, W., Hodgson, K. O., Hedman, B., Solomon, E. I., and Kovacs, J. A. (2006) *Journal of the American Chemical Society* **128**, 11211-11221

54. Dey, A., Chow, M., Taniguchi, K., Lugo-Mas, P., Davin, S., Maeda, M., Kovacs, J. A., Odaka, M., Hodgson, K. O., Hedman, B., and Solomon, E. I. (2006) *Journal of the American Chemical Society* **128**, 533 - 541

55. Mascharak, P. K. (2002) *Coordination Chemistry Reviews* **225**, 201-214

56. Kopf, M.-A., Bonnet, D., Artaud, I., Pétré, D., and Mansuy, D. (1996) *European Journal of Biochemistry* **240**, 239-244

57. Miyanaga, A., Fushinobu, S., Ito, K., Shoun, H., and Wakagi, T. (2004) *European Journal of Biochemistry* **271**, 429-438

58. Kukushkin, V. Y., and Pombeiro, A. J. L. (2002) *Chemical Reviews* **102**, 1771-1802

59. Jin, H., Turner, I. M., Nelson, M. J., Gurbiel, R. J., Doan, P. E., and Hoffman, B. M. (1993) *Journal of the American Chemical Society* **115**, 5290-5291

60. Doan, P. E., Nelson, M. J., Jin, H., and Hoffman, B. M. (1996) *Journal of the American Chemical Society* **118**, 7014-7015

61. Mitra, S., and Holz, R. C. (2007) *Journal of Biological Chemistry* **282** 7397-7404

62. Rao, S. N., and Holz, R. C. (2008) *Biochemistry* **47**, 12057–12064

63. Hopmann, K. H., and Himo, F. (2008) *European Journal of Inorganic Chemistry* **2008**, 3452-3459

64. Yamanaka, Y., Hashimoto, K., Ohtaki, A., Noguchi, K., Yohda, M., and Odaka, M. (2010) *Journal of Biological Inorganic Chemistry* **15**, 655-665

65. Hopmann, K. H., Guo, J.-D., and Himo, F. (2007) *Inorganic Chemistry* **46**, 4850-4856

66. Hopmann, K. H., and Himo, F. (2008) *European Journal of Inorganic Chemistry* **2008**, 1406-1412

67. Heinrich, L., Mary-Verla, A., Li, Y., Vaissermann, J., and Chottard, J.-C. (2001) *European Journal of Inorganic Chemistry* **2001**, 2203-2206

68. Taniguchi, K., Murata, K., Murakami, Y., Takahashi, S., Nakamura, T., Hashimoto, K., Koshino, H., Dohmae, N., Yohda, M., Hirose, T., Maeda, M., and Odaka, M. (2008) *Journal of Bioscience and Bioengineering* **106**, 174-179

69. Hashimoto, K., Suzuki, H., Taniguchi, K., Noguchi, T., Yohda, M., and Odaka, M. (2008) *Journal of Biological Chemistry* **283**, 36617-36623

70. Mylerova, V., and Martinkova, L. (2003) *Current Organic Chemistry* **7**, 1279-1295

71. Wang, M.-X. (2005) *Topics in Catalysis* **35**, 117-130

72. MartÍnková, L., and Křen, V. (2002) *Biocatalysis and Biotransformation* **20**, 73-93

73. Yamada, H., Shimizu, S., and Kobayashi, M. (2001) *The Chemical Record* **1**, 152-161

74. Shaw, N. M., Robins, K. T., and Kiener, A. (2003) *Advanced Synthesis & Catalysis* **345**, 425-435

75. Rozzell, J. D. (1999) *Bioorganic & Medicinal Chemistry* **7**, 2253-2261

76. Bornscheuer, U. T. (2003) *Angewandte Chemie International Edition* **42**, 3336-3337

77. Woodley, J. M. (2008) *Trends in Biotechnology* **26**, 321-327

78. Sheldon, R. A. (2007) *Advanced Synthesis & Catalysis* **349**, 1289-1307

79. Tischer, W., and Wedekind, F. (1999) Immobilized Enzymes: Methods and Applications. in *Biocatalysis - From Discovery to Application* (Fessner, W.-D., Archelas, A., Demirjian, D. C., Furstoss, R., Griengl, H., Jaeger, K. E., Morís-Varas, E., Öhrlein, R., Reetz, M. T., Reymond, J. L., Schmidt, M., Servi, S., Shah, P. C., Tischer, W., and Wedekind, F. eds.), Springer Berlin Heidelberg. pp 95-126

80. Datta, S., Christena, L. R., and Rajaram, Y. (2013) *3 Biotech* **3**, 1-9

81. Miletić, N., Nastasović, A., and Loos, K. (2012) *Bioresource Technology* **115**, 126-135

82. Nagasawa, T., Shimizu, H., and Yamada, H. (1993) *Applied Microbiology and Biotechnology* **40**, 189-195

83. Thomas, S. M., DiCosimo, R., and Nagarajan, V. (2002) *Trends in Biotechnology* **20**, 238-242

84. Yamada, H., and Kobayashi, M. (1996) *Bioscience, Biotechnology, and Biochemistry* **60**, 1391-1400

85. Hann, E. C., Eisenberg, A., Fager, S. K., Perkins, N. E., Gallagher, F. G., Cooper, S. M., Gavagan, J. E., Stieglitz, B., Hennessey, S. M., and DiCosimo, R. (1999) *Bioorganic & Medicinal Chemistry* **7**, 2239-2245

86. Mersinger, L. J., Hann, E. C., Cooling, F. B., Gavagan, J. E., Ben-Bassat, A., Wu, S., Petrillo, K. L., Payne, M. S., and DiCosimo, R. (2005) *Advanced Synthesis & Catalysis* **347**, 1125-1131

87. Pelt, S., Quignard, S., Kubá, D., Sorokin, D. Y., Rantwijk, F., and Sheldon, R. A. (2008) *Greem Chemistry* **4**, 395-400

88. Pawar, S. V., and Yadav, G. D. (2014) *Journal of Molecular Catalysis B: Enzymatic* **101**, 115-121

89. Kamble, A., Banoth, L., Meena, V., Singh, A., Chisti, Y., and Banerjee, U. C. (2013) *3 Biotech* **3**, 319-330

90. Maksimova, Y. G., Vasilyev, D. M., Ovechkina, G. V., Maksimov, A. Y., and Demakov, V. A. (2013) *Applied Biochemistry and Microbiology* **49**, 347-351

91. Maksimova, Y. G., Rogozhnikova, T. A., Ovechkina, G. V., Maksimov, A. Y., and Demakov, V. A. (2012) *Applied Biochemistry and Microbiology* **48**, 434-439

92. Maksimova, Y. G., Demakov, V. A., Maksimov, A. Y., Ovechkina, G. V., and Kovalenko, G. A. (2010) *Applied Biochemistry and Microbiology* **46**, 379-384

93. Chiyanzu, I., Cowan, D. A., and Burton, S. G. (2010) *Journal of Molecular Catalysis B: Enzymatic* **63**, 109-115

94. Smoum, R., Rubinstein, A., Dembitsky, V. M., and Srebnik, M. (2012) *Chemical Reviews* **112**, 4156-4220

95. Yang, W., Gao, X., and Wang, B. (2003) *Medicinal Research Reviews* **23**, 346-368

96. Morrison, J. F., and Walsh, C. T. (2006) The Behavior and Significance of Slow-Binding Enzyme Inhibitors. in *Advances in Enzymology and Related Areas of Molecular Biology*, John Wiley & Sons, Inc. pp 201-301

97. Baker, J. O., and Prescott, J. M. (1983) *Biochemistry* **22**, 5322-5331

98. Springsteen, G., and Wang, B. (2002) *Tetrahedron* **58**, 5291

99. Liu, C. T., and Benkovic, S. J. (2013) *Journal of the American Chemical Society* **135**, 14544-14547

100. DePaola, C. C., Bennett, B., Holz, R. C., Ringe, D., and Petsko, G. A. (1999) *Biochemistry* **38**, 9048-9053

101. Smoum, R., Rubinstein, A., Dembitsky, V. M., and Srebnik, M. (2012) *Chemical Reviews* **112**, 4156

102. Tsujimura, M., Odaka, M., Nakayama, H., Dohmae, N., Koshino, H., Asami, T., Hoshino, M., Takio, K., Yoshida, S., Maeda, M., and Endo, I. (2003) *Journal of the American Chemical Society* **125**, 11532-11538

103. Arakawa, T., Kawano, Y., Katayama, Y., Nakayama, H., Dohmae, N., Yohda, M., and Odaka, M. (2009) *Journal of the American Chemical Society* **131**, 14838-14843

104. Gumataotao, N., Kuhn, M. L., Hajnas, N., and Holz, R. C. (2013) *Journal of Biological Chemistry* **288**, 15532-15536

105. Yano, T., Wasada-Tsutsui, Y., Arii, H., Yamaguchi, S., Funahashi, Y., Ozawa, T., and Masuda, H. (2007) *Inorganic Chemistry* **46**, 10345-10353

106. Yamaki, T., Oikawa, T., Ito, K., and Nakamura, T. (1997) *Journal of Fermentation and Bioengineering* **83**, 474-477

107. Gasteiger, E., Hoogland, C., Gattiker, A., Duvaud, S. e., Wilkins, M., Appel, R., and Bairoch, A. (2005) Protein Identification and Analysis Tools on the ExPASy Server. in *The Proteomics Protocols Handbook* (Walker, J. ed.), Humana Press. pp 571-607

108. Otwinowski, Z., and Minor, W. (1997) Processing of X-ray diffraction data collected in oscillation mode. in *Methods in Enzymology* (Charles W. Carter, Jr. ed.), Academic Press. pp 307-326

109. Murshudov, G. N., Vagin, A. A., and Dodson, E. J. (1997) *Acta Crystallographica Section D* **53**, 240-255

110. Emsley, P., and Cowtan, K. (2004) *Acta Crystallographica Section D* **60**, 2126-2132

111. Adams, P. D., Grosse-Kunstleve, R. W., Hung, L.-W., Ioerger, T. R., McCoy, A. J., Moriarty, N. W., Read, R. J., Sacchettini, J. C., Sauter, N. K., and Terwilliger, T. C. (2002) *Acta Crystallographica Section D* **58**, 1948-1954

112. Stevens, J. M., Rao Saroja, N., Jaouen, M., Belghazi, M., Schmitter, J.-M., Mansuy, D., Artaud, I., and Sari, M.-A. (2003) *Protein Expression and Purification* **29**, 70-76

113. Baneyx, F., and Mujacic, M. (2004) *Nat Biotech* **22**, 1399-1408

114. Baneyx, F. (1999) *Current Opinion in Biotechnology* **10**, 411-421

115. Sari, M.-A., Jaouen, M., Saroja, N. R., and Artaud, I. (2007) *Journal of Inorganic Biochemistry* **101**, 614-622

116. Rzeznicka, K., Schätzle, S., Böttcher, D., Klein, J., and Bornscheuer, U. (2010) *Applied Microbiology and Biotechnology* **85**, 1417-1425

117. Cerbelaud, E., Levy-Schil, S., Petre, D., and Soubrier, F. (1995) Novel nitrile hydratases from Comamonas testosteroni and the genes encoding them and their uses. Rhone-Poulenc Chimie SA

118. Kuhn, M. L., Martinez, S., Gumataotao, N., Bornscheuer, U., Liu, D., and Holz, R. C. (2012) *Biochemical and Biophysical Research Communications* **424**, 365-370

119. Martinez, S., Wu, R., Sanishvili, R., Liu, D., and Holz, R. (2014) *Journal of the American Chemical Society* **136**, 1186-1189

120. Odaka, M., Noguchi, T., Nagashima, S., Yohda, M., Yabuki, S., Hoshino, M., Inoue, Y., and Endo, I. (1996) *Biochemical and Biophysical Research Communications* **221**, 146-150

121. Tsujimura, M., Dohmae, N., Odaka, M., Chijimatsu, M., Takio, K., Yohda, M., Hoshino, M., Nagashima, S., and Endo, I. (1997) *Journal of Biological Chemistry* **272**, 29454-29459

122. Kennepohl, P., Neese, F., Schweitzer, D., Jackson, H. L., Kovacs, J. A., and Solomon, E. I. (2005) *Inorganic Chemistry* **44**, 1826-1836

123. Brodkin, H. R., Novak, W. R. P., Milne, A. C., D'Aquino, J. A., Karabacak, N. M., Goldberg, I. G., Agar, J. N., Payne, M. S., Petsko, G. A., Ondrechen, M. J., and Ringe, D. (2011) *Biochemistry* **50**, 4923-4935

124. Shearer, J., Kung, I. Y., Lovell, S., Kaminsky, W., and Kovacs, J. A. (2000) *Journal of the American Chemical Society* **123**, 463-468

125. Nakasako, M., Odaka, M., Yohda, M., Dohmae, N., Takio, K., Kamiya, N., and Endo, I. (1999) *Biochemistry* **38**, 9887-9898

126. Nagasawa, T., Takeuchi, K., and Yamada, H. (1991) *European Journal of Biochemistry* **196**, 581-589

127. Katayama, Y., Hashimoto, K., Nakayama, H., Mino, H., Nojiri, M., Ono, T.-a., Nyunoya, H., Yohda, M., Takio, K., and Odaka, M. (2006) *Journal of the American Chemical Society* **128**, 728-729

128. Mendel, R. R., Smith, A. G., Marquet, A., and Warren, M. J. (2007) *Natural Product Reports* **24**, 963-971

129. Higgins, K. A., Carr, C. E., and Maroney, M. J. (2012) *Biochemistry* **51**, 7816-7832

130. Gong, J.-S., Lu, Z.-M., Li, H., Shi, J.-S., Zhou, Z.-M., and Xu, Z.-H. (2012) *Microbial Cell Factories* **11**, 142

131. Woodley, J. M. (2006) *Biochem Soc Trans* **34**, 301-303

132. Přepechalová, I., Martínková, L., Stolz, A., Ovesná, M., Bezouška, K., Kopecký, J., and Křen, V. (2001) *Applied Microbiology and Biotechnology* **55**, 150-156

133. Serdakowski, A. L., and Dordick, J. S. (2008) *Trends in Biotechnology* **26**, 48-54

134. Avnir, D., Thibaud, C., Ovadia, L., and Livage, J. (2006) *Journal of Materials Chemistry* **16**, 1013-1030

135. Gill, I. (2001) *Chemistry of Materials* **13**, 3404-3421

136. Dave, B. C., Dunn, B., Valentine, J. S., and Zink, J. I. (1994) *Analytical Chemistry* **66**, 1120A

137. Dunn, B., Miller, J. M., Dave, B. C., Valentine, J. S., and Zink, J. I. (1998) *Acta Materialia* **46**, 737

138. Ellerby, L., Nishida, C., Nishida, F., Yamanaka, S., Dunn, B., Valentine, J., and Zink, J. (1992) *Science* **255**, 1113-1115

139. Smith, K., Silvernail, N. J., Rodgers, K. R., Elgren, T. E., Castro, M., and Parker, R. M. (2002) *Journal of the American Chemical Society* **124**, 4247-4252

140. Wei, Y., Xu, J., Feng, Q., Lin, M., Dong, H., Zhang, W.-J., and Wang, C. (2001) *Journal of Nanoscience and Nanotechnology* **1**, 83-93

141. Eggers, D. K., and Valentine, J. S. (2001) *Protein Science* **10**, 250-261

142. Blyth, D. J., Aylott, J. W., Richardson, D. J., and Russell, D. A. (1995) *Analyst* **120**, 2725-2730

143. H. Lan, E., C. Dave, B., M. Fukuto, J., Dunn, B., I. Zink, J., and S. Valentine, J. (1999) *Journal of Materials Chemistry* **9**, 45-53

144. Elgren, T. E., Zadvorny, O. A., Brecht, E., Douglas, T., Zorin, N. A., Maroney, M. J., and Peters, J. W. (2005) *Nano Letters* **5**, 2085-2087

145. Frampton, M., Vawda, A., Fletcher, J., and Zelisko, P. M. (2008) *Chemical Communications*, 5544-5546

146. Pastor, I., Prieto, M., and Mateo, C. R. (2008) *The Journal of Physical Chemistry B* **112**, 15021-15028

147. Monton, M. R. N., Forsberg, E. M., and Brennan, J. D. (2012) *Chemistry of Materials* **24**, 796-811

148. Pierre, A. C. (2004) *Biocatalysis and Biotransformation* **22**, 145-170

149. Kandimalla, V. B., Tripathi, V. S., and Ju, H. (2006) *Critical Reviews in Analytical Chemistry* **36**, 73-106

VITA

Salette Martinez was born in Veracruz, Mexico. As a teenager she moved to Utica, Michigan, where she attended school. Between 2005 and 2009 she attended the University of Detroit Mercy, Detroit, where she earned a Bachelor of Science in Chemistry and a Minor in Mathematics.